A Multi-Zone Model of the CFR Engine: Investigating Cascading Autoignition and Octane Rating

Marlan Perumal

Thesis presented for the degree of
Master of Science in Engineering

Sasol Advanced Fuels Laboratory
Department of Mechanical Engineering
University of Cape Town

January 2011

Plagiarism Declaration

1. I know that plagiarism is wrong. Plagiarism is to use another's work and pretend that it is one's own.
2. Each contribution to, and quotation in, this thesis from the work(s) of other people has been attributed, and has been cited and referenced.
3. This thesis is my own work.
4. I have not allowed, and will not allow, anyone to copy my work with the intention of passing it off as his or her own work.
5. I acknowledge that copying someone else's work, or part of it, is wrong, and declare that this is my own work.

Marlan Perumal

Acknowledgments

I would like to thank the following people for their contributions and support:

1. Dr Gareth Floweday, who started out as my office mate and ended up as my supervisor, for his guidance, advice and leadership during the course of this project.

2. Prof Andy Yates, who started out as my supervisor and ended up as a voice of reason and wisdom who would whisper in my ear every now and again.

3. Dr Andre Swarts, for providing experimental data from his previous work on the CFR engine and for introducing me to said beast.

4. Dr Chris Woolard for teaching me some chemistry and for correcting me when I thought I'd learnt it.

5. My office mates, Victor Burger, Melissa Petersen and Mariam Ajam, for their wonderful wit and wisdom that made it a pleasure to come to work each day.

6. My students, who made me want to learn more.

7. My friends and family for being exactly what friends and family are for.

This work was performed at the Sasol Advanced Fuels Laboratory, which is run and funded by Sasol Technology Fuels Research.

Abstract

The CFR engine is the standardised research engine used for the measurement of knock resistance of fuels through the Research Octane Number (RON) and Motor Octane Number (MON) tests. In standard production engines, knock manifests as an almost instantaneous pressure rise followed by "knock ringing" pressure oscillations of similar magnitude. However, knock in the CFR engine is characterised, and measured by, a steep, but more gradual pressure rise, followed by ringing of much lesser magnitude. It has been previously proposed that a "cascading autoignition", resulting from an in-cylinder temperature gradient, is responsible for this unique pressure development.

A quasi-dimensional multi-zone model of the CFR engine has been developed in this work to investigate this phenomenon. The engine cylinder was divided into multiple zones containing the unburned fuel-air mixture. Each zone experienced different temperature-pressure histories during the compression stroke and flame propagation phases of the engine cycle. A Wiebe function description of flame propagation was used to describe the normal combustion process; mass and energy were transferred proportionally from the unburned zones to a single burned zone. The Functional Global Autoignition Model (FGAM) was used to describe the autoignition chemistry in the unburned zones and a chemical equilibrium approach was used to determine the composition of the burned zone.

The model was applied to nine Primary Reference Fuels (PRFs) and a Toluene Standardisation Fuel (TSF) under their respective RON and MON test conditions. The simulation results of the RON tests showed good agreement with experimental results obtained from a previous study. Analysis of the simulation results further provided insight into the possible role of low temperature chemistry and cool flames in the RON test. The results of the MON simulations did not show good agreement with experimental data, indicating a need for better data regarding inlet conditions of the MON test.

The FGAM was computationally more efficient than the commonly used alternative of detailed chemical kinetic models, but was still able to accurately simulate cool flame heat release behaviour. This enabled the multi-zone engine model to reproduce the unique post-knock pressure development in the CFR engine, the determinant of knock intensity in the Octane Rating tests, which traditional single and 2-zone models have been unable to do.

Table of Contents

List of Figures

List of Tables

List of Abbreviations

ATC	After Top-dead Centre
BTC	Before Top-dead Centre
CAD	Crank Angle Degrees
CCR	Critical Compression Ratio
CF	Cool Flame
CFID	Cool Flame Ignition Delay
CFD	Computational Fluid Dynamics
CFR	Co-operative Fuels Research: Refers to the standard engine used for the ASTM Octane Rating Tests
CID	Conservation of Ignition Delay
DISI	Direct Injection Spark Ignition
DKM	Detailed Kinetic Mechanism
ECU	Engine Control Unit
EGR	Exhaust Gas Recirculation
EVC	Exhaust Valve Closing
EVO	Exhaust Valve Opening
ext	External

FGAM	Functional Global Autoignition Model
GA	Genetic Algorithm
HCCI	Homogeneous Charge Compression Ignition
ID	Ignition Delay
int	Internal
IVC	Inlet Valve Closing
IVO	Inlet Valve Opening
KI	Knock Intensity
LLNL	Lawrence Livermore National Laboratory
MFB	Mass Fraction Burned
MON	Motor Octane Number
MON*XY*	Designation given to the test condition corresponding to MON rating of *XY*
MTBE	Methyl-Tertiary-Butyl-Ether
NTC	Negative Temperature Coeffcient
NVO	Negative Valve Overlap
ODE	Ordinary Differential Equation
OI	Octane Index
ON	Octane Number
OOP	Object Oriented Programming
PCFID	Post Cool Flame Ignition Delay
PRF	Primary Reference Fuel

PRF*XY*	Designation given to a blend of *XY*% iso-octane and the remainder n-heptane
PSO	Particle Swarm Optimisation
RCM	Rapid Compression Machine
REG	Residual Exhaust Gas
RON	Research Octane Number
RON*XY*	Designation given to the test condition corresponding to RON rating of *XY*
rpm	Revolutions Per Minute
RR	Reaction Rate
SI	Spark Ignition
SKI	Standard Knock intensity
T_{CF}	Cool Flame Ceiling Temperature
TDC	Top-Dead Centre
TSF	Toluene Standardization Fuel
TSF*XYZ*	Designation given to a TSF blend with an Octane Rating of *XY.Z*
VBA	Visual Basic for Applications

Chapter 1

Introduction

1.1 Background

The spark ignition (SI) engine has been the dominant prime mover of passenger vehicles for most of the 20th century and at least the early part of the 21st century. With the continual drive to increase performance and efficiency whilst reducing emissions, design of modern engines must continuously push the limits of operation. One of the major design considerations for SI engines is knock.

Spark knock is caused by autoignition of the unburned air-fuel mixture in the engine cylinder before it has been consumed by the expanding flame front [1]. Knock can potentially be very damaging to the engine and so places a limit on such design and operating conditions as compression ratio, spark timing and inlet pressure. This has resulted in a large amount of research over the years into the causes of knock and means by which to prevent it. From a fuels perspective, the Octane Rating of a fuel is the measure of its resistance to knock. This is measured by two standardised methods under different operating conditions to give the Motor Octane Number (MON) [2] and Research Octane Number (RON) [3].

The RON and MON tests were initially representative of the operating conditions of engines of the time, however modern engines have moved to combustion at lower temperature and higher pressure and so beyond conditions described by the RON and MON tests [4]. It is therefore important to understand the underlying cause of this sensitivity if one hopes to extrapolate from RON and MON values to predict the knock resistance of a given fuel in modern and future engines.

The main complication arising from this is that most fuels have different RON and MON values. This difference between the RON and MON values is termed the *sensitivity* of the fuel [5]. Having moved beyond the operating region in which the RON and MON tests were actually representative, it is important to understand the underlying cause of this

difference. It was in this light that research in the Sasol Advanced Fuels Laboratory at the University of Cape Town returned to the RON and MON tests themselves.

In an investigation of the ASTM testing methods, a comprehensive set of tests in a CFR engine under knocking and non-knocking conditions was conducted by Swarts, Yates and co-workers [6–12], noting several peculiarities of the Octane tests. One of these was the so-called "cascading autoignition" phenomenon, whereby the actual knock event manifested itself differently to conventional production engines. This was proposed to be due to a thermal gradient set up inside the combustion chamber of the CFR engine [12].

To investigate this, and the relationship between Octane measurement and the fuel and operating parameters, a computational model of the CFR engine was desired. Two areas of importance were identified:

- Fuel evaporative cooling effects
- Combustion and autoignition

Two separate modelling studies were initiated to investigate these. The first [13] took the form of a Computational Fluid Dynamics (CFD) model of fuel evaporation in the intake manifold and cylinder. This aimed to ascertain whether a significant temperature gradient could be set up in the CFR engine. In addition it aimed to provide realistic initial conditions for the second model. The final results of this investigation were unfortunately not available at the time of writing.

The second modelling study entailed the development of a multi-zone thermo-chemical model of the combustion process in the CFR engine, with the aim of reproducing the cascading autoignition phenomenon. It is this multi-zone engine model that is described in this thesis.

1.2 Research Objectives

The primary objective of this study was to set up a computational model that could reproduce the unique in-cylinder pressure development characteristic of the CFR engine knocking under standard Octane test conditions. In order to accomplish this, the model required the following:

- A multi-zone description of the cylinder contents so as to simulate an in-cylinder temperature gradient.
- A description of normal combustion in the engine due to flame propagation
- A suitable autoignition model to predict the onset of, and heat release due to, autoignition in the engine.

- The ability to alter the model's inlet conditions and certain operating parameters to match both the RON and MON tests.
- A means to quantify the severity of knock.

The model required validation by comparison with existing experimental data of knocking and non-knocking pressure traces in the CFR engine under Octane rating test conditions. With the model thus verified, the secondary objective of using the model to differentiate between fuels of different Octane Numbers was pursued.

1.3 Thesis Outline

The format of this thesis is as follows:

- A review of the prevailing literature in the fields of interests, covering three main topics:
  - Knock and the measurement of octane number
  - Autoignition modelling
  - Engine modelling techniques
- A description of the multi-zone engine model used in this study
- Results of calibration of the engine model to experimental data and a parametric study of the model response to various changes in operating and simulation parameters
- A description of the process of fitting the Functional Global Autoignition Model (FGAM) to various fuels
- Results of simulations of Primary Reference Fuel (PRF) and Toluene Standardisation Fuel (TSF) blends under their respective octane rating test conditions
- Discussion of results
- Conclusions
- Recommendations
- Appendices containing:
  - Calibration coefficients for the FGAM for PRF and TSF fuel blends used in this study
  - A review of optimization and solving algorithms considered in this work
  - Class descriptions for the Engine Model

Chapter 2

Literature Review

The topics of knock, autoignition and engine modelling have all been extensively investigated in the literature. As an introduction to the system being modelled in this work, this chapter begins with a description of the knock phenomenon. The topic of autoignition is next considered with specific emphasis on the complex two-stage autoignition behaviour that some hydrocarbon fuels display and current methods of modelling this behaviour. A description follows of the Octane Rating process, in which a fuel's resistance to knock is measured. Finally different modelling approaches that have been used to study knock in engines are presented, with consideration of the techniques and results that informed the development of the multi-zone engine model that is the subject of this thesis.

2.1 Knock in Spark Ignition Engines

During normal combustion in a spark ignition engine, the combustible air-fuel mixture is compressed by the rising piston before combustion is initiated by the spark. The flame front expands outwards from the initial spark, consuming the unburnt end-gas. As the flame expands, it in turn compresses the end-gas, further raising its temperature and pressure. Under abnormal conditions the end-gas can autoignite before it is consumed by the flame front. The audible sound associated with this abnormal combustion is termed knock [1].

Although the terms autoignition and knock are often used interchangeably in the context of the SI engine, it will be important to differentiate between the two. The following definitions will thus be used in this thesis:

autoignition is the spontaneous combustion of a fuel and air mixture without an external ignition source.

knock is the objectionable noise in an engine associated with autoignition of the unburned fuel-air mixture.

knock point is the first moment at which some portion of the unburned fuel-air mixture autoignites.

knock ringing refers to the pressure oscillations due to shock waves in the cylinder, which can be caused by the steep pressure rise associated with autoignition.

knock event refers to the complete knock phenomenon, beginning at the knock point and ending once the knock ringing has stopped.

These definitions allow for the application of the term "knock" to the traditional usage [1] in the context of standard production SI engines, to the unique way in which knock occurs in the CFR engine (explained in Section 2.4.1), as well as to other engine technologies (which will not be discussed here) such as *diesel knock* [1] and *HCCI knock* [14].

When knock occurs, it can be very damaging to the engine. Nates [15] and Heywood [1] both propose two primary modes of damage. The first mode is thermal loading, with possible damage including piston and ring seizure as well as piston burn-through. This can result in a positive feedback loop, with the hotter combustion chamber leading to earlier autoignition and so more severe knock. This in turn leads to greater thermal loading and substantial damage can ensue in a matter of minutes. The second, mode is a direct result of the energy release in the confined crevices found between the piston and liner, between piston rings and in the squish zones. This can result in piston erosion and/or piston jacking.

The prevention of knock has thus been a primary design criterion in the development of the SI engine. Compression ratio is limited by knock, as is spark advance and boost pressure in turbocharged engines. Modern gasoline engines include a knock sensor, which is an accelerometer tuned to pick up the vibrations of the engine in the range 6-10 kHz [11]. The engine electronic control unit (ECU) adjusts the operating parameters (eg. by retarding spark timing) upon detection of marginal knock to ensure essentially knock free engine operation. This means that knock is seldom a problem noted by the driver. However, the prevention of knock still places a performance constraint on the operation of the engine.

The onset of knock is affected by various parameters as described in Table 2.1. The reasons for these effects are well explained in engine texts such as [1,16] but the underlying reasons usually involve an increase in temperature, increase in pressure or an increase in the amount of time that the end-gas is exposed to these high temperatures and pressures and so is more likely to autoignite before being consumed by the flame front.

As knock is primarily an autoignition phenomenon, an understanding of autoignition itself is required. The next two sections cover the fundamentals of hydrocarbon autoignition and how to model it. This will introduce several concepts that are necessary in order to understand the manifestation of knock in the CFR engine during the Octane Rating tests.

Table 2.1: *Engine parameters that in general increase the likelihood of knock*

Change in Parameter
Increase Compression Ratio
Advance Spark Timing
Increase Inlet Temperature
Increase Inlet Pressure
Increase Burn Duration
Use Fuel with lower Octane Number

2.2 Hydrocarbon Autoignition

Following Heywood [1], *autoignition* is defined as a rapid combustion reaction, which is not initiated by an external ignition source. For combustible mixtures of air and most hydrocarbon fuels, this generally involves a complex reaction system consisting of many intermediate species and a series of initiation, propagation and termination reactions.

Perhaps the simplest manifestation of autoignition occurs for what are known as *single-stage* fuels such as toluene and methanol. Following an initial induction period, during which there is little to no apparent temperature change, the fuel-air mixture undergoes a very rapid temperature rise as the fuel combusts completely. This induction period is known as the *autoignition delay* or simply *ignition delay* (ID). The length of this ignition delay period is dependent on the fuel itself as well as various factors such as pressure, fuel-air equivalence ratio and most significantly temperature. With all else held constant, the ignition delay of a single stage fuel is generally given by an Arrhenius relation of the form

$$ID = Ae^{-B/T} \tag{2.1}$$

where T is the initial temperature and A and B are coefficients corresponding to the fuel-air mixture [1].

Experiments to determine autoignition delay are usually performed in devices such as a Rapid Compression Machine (RCM) [17,18] or Shock Tube [19,20]. In these devices a fuel-air mixture is compressed very quickly up to an initial raised temperature and pressure. The compression is performed by a piston in the case of the rapid compression machine and by the shock wave created by a rapidly expanding driver gas in the shock tube. The system is maintained at nominally constant volume for the RCM and constant pressure for the shock tube, and the ignition delay from the initial elevated temperature and pressure is recorded.

Some fuel molecules (such as the paraffins n-heptane and iso-octane) exhibit what is known as *2-stage autoignition*. At low to intermediate initial temperatures (T_i) (less than 1000 K), an initial ignition delay is followed by a small heat release event in which the temperature rises to to about 1000 K and then stabilises. This event is called the *cool flame* (CF), the initial delay is known as the *cool flame ignition delay* (CFID) and the temperature at the plateau is known as the *cool flame ceiling temperature* (T_{CF}). The difference between the initial temperature and the ceiling temperature is called the *cool flame temperature rise* (ΔT_{CF}) . Following the cool flame, a second induction period is noted (*post cool flame ignition delay* (PCFID)), after which the main heat release event occurs. The total time elapsed before the main heat release is the *overall ignition delay* (ID). These features are shown in Figure 2.1.

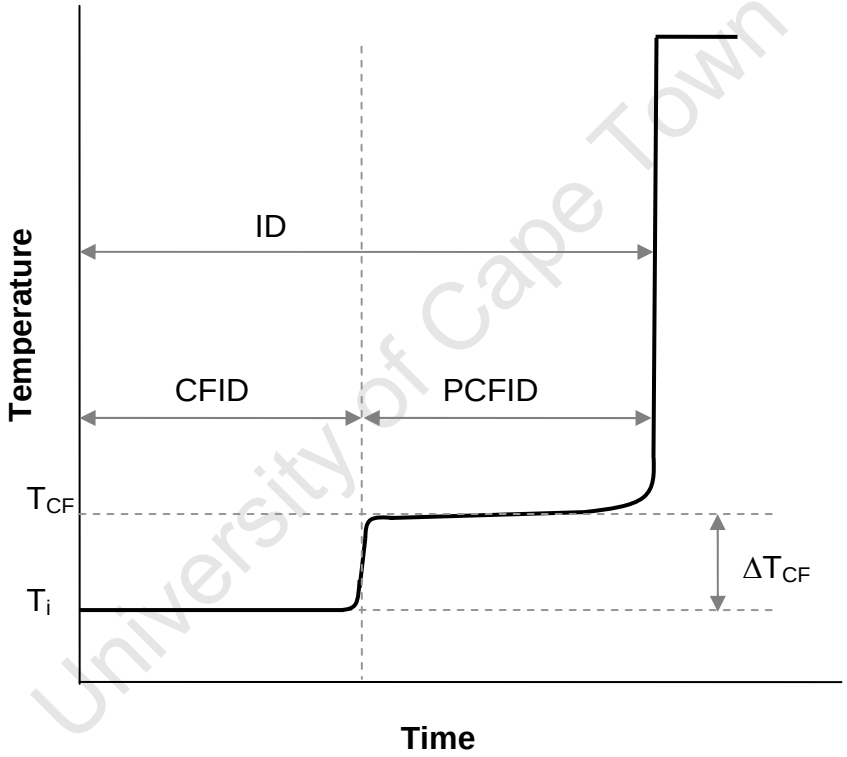

Figure 2.1: *Features of two-stage autoignition: initial temperature (T_i); overall ignition delay (ID); cool flame ignition delay (CFID); cool flame temperature rise (ΔT_{CF}); cool flame ceiling temperature (T_{CF}); post cool flame ignition delay (PCFID)*

At low temperatures the post cool flame ignition delay is, relatively, very short due to the high ceiling temperature and so the cool flame ignition delay and overall ignition delay are almost coincidental. The ignition delay at low temperatures is therefore governed mainly by this low temperature cool flame chemistry. As the initial temperature increases, the cool flame ignition delay decreases, however the ceiling temperature also decreases. This then increases the post cool flame ignition delay but the overall effect is still initially to

decrease the overall ignition delay. At some point however the trend reverses and the overall ignition delay actually increases with an increase in initial temperature. This is known as Negative Temperature Coefficient (NTC) behaviour. At some later point, the cool flame is no longer discernible and the ignition delay is once more dominated by the high temperature chemistry. Beyond this point, autoignition once again occurs in a single stage and appears to follow a straight line Arrhenius relation with temperature.

Following Floweday [21], these features can all be presented on the same set of axes (using slightly different nomenclature) as seen in Figure 2.2:

- Overall ignition delay (ID)
- Cool flame ignition delay (t_1) plotted as a function of initial temperature (T_i)
- Post cool flame ignition delay ($ID - t_1$) as a function of cool flame ceiling temperature
- Cool flame ceiling temperature (T_{cf}) plotted on the secondary axis as function of initial temperature
- Initial temperature plotted on a linear scale on the secondary axis for ease of reading

An analysis of the autoignition profile features of n-heptane was performed in [21] by considering the data in this format and several interesting features were noted. The first is the cool flame hook, in which the cool flame ignition delay exhibits its own NTC behaviour. The second is that once at the ceiling temperature, the post cool flame ignition delay is less than the expected ignition delay if the experiment had simply been started at the ceiling temperature. This implies that the low and high temperature pathways are not independent and it is suggested that the radicals created during the cool flame increase the reactivity of the mixture thereafter. Finally it was noted the cool flame ignition delay at low temperature (and resultantly the overall ignition delay in this region) was only very weakly dependent on pressure, whereas the effect of pressure at high temperature was more clearly evident.

Because of the S shaped curve formed by the NTC behaviour and low temperature cool flame chemistry, the ignition delay at low temperatures can be significantly lower than what would be predicted by only high temperature single stage chemistry. The distinction between single stage and 2-stage autoignition, as well as the various features of cool flame chemistry, have been described here as being easily discernible and indeed they are for most stoichiometric blends of pure 2-stage fuel components with no residual exhaust gas dilution. However for fuel blends (especially those containing both single stage and 2-stage fuels) of non-stoichiometric mixtures and high residual exhaust gas dilution, these distinctions can become blurred [21]. The NTC region may not imply an actual increase in ignition delay with increasing temperature but rather a change in slope. The induction periods, both cool flame and post cool flame, may be accompanied by noticeable heat release and temperature

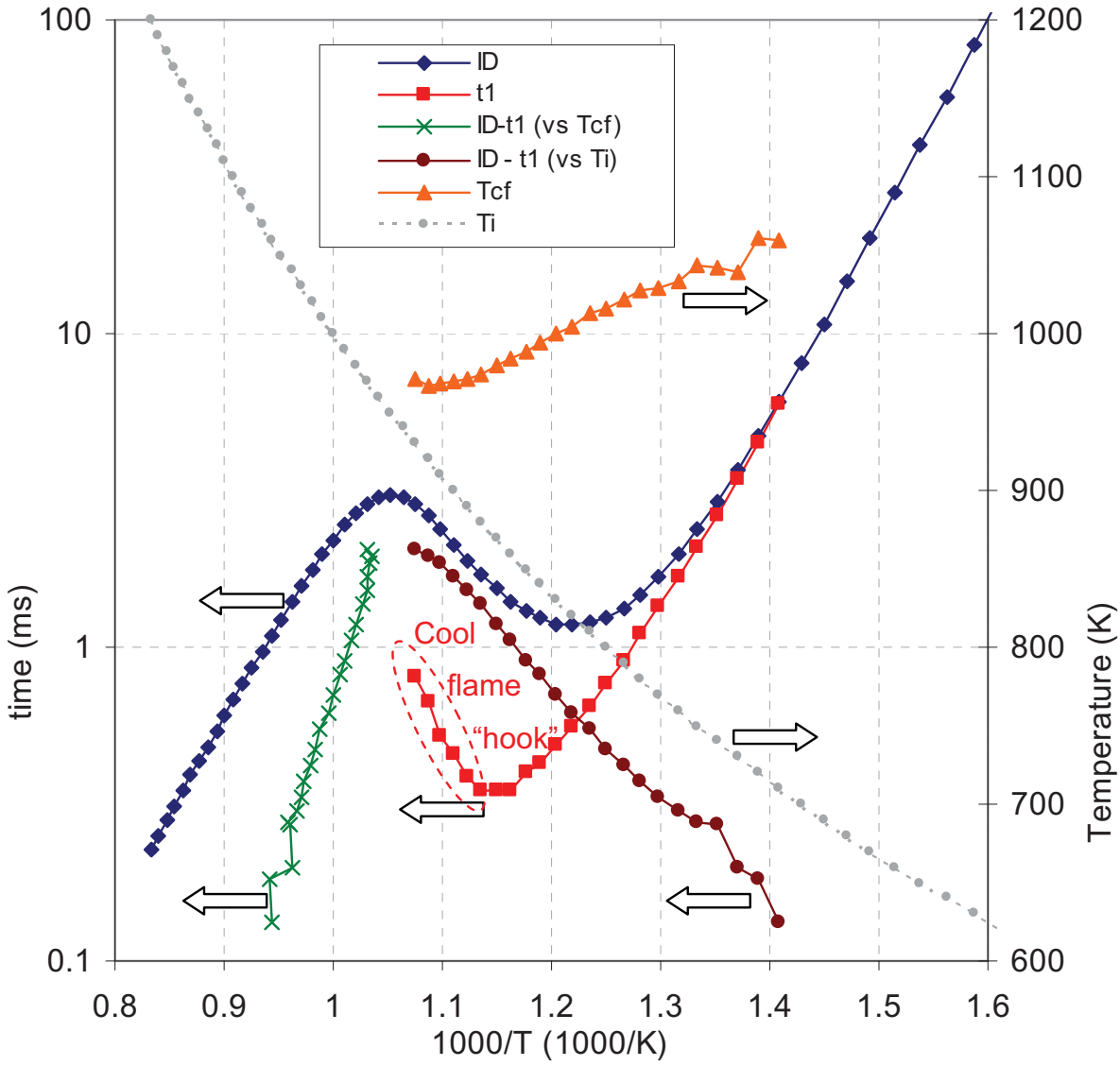

Figure 2.2: *Autoignition profile of n-heptane at $P = 20$ bar, $\phi = 1$, REG% = 0 [22]*

rise. The cool flame and main heat release events may occur more gradually and not in the near instantaneous fashion described [21]. As these are exactly the conditions encountered in CFR engine during the RON and MON tests, and since heat release effects may influence the manifestation of knock, it is important that an autoignition model be able to describe these features for a given fuel.

2.3 Autoignition Modelling

2.3.1 Detailed Kinetic Mechanisms

It is generally agreed that the most accurate descriptions of autoignition are the comprehensive Detailed Chemical Kinetics Mechanisms (DKM) [23]. These are an attempt to capture all the chemical species and reactions that can occur during the autoignition of a fuel-air mixture. Current examples include the mechanism developed at Lawrence Livermore National Laboratory (LLNL) [24] consisting of about 1550 species and 8000 reactions as well as the mechanism developed by Andrae and co-workers [25]. Both these mechanisms are capable of modelling blends of iso-octane, n-heptane, toluene and various other fuel components commonly considered in gasoline surrogates.

The thermo-chemical properties and reaction rate parameters are usually derived from fundamental principles and so can be independently validated by experimental results from RCMs and shock tubes. These models have shown very good correlation with experimental results for pure components over a wide range of temperatures and pressures [23]. The reaction rate approach allows for the description of species transport and would theoretically be capable of describing non-homogeneous systems. In practice however, the solving of these detailed kinetics systems are extremely computationally expensive and only basic systems can realistically be described without access to super-computing resources [26, 27].

Mechanisms for different fuels can be combined in order to predict the autoignition behaviour of blends. Special care must however be taken to ensure that any crossover reactions that can take place between species are also added into the mechanism [28]. These crossover reactions can produce unexpected results, such as the significantly reduced ignition delays for certain blends of iso-octane and toluene [18]. Again the computational expense involved places a limit on the number of components in a blend that can realistically be modelled. Real gasoline fuels that are composed of a multitude of different components can therefore not be modelled directly but must be approximated by gasoline surrogates [29, 30]. This may be sufficient for engine research but may be limiting for purposes of real fuel development.

2.3.2 Reduced Kinetic Mechanisms

Reduced Kinetics Mechanisms are simplifications of the DKMs achieved by removing species and reactions that have little effect on the overall result (especially where use in a limited range of temperature and/or pressure makes this possible) and by lumping together similar species. In this way species and reactions can be reduced from 1000s to 100s, reducing the computational effort required, though it is still quite large. This is usually accompanied by a loss in accuracy of the model so a trade-off must be made between accuracy and simulation time [21].

A significant research effort has been devoted to the development and refinement of these models. Griffiths [23] presents an excellent review of the reduction techniques applied and the reduced models available up to 1995. Further developments since then include the use of new computational methods for the reduction of mechanisms [31, 32] and the use of better detailed mechanisms such as [24, 25] as a basis.

2.3.3 Skeletal Kinetic Mechanisms

Models that are simplified even further, with judicious lumping to 10s of species and reactions, are referred to as skeletal models. A distinction can be made in that skeletal models are generally built up, by considering what classes of species and reactions are necessary to describe the autoignition behaviour, whereas reduced models are generally reduced down from the DKMs [23]. The thermo-chemical and reaction rate parameters are generally also determined by empirical means rather than from fundamentals [21]. The species used in skeletal models are however usually directly representative of specific radical and molecule classes and remain chemically defensible.

The accuracy of these models over the full temperature-pressure domain can be significantly reduced and although they can usually still perform reasonably at predicting the overall ignition delay of the modelled fuel, the characteristic cool flame behaviour is often not well described [21]. The advantage though is that the skeletal mechanisms can be small enough to be incorporated in more complex models such as CFD.

2.3.4 Global Autoignition Models

Global autoigniton models are mathematical descriptions of autoignition delay presented in the format of chemical kinetic models. Examples include the models of Schreiber [33] and Müller [34]. Although they are presented in the same format as skeletal chemical kinetics models and the species and reactions are inspired by the various radical pools present in the autoignition chemistry, the intermediate species do not truly correspond to these radical pools and the objective is aligned toward matching the autoignition behaviour rather than the actual chemistry.

That said, these models once again are generally limited in their prediction of overall ignition delay rather than the distinct cool flame features [21]. For the purposes of this thesis the distinction will be made that where the primary *objective* is the description of the class chemistry, the model will be termed skeletal, and where the primary objective is the fitting of autoignition delay and behaviour, the model will be termed global.

2.3.5 Empirical Autoignition Models

A final class of autoignition model is the empirical model. This is typically an explicit mathematical description of ignition delay (τ), not necessarily requiring a reaction rate approach. Examples include the single Arrhenius model proposed by Douad and Eyzat [35] and Yates 3-Arrhenius model [11].

These models can be implemented in a changing temperature-pressure environment through use of the *Conservation of Ignition Delay* (CID) approach proposed by Livengood and Wu [36]. In this approach it is assumed that autoignition occurs when the integral in Equation 2.2 goes to 1.

$$\int_0^t \frac{1}{\tau} dt \tag{2.2}$$

An empirical model was proposed by Yates and Viljoen [37] that could also simulate cool flame behaviour. This model uses an Arrhenius equation to calculate the cool flame ignition delay. A cool flame temperature rise is calculated and then imposed as a step function. A post cool flame ignition delay is then calculated including enhanced post cool flame reactivity through an "X-factor", and so the overall ignition delay is computed. There are 14 calibration parameters that can be adjusted to fit the autoignition profile of a given fuel and a formulation of these parameters is given for the PRF blends and methanol in [37].

The empirical model applied in this way is extremely computational efficient in computing ignition delay, however the step function approach does not properly describe the heat release rates that would occur during the knock event in an engine. It is also unclear how such a model would be able to be applied in a system with species transfer. A CFD implementation using the conservation of ignition delay approach with a single Arrhenius model was proposed by Lafossas [38]. A similar approach could perhaps be applied to the Yates and Viljoen model but would require some additional consideration in order to cater for the two stages of ignition.

2.3.6 The Functional Global Autoignition Model

By considering that for certain applications, accurate modelling of autoignition delay and cool flame behaviour is more important than accurately describing the chemistry involved, and acknowledging the advantages of a reaction rate based autoignition model, Floweday [39] proposed a Functional Global Autoignition Model (FGAM). This model is

primarily a description of autoignition behaviour but was developed with consideration of the actual reaction pathways that occur in paraffin chemistry, on the basis that a formulation that more closely resembled the real chemistry would be more likely to emulate the real behaviour.

The model consists of 9 species and 9 reactions and is schematically represented in Figure 2.3 with reaction rates as in Figure 2.4.

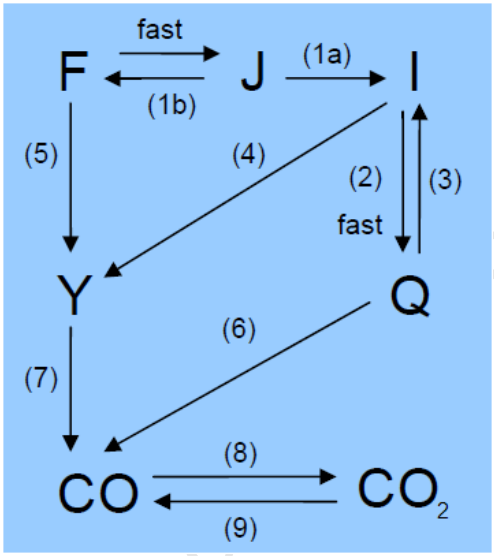

Figure 2.3: *Reaction schematic of the Functional Global Autoignition Model [22]*

Here F represents the fuel species. The intermediate species I, J, Q and Y all possess the same thermo-chemical properties as F. The coefficients α, β and γ are such that the balanced equation converts fuel and the appropriate amount of oxygen completely to CO and H_2O. For the set of reactions $F \rightleftharpoons J \rightarrow I$, a quasi-steady state assumption [40] was used to reduce to the single reaction $F \rightarrow I$ with the reaction rate as given.

Several features of this model are worth mentioning. The model contains 36 reaction rate parameters, which can be calibrated to physical experimental data or detailed chemical kinetics simulations. The fitness function to be minimised, used to calibrate the FGAM, was the area between the FGAM and DKM temperature time traces for 32 different sets of initial conditions. In this way, the model was capable of describing for n-heptane, iso-octane and a gasoline surrogate consisting of n-heptane, iso-octane, 1-hexene and toluene, the following autoignition features:

- cool flame ignition delay
- cool flame ceiling temperature

1	$F \rightarrow I$
2	$I \rightarrow Q$
3	$Q \rightarrow I$
4	$I \rightarrow Y$
5	$F \rightarrow Y$
6	$Q + \alpha O_2 \rightarrow \beta CO + \gamma H_2O$
7	$Y + \alpha O_2 \rightarrow \beta CO + \gamma H_2O$
8	$CO + \frac{1}{2}O_2 \rightarrow CO2$
9	$CO_2 \rightarrow CO + \frac{1}{2}O_2$

$RR_1 = 1/(1/K_{1a} + [F]^{a1}[O_2]^{b1}K_{1b})$	$K_{1a} = A_{1a}e^{B_{1a}/T}$
	$K_{1b} = A_{1b}P^{n_{1b}}e^{B_{1b}/T}$
$RR_2 = [F]^{a2}[I]^{c2}K_2$	$K_2 = A_2P^{n_2}e^{B_2/T}$
$RR_3 = [Q]^{d3}K_3$	$K_3 = A_3e^{B_3/T}$
$RR_4 = [I]^{c4}K_4$	$K_4 = A_4e^{B_4/T}$
$RR_5 = [F]^{a5}[O_2]^{b5}K_5$	$K_5 = A_5P^{n_5}e^{B_5/T}$
$RR_6 = [Q]^{d6}[O_2]^{b6}K_6$	$K_6 = A_6e^{B_6/T}$
$RR_7 = [Y]^{e7}[O_2]^{b7}K_7$	$K_7 = A_7e^{B_7/T}$
$RR_8 = [CO]^{f8}[O_2]^{b8}K_8$	$K_8 = A_8e^{B_8/T}$
$RR_9 = [CO_2]^{g9}K_9$	$K_9 = A_9e^{B_9/T}$

Figure 2.4: *Reaction rates for the Functional Global Autoignition Model*

- post cool flame ignition delay with enhanced reactivity
- rate of heat release for cool flame and main ignition
- effects of pressure, fuel-air ratio and residual exhaust gas dilution.

The FGAM was able to fit the overall ignition delay profiles generated by the LLNL Detailed Kinetic Mechanism [24] (including 2 single stage fuels) to within 10-25% which was considered very good given that the difference between successive detailed Kinetic mechanisms can be as much as 35% [21]. It was thus proposed that the FGAM could be calibrated to fit any given fuel (including real multicomponent gasoline fuels) provided enough information on the autoigntion behaviour of the fuel was available from either experiments or DKM simulations.

Even with the large uncertainty in the accuracy of Detailed Kinetic Models, they are still considered the best comparison for validation of reduced kinetic and other autoignition models. This is because sufficient experimental data to cover the entire autoignition range would have to be compiled from several devices each with its own experimental uncertainty [23].

2.4 Octane Rating

The Octane rating of a fuel is a measure of its resistance to knock. Octane Number (ON) is measured according to 2 standardised tests: ASTM 2699 [3] for measuring Research Octane Number (RON) and ASTM 2700 [2] for measuring Motor Octane Number (MON). The tests measure the highest useful compression ratio in a standardised CFR engine under standardised test conditions *relative to* blends of iso-octane (high resistance to knock) and n-heptane (low resistance to knock). The blends of iso-octane and n-heptane are known as Primary Reference Fuels (PRFs). The designation PRF80 for example indicates a blend of 80% iso-octane and 20% n-heptane with an assigned RON and MON value of 80. The designation RON80 indicates the test conditions resulting in an Octane rating of 80 for the RON test, and similarly for MON80, the test conditions resulting in an Octane Rating of 80 for the MON test.

The operating conditions for both the RON and MON tests are given in Table 2.2. The 3 important differences between the two methods are: the higher engine speed for MON; that the spark timing is varied for the MON test but held constant for RON; that the *inlet air* temperature is controlled for RON whereas the *inlet mixture* temperature is controlled at a significantly higher temperature for MON. The importance of these differences will be elaborated on below.

An Octane test of an unknown fuel would proceed as follows:

Table 2.2: *Standard test conditions for measurement of Octane Number via the Research and Motor methods*

Parameter	RON	MON
Engine Speed	600 rpm	900 rpm
Spark Timing	13° BTC	14-26° BTC
Compression Ratio	4-18	4-18
Inlet Air Temperature	52°C	38°C
Inlet Mixture Temperature	-	149°C
Inlet Pressure	atmospheric	atmospheric
Air-Fuel Ratio	For max knock	For max knock

1. The engine is run at the appropriate speed and inlet conditions under stoichiometric conditions for the fuel being tested.

2. The compression ratio is steadily increased until knock is detected and the knockmeter registers a reading of 50, which corresponds to Standard Knock Intensity (SKI).

3. The air-fuel ratio is adjusted to achieve the maximum level of knock.

4. The compression ratio is adjusted once again to achieve standard knock intensity.

5. At the same compression ratio, two PRF blends within 2 ON, that would bracket the Octane reading of the fuel, are selected and run in the engine.

6. The Knock Intensity (KI) of the two reference fuels are recorded and the Octane number of the unknown fuel is determined by interpolating between the KI values.

2.4.1 The CFR Engine

The standardised CFR engine is purpose built for conducting the RON and MON tests. The first such engine was built in 1929 [41], and although several modifications to the control and measurement systems have been made since, the engine itself has remained mostly unchanged, in keeping with the standardisation of the test methods.

It is a single cylinder engine with adjustable compression ratio, achieved by moving the entire cylinder and cylinder head either up or down to change the clearance volume. The piston and cylinder head flame face are both nominally flat and the spark plug is mounted on the side of the cylinder. The longer flame path from the spark plug to the opposite wall, in addition to the slower engine speed and heated inlet, create conditions that induce knock at lower compression ratios than standard production engines. Dimensions of the CFR engine are given in Table 2.3.

Figure 2.5: *The CFR engine [42]*

Table 2.3: *Primary dimensions and valve timings of the CFR Engine. All timings referenced to TDC during combustion stroke*

Dimension	Value	Unit
Bore	82.5	mm
Stroke	114.3	mm
Conrod Length	254	mm
Inlet Valve Diameter	34	mm
Exhaust Valve Diameter	34	mm
Inlet Valve Lift	6.045	mm
Exhaust Valve Lift	6.045	mm
IVO	370	CAD
IVC	574	CAD
EVO	140	CAD
EVC	375	CAD

Figure 2.6: *Shrouded inlet valve of the CFR engine*

Air is drawn in from the atmosphere and heated to the prescribed inlet temperature. Fuel is introduced into the air-stream via a venturi type carburettor. For the MON test, where mixture temperature is controlled, the air-fuel mixture passes another heater where it is controlled to the required temperature.

The mixture enters the engine cylinder through a special inlet poppet valve. The valve features a shroud over one half of the flow area. This serves to direct the incoming air away from the spark plug and around the cylinder, generating a high degree of swirl inside the engine. The reduced flow area also impedes the incoming inlet charge. Together with the lack of inlet and exhaust valve overlap, this would reduce the volumetric efficiency of the engine, resulting in a higher than expected residual exhaust gas fraction.

Fuel is stored in one of three selectable bowls, from which it flows into a float chamber. The air-fuel ratio is changed by adjusting the height of the fuel bowls. From the float chamber the fuel is introduced into the air stream through the venturi. Liquid fuel evaporates in the manifold and partly inside the cylinder during the compression stroke [8].

Knock Measurement System

The knock measurement system consists of several components. The *detonation pickup* is positioned in the center of the cylinder head. The pickup transmits a signal, proportional to the rate of change of pressure, to the *detonation meter*. The detonation meter processes the signal electronically, including a band pass filter to remove the low frequency portion of the signal associated with compression and expansion in the reciprocating engine. Importantly it also reduces the high frequency component associated with the pressure oscillations following knock [10].

The signal is further processed and is output to the *knockmeter*, which displays a knock intensity value between 0 and 100. Standard Knock Intensity (SKI) is defined as a reading of 50 on the knockmeter. In order to account for variances between measurements in different tests and CFR engines, there are two primary adjustment dials for the knockmeter output. The METER dial adjusts the gain so that the knock intensity of a known fuel can be adjusted to SKI at its critical compression ratio (CCR) to form a reference point. This is usually performed using a PRF90 blend at its critical compression ratio of 6.64 for RON and 6.76 for MON. The SPREAD dial adjusts the sensitivity of the knockmeter and for the Octane Rating tests it is usually set to give a change of 10 to 18 knockmeter divisions per ON [2, 3].

2.4.2 Octane Sensitivity

Given the different operating conditions used in their respective tests, the RON and MON values determined for a given fuel are often quite different. This is quantified by the Sensitivity (S) defined by

$$\mathrm{S} = \mathrm{RON} - \mathrm{MON} \tag{2.3}$$

The sensitivity of the PRF blends are 0 by definition. Most fuels tested have a higher RON than MON and so have a positive sensitivity though there are some exceptions [43]. Commercially available gasoline in South Africa has a sensitivity in the range of 8-12 [44].

When these methods were introduced in 1929 [41], the test conditions were fairly representative of the operating conditions in the engines of the time. The higher temperature of the MON test accounted for the heated carburetors of early engines. As engine technology improved with multi-port fuel injection replacing carburettors, the prevailing engine conditions gravitated toward those represented by the RON test [4].

Kalghatgi [5] proposed an Octane Index measure (OI = RON - KS) where K is a constant typical of a given engine and operating condition and S is the sensitivity. For $0 \leq \mathrm{K} \leq 1$, this would result in a linear interpolation between RON and MON. Turbocharged and Direct Injection Spark Injection (DISI) engines (with higher operating pressures and lower temperatures) experience knock outside of the original RON/MON operating envelope [11]. Thus, as is more often the case, $\mathrm{K} < 0$ for modern engines. This would require an extrapolation beyond the description space of RON and MON. In order to ensure that this extrapolation is indeed valid, it is extremely important to understand the underlying cause of fuel sensitivity.

Given that the RON and MON test conditions lie within the NTC region of paraffinic fuels, Swarts and Yates [10] as well as others have proposed that sensitive fuels, which generally exhibit single stage or reduced 2-stage autoignition behaviour, react differently

to the change in operating conditions between MON and RON. Mittal et al [43] concluded that the sensitivity of a fuel can be attributed to the relative rate of change of autoignition delay with temperature in the NTC region. In contrast, it has been suggested by Moran and Taylor [45] that sensitivity can be attributed to the evaporative cooling potential of the fuel.

2.4.3 Experimental Studies of the Octane Rating Process

The RON and MON tests are not merely measurements of autoignition delay but also the severity of knock produced in the CFR engine when the fuel autoignites. This is affected by various additional engine effects. In order then to quantitatively assess the relative contribution of these different effects (fuel evaporation, autoignition behaviour and engine effects) an investigation of the actual Octane rating procedures must be performed. This has previously been undertaken by Swarts, Yates and co-workers [6–12].

One of the key observations of this work is the fact that knock manifests differently in the CFR engine to that in modern production engines [8]. When knock occurs in modern engines, a small fraction (in the region of 5%) autoignites suddenly, resulting in a very high pressure rise rate followed by high magnitude pressure oscillations in the engine cylinder giving the characteristic knock sound. In the CFR engine a much larger portion of the endgas (30-70%) is involved in the knock event. The pressure rise rate is noticebly less than the near-instantaneous rate seen in modern engines.

Figure 2.7 shows a representation of typical severe knock in standard production SI engines. The near instantaneous pressure rise rate can be seen, as well as the fact that the subsequent pressure oscillations are of the same magnitude as the initial pressure spike. In contrast, Figure 2.8 shows a representation of knock manifestation in the CFR engine. Arrigoni et al [46] specifically noted that the pressure rise due to knock in the CFR engine takes place over a finite period and that the subsequent pressure oscillations are of lesser magnitude.

In addition, by examining the knock measurement system in the CFR engine, it was concluded that the knock intensity reading was a function of the initial pressure rise rate of the post knock point pressure development and not the later pressure oscillations [10]. This is in contrast with modern knock sensors, which are designed to detect the high frequency oscillations of knock ringing [11].

Returning then to the previous definition of knock, a distinction can be made between knock as measured by a knock sensor in a standard production engine and knock as measured by the knockmeter in the CFR engine. In production SI engines, the measured knock is largely due to *knock ringing* resulting in vibrations picked up by the knock sensor. By contrast, the measured knock in the CFR engine is more strongly associated with the steep pressure rise immediately after the knock point.

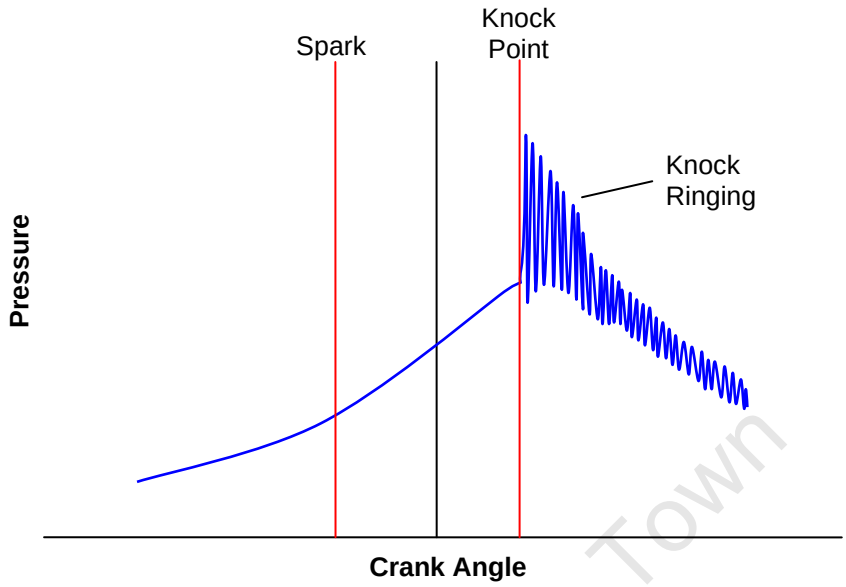

Figure 2.7: *Diagrammatic representation of knock manifestation in a standard production SI engine*

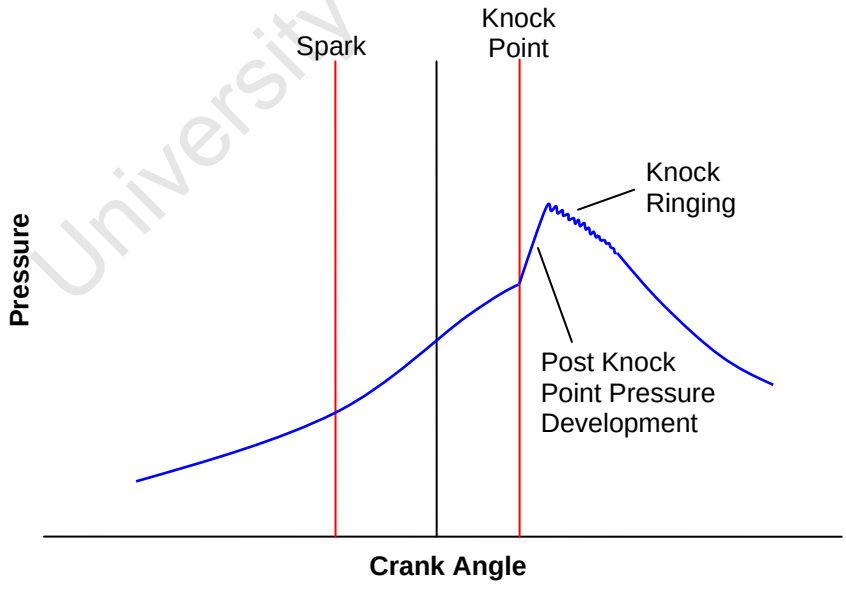

Figure 2.8: *Diagrammatic representation of knock manifestation in the CFR engine*

A representative simulation of the Octane measurement process should therefore be able to reproduce this characteristic pressure development at the knock point if the same metric of knock intensity is to be used. It was proposed by Swarts et al [12] that this pressure development was due to a "cascading autoignition" caused by an in-cylinder temperature gradient. This temperature gradient could be created by in-cylinder fuel evaporation and heat transfer during the intake and compression stages, and thereafter maintained by the slow engine speed and the high swirl generated by the shrouded inlet valve.

Konig et al [47] performed an experimental study investigating three modes of autoignition, initiated at exothermic centres, applicable to SI engines. *Thermal Explosion* occurred at high mean end-gas temperature and small temperature gradients, and was equivalent to homogeneous autoignition of the entire end-gas. *Developing detonation* occurred at intermediate end-gas temperature and intermediate temperature gradient, and resulted in a strong shock wave propagating from the centre. *Autoignitive deflagration* occurred under conditions of low mean end-gas temperature and large temperature gradients, and resulted in a relatively weak pressure wave propagating from the centre.

It was proposed in [47] that the manifestation of knock in standard production engines causing serious engine damage is a result of the developing detonation mode of autoignition. In the context of the current study, it is proposed that the manifestation of knock in the CFR engine is a result of the deflagration mode of autoignition and that this is in fact the same phenomenon as cascading autoignition.

2.5 Engine Modelling

2.5.1 Modelling Approaches

Various types of engine model have been utilised in the study of engine knock and octane number. In a study of autoignition in a motored engine, Curran et al [48] considered the engine as a homogeneous reactor whose volume is altered to simulate piston motion using the volume formulation derived by Heywood [1] . A detailed kinetics mechanism was then used to model autoignition. In consideration of a motored engine, the assumption of a single homogeneous zone is more appropriate than in a spark ignition engine, however it is noted even here that temperature and species inhomogeneities may have led to a discrepancy between the modelled and experimental results.

Hajireza et al [49] proposed a zero-dimensional two-zone model consisting of a burned zone and an unburned zone for the modelling of combustion through SI flame propagation. The flame front is considered to be infinitely thin. As normal combustion occurs, mass and enthalpy are transferred from the unburned zone to the burned zone, converting unburned reactants to combustion products. Heat Transfer is assumed to occur via forced induction

between the walls and flame front and the unburned zone as well as radiative heat transfer to the walls from the burned zone. A reduced kinetics model is used in both burned and unburned zones. In the unburned zone this is used for the modelling of autoignition, whereas in the burned zone it is used for control of the final burned temperature through consideration of dissociation reaction. These researchers further extended the model to the inclusion of a 3rd zone to represent a thermal boundary layer [50] in recognition of the fact that the temperature in the unburned zone would not be perfectly homogeneous.

The 2-zone approach has been widely utilised by other researchers. Swarts et al [51] used a conservation of ignition delay approach with a 3-Arrhenius Autoignition Model and a fuel life function to describe flame propagation. Yates et al [52] also used a conservation of ignition delay approach with the improved Empirical ID model and a Wiebe function description of flame propagation. D'Errico et al [53] used a detailed kinetic model to describe autoignition and a flame area growth model. Mittal et al [43] used a CID approach with ignition delays pre-calculated using a detailed kinetic model. These models all performed very well in predicting the timing of autoignition and correlated well with experimental results. However little to no emphasis was placed on accurately predicting the rate of heat release during the knock event. The 2-zone approach also does not allow for the simulation of in-cylinder temperature gradients so none of these models could be used directly to investigate the cascading autoignition phenomenon in the CFR engine.

As mentioned previously, Lafossas [38] was able to implement a CID approach in CFD engine simulations. This was achieved by modelling the production of a precursor species (Y) at a rate inversely proportional to the ignition delay calculated at the local conditions. This could be done in each computational element and the precursor species could be dealt with by the standard methods of species transport. Autoignition was taken to have occurred when the concentration of Y reached some critical value, at which point the energy of combustion was released. This implementation used a simple single Arrhenius description of ID in a region of the temperature-pressure domain where this would be a reasonable approximation. As a result, prediction of knock correlated well with experimental data under the conditions considered. It cannot, however, be necessarily assumed that such an approach would be as effective in applications where a single Arrhenius ID model provides very poor prediction of ignition delay.

Outside the sphere of SI combustion, the study of autoignition, especially concerning rates of heat release and the effects of temperature inhomogeneities, is of particular importance to Homogeneous Charge Compression Ignition (HCCI) engines [17]. In fact the more gradual heat release due to autoignition in HCCI engines [22] is similar to the cascading autoignition phenomenon of interest in the CFR engine. There is thus value in considering the approaches used in the modelling of HCCI engines.

Aceves et al [54] used a quasi-dimensional multi-zone approach and a DKM to simulate HCCI combustion. Using the results of a CFD simulation of the engine without autoignition

reactions, the cylinder was divided into multiple zones with similar temperature histories. The DKM was then applied individually in each of these zones so that autoignition could be predicted in each. All zones were however coupled by the mass, energy and volume balances imposed on the system. The model was applied to simulating the operation of a single cylinder HCCI engine running on natural gas fuel. In this way, the researchers were able to simulate a more gradual overall pressure rise due to autoignition, similar to that seen in their experimental data.

Several other researchers have also applied a similar multi-zone approach to HCCI modelling. Mehl et al [55] used a 1-D thermo-fluid model to obtain initial conditions at IVC and investigated various options in stratification of the fresh charge into multiple zones. Xu et al [56] compared the performance of single-zone and multi-zone models with experimental data. Again the multi-zone model was shown to much better simulate the gradual pressure rise rate during autoignition, seen in the real engine data, than a single zone model. Simulations with a small number of zones showed distinct autoignition events in each of the zones, resulting in non-smooth pressure development during the combustion period. The effects of different temperature distributions between the zones was also investigated and shown to affect the phasing and rate of pressure development during autoignition.

In the transition between SI and HCCI operation, there can exist a phase during which combustion is initiated by a spark and normal flame propagation ensues before a significant fraction of the end-gas autoignites [57]. This can be utilised in the mode of operation known as *spark-assisted HCCI*. The operating conditions resulting in this behaviour usually involve high residual exhaust gas fraction achieved through negative valve overlap (NVO) [57]. These 2 stages of heat release, from flame propagation and then autoignition, closely resemble the knocking pressure development in the CFR engine. Glewen et al [58] used a double Wiebe function description to describe this 2 stage heat release and using various combinations of Wiebe coefficients, were able to match the heat release rates observed in experimental operation over a range of SI-HCCI combinations.

2.5.2 Modelling of Combustion through Flame Propagation

A key aspect of any SI engine model is how the normal combustion through flame propagation is described. Here again there are 2 main paths that can be followed. Either the flame itself can be modelled or an empirical correlation with observed burn rates in a given engine can be used. The first approach has the advantage that for different fuels and operating conditions, the basic properties of the fuel-air mixture can be used to model the combustion development, provided the cylinder geometry and in-cylinder charge motion can be adequately described. Empirical correlations of burn rate are often much simpler, more computationally efficient and do not necessarily require an understanding of the in-cylinder charge behaviour. The difference in burn rates of different fuels and under different operating conditions may be difficult to describe though.

Turbulent Combustion Modelling

The modelling of combustion in a turbulent environment is a complex undertaking, requiring consideration of both the fluid mechanical behaviour and combustion chemistry. Veynante and Vervisch [59] present an excellent summary of the various models available (up to 2002) to deal with these coupled systems in premixed, non-premixed and partially premixed turbulent combustion.

SI combustion in the CFR engine is nominally premixed and turbulent flame regimes in premixed combustion are linked to various time and length scales. Many current combustion models are of the "flamelet" variety. Recent examples include the Universal Coherent Flamelet Model proposed by Teraji et al. [60] and the combustion model used by Perini et al [61] and others [53,62,63] based on a fractal approach to flame surface wrinkling.

Due to the requirement of modelling the fluid dynamics of the system, many of the combustion models require implementation in a 3D CFD code. The model described in [61] however was implemented in a quasi-dimensional framework and so could possibly have been used in the multi-zone model.

In this quasi-dimensional model an initial flame shape was assumed. For a centre mounted spark plug, the symmetric geometry allowed for the assumption of a spherical flame front, truncated by the cylinder walls and piston. Because of the symmetrical geometry, the effect of in-cylinder charge motion could largely be ignored, except in the calculation of turbulence.

Much experimental work has been performed measuring *laminar flame speed* under a range of different temperatures, pressures and equivalence ratios for various fuels and correlations are available [61,64] to easily determine these. A fractal based flame surface approach was adopted in [61] to calculate the *turbulent burning velocity* based on the laminar flame speed. In this way the propagation of the flame through the cylinder could be predicted.

Empirical Burn Rate Correlations

In many cases a complete description of the propagating flame is not necessary and all that is required is a description of the Mass Fraction Burned (MFB) at each point. This can be derived empirically from pressure traces from the modelled engine under the required operating conditions. From a given pressure trace, the Rassweiller and Withrow method described in [7] can be used to calculate the MFB at each crank angle (θ).

$$\mathrm{MFB}_\theta = \frac{\sum_{i=ign}^{i=\theta} \Delta P_{c,i}}{\sum_{i=ign}^{i=EOC} \Delta P_{c,i}} \tag{2.4}$$

$$\Delta P_{c,i} = \left(P_i - \left(\frac{V_{i-1}}{V_i} \right)^n P_{i-1} \right) \left(\frac{V_{i-1}}{V_{TDC}} \right) \tag{2.5}$$

where	ign	is the crank angle at which ignition occurs
	EOC	is the crank angle at end of combustion
	$P_{c,i}$	is the pressure rise attributed to combustion
	P	is the cylinder pressure
	V	is the cylinder volume
	n	is the polytropic coefficient of the compression and expansion portions of the cycle
	i	is the crank angle position index

The standard mathematical approximation of burn rate profiles is the Wiebe function [1].

$$\chi_\theta = 1 - e^{-a\left(\frac{\theta - \theta_{ign}}{\Delta\theta_{burn}}\right)^{m+1}} \tag{2.6}$$

where	χ	is the Wiebe function
	θ_{ign}	is crank angle at ignition
	$\Delta\theta_{burn}$	is burn duration
	a	is a tunable constant
	m	is a tunable constant

This produces an S shaped curve that describes combustion initiation, acceleration and deceleration. The constants a and m can generally be tuned to fit most observed burn profiles for normal combustion. During abnormal combustion such as knock though, the rapid heat release due to autoignition cannot be described by a Wiebe function. Swarts et al [8] proposed that the Fuel Life Function developed by Oppenheim and Kuhl could better describe the MFB profile of a knocking pressure trace. However if the description of normal combustion is only required up till the point of knock, then the Wiebe function is a sufficient descriptor of MFB.

In the CFR engine, the side mounted spark plug and high level of swirl make flame development difficult to predict through the flamelet models, designed for centre mounted spark-plugs, described in the previous section. Some assumptions could be made and an appropriate model adapted to the CFR geometry. However, such a modelling exercise would be outside the scope of this study, as a Wiebe function description would be sufficient to characterise the autoignition event.

2.5.3 Modelling of the CFR Engine

The CFR engine has been the subject of several modelling efforts due to its role in the Octane rating process and its use as a single cylinder research engine in a variety of other applications. Some of the modelling approaches and results are relevant to this study.

Hsiao [65] conducted studies using 2 and 3-zone models as well as a CFD model to investigate the flame shape that best described combustion in the CFR engine. The CFD model confirmed the high degree of in-cylinder swirl set up by the shrouded inlet valve. The velocity of the swirling gas decreased as the piston approached TDC but a cylindrical profile varying uniformly with radius was clearly set up as shown in Figure 2.9.

Investigations of the flame shape revealed that a reversed cylindrical burn profile, beginning at the walls and burning in toward the center, matched observed experimental results well for lower compression ratios whereas a planar profile, burning from one side of the cylinder to the other, worked better for higher compression ratios. These profiles are shown in Figure 2.10. It was proposed that the high swirl would transport the flame from the side mounted spark plug around the cylinder and then burn inwards, resulting in the reversed cylindrical profile. At higher compression ratios, the reduced swirl velocities would lessen this effect and so the flame would propagate more directly across the cylinder.

Additional results from this CFD study not published in [65] but presented as an appendix in [51] show an in-cylinder temperature gradient at IVC of 20 K and, under motored conditions, a temperature gradient at TDC of 40 K. Although the temperature distribution was not as uniformly cylindrical as the velocity profile it could still be approximated as cylindrical.

Mehl et al [66] used a 2-zone model with detailed chemical kinetics in the unburned zone to predict knock. Inlet conditions were simulated using a 1-dimensional fluid dynamics model, simulating unsteady compressible flow in the intake system but not including fuel evaporation. Flame propagation was modelled using a fractal based wrinkled flame front approach similar to that of Perini et al [61] described above. Previous work by this group [62] indicated that inclusion of the chemical kinetic reactions in the unburned zone was necessary in order for the combustion model to match experimental results even in non-knocking traces.

This model was then applied to the Octane Rating tests. Good correlation to the critical compression ratios of the PRFs was claimed, using a proxy for SKI of 30% of the unburned gas autoigniting at knock point. The RON and MON values of a gasoline surrogate (13% n-heptane, 42% iso-octane, 13% MTBE and 32% toluene) were also reasonably predicted.

These results are questionable though given the experimental results of Swarts et al [10] showing as much as 70% of the unburned gas involved in the knock event. No attempt was

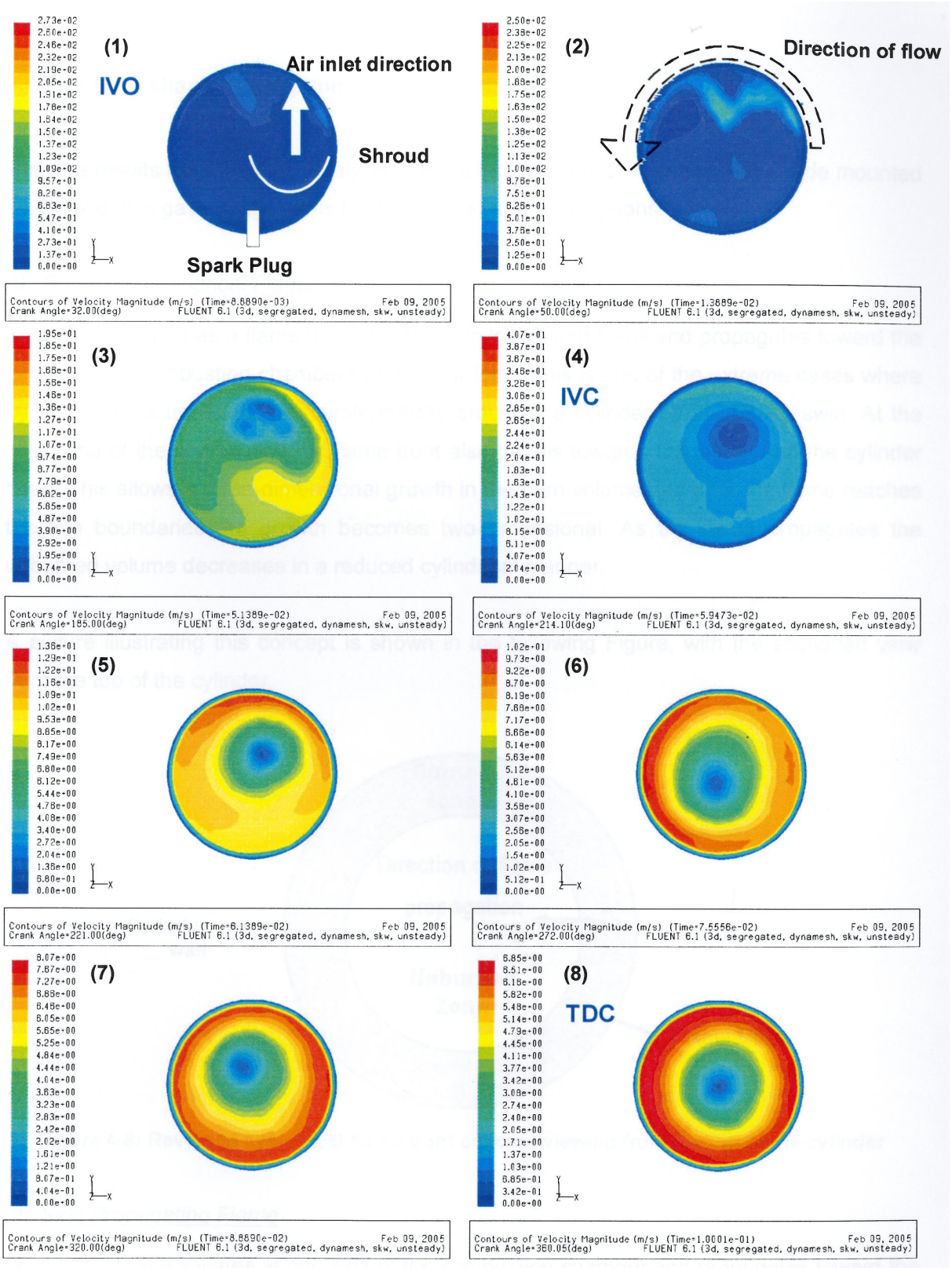

Figure 2.9: *CFD modelling results showing flow development inside the CFR engine with contours showing velocity magnitude. Reproduced from [65]*

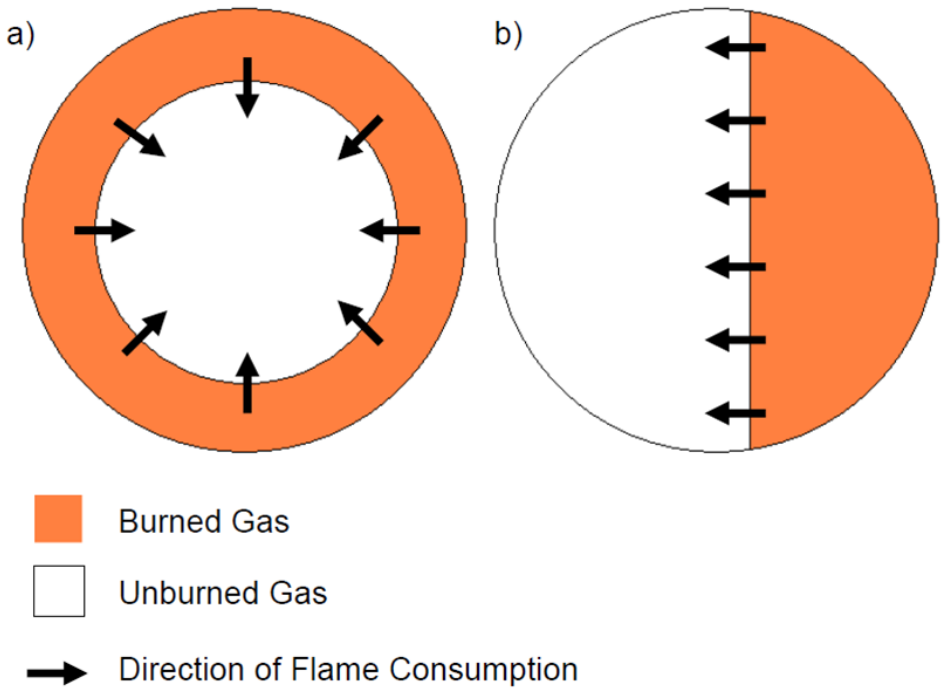

Figure 2.10: *Flame shape models proposed by Hsiao [65]: a) reversed cylindrical burn profile, b) planar burn profile*

made to simulate the post-knock pressure development as simulations were stopped at the point of autoignition. Furthermore, it was specifically stated that a multi-zone approach was not adopted due to the already great computational expense of the DKM utilised.

In an investigation of Octane sensitivity Mittal and Heywood [43] also used a 2-zone model but instead of using a DKM directly in the simulation, the ignition delay profiles of the fuels were generated prior to the engine model being run. A conservation of ignition delay integral was then utilised to predict the onset of autoignition in the engine model. The RON96 test was chosen for simulation as the compression ratios of RON96 and MON96 are very similar. Three fuels with a RON of 96 and varying sensitivity were selected: PRF96, TRF96 (a blend of toluene and n-heptane) and a blend of ethanol and n-heptane.

It was also assumed that knock intensity was proportional to the mass fraction of unburned gas involved in the autoignition event. It was not clearly stated what flame propagation combustion model was used but it is assumed that the same burn rate was applied for all fuels tested as the CAD at which autoignition occurred was used as the metric of knock intensity. At the inlet air temperature of the RON test, the CAD of autoignition were quite similar for all three fuels

The effects of changes in inlet air temperature were then investigated and, as expected, it

was found that the CAD of autoignition decreased (autoignition occurred earlier) with an increase in inlet temperature. However the fuels with higher sensitivity were more sensitive to these changes in temperature. At temperatures below that of the RON test, sensitive fuels experienced autoignition later than the PRF. At temperatures higher than that of the RON test (such as would be the case in the MON test) autoignition occurred earlier for sensitive fuels than the PRF.

It was thus concluded that it was this differing response to the inlet temperature conditions of the RON and MON tests that accounted for octane sensitivity. An analysis of the autoignition profiles of the various fuels in the transition region (moving into and out of NTC behaviour) was then performed and it was found that as fuels increased in sensitivity, the minimum value of $\mathrm{d}ln(\tau)/\mathrm{d}ln(1/T)$ also increased. Sensitive fuels therefore were the fuels that exhibited less pronounced NTC behaviour. This is a qualitatively strong argument but only considers the RON96 case and does not quantitatively allow for the knock performance of a sensitive fuel under differing conditions to be gauged.

Swarts [51] used a 2-zone model with conservation of ignition delay integral applied to the Yates 3-Arrhenius autoignition model [11] to interpret the results of the experimental work presented in [12]. Consideration was given in this study to the possibility of temperature gradient being the cause of cascading autoignition. A basic analysis concluded that, under an adiabatic zone assumption, a temperature gradient of 40 K at IVC was required to reproduce the post knock pressure development seen in the CFR engine. As it was noted that this was higher than the 20 K gradient predicted by the CFD study of [65], a *heat loss* gradient was instead proposed.

It was also noted that the initial temperature at IVC required to produce autoignition for the PRFs at the knock point was in the region of 450 K to 470 K for the RON test. This is significantly higher than the specified inlet temperature of 325 K. For the MON test, initial temperature at IVC was required to be between 500 K and 550 K for the PRFs. Additionally, the TSFs considered consistently required initial temperatures 20-40 K higher than the equivalent PRF to autoignite at the appropriate point. Accurate specification of the initial conditions in a model simulating the Octane tests would thus seem to be highly important.

2.6 Optimisation and Solving Algorithms

In producing a computational model, various numerical methods are required in solving the governing equations and optimising any calibration parameters to best describe the system. The choice of these methods, as with the choice of which actual submodels to use, usually involves a trade-off between accuracy and simulation time. As a description of these algorithms is not essential for an understanding of the research work, a detailed description is provided instead in Appendix B.

2.7 Alternate Engine Technologies

This work was primarily concerned with modelling of the CFR engine, which utilises the traditional spark-ignition technology of gasoline engines. However the approach adopted, and described in the remainder of this thesis, may be applicable to other engine technologies, where the manner in which autoignition manifests (not just the autoignition timing) is important to the operation of the engine.

The technologies of HCCI and spark-assisted HCCI have already been described in this chapter. Like in the CFR engine, the pressure rise after the initial onset of autoignition is more gradual than would be the case if the entire cylinder contents autoignited at once. Multi-zone models [54–56,67] have been applied to simulate in-cylinder temperature gradients to reproduce this pressure development and were shown to perform better in this respect than single zone models [56]. However they may benefit from use of a more computationally efficient autoignition model than the detailed and reduced kinetic models currently used.

Another interesting engine technology (still in development at the time of writing) is the Mazda SKYACTIV-G gasoline engine concept [68]. This engine uses an extremely high compression ratio of 14:1. Operation at such a high compression ratio would theoretically result in an increase in efficiency but would be prevented in practice in standard production engines by the onset of severe knock [1]. It is claimed that the SKYACTIV-G is able to avoid knock through three main strategies [69].

1. **Shortening burn duration**: Various means are used to create a more homogeneous mixture such as intensifying air flow, increasing injection pressure, use of multi-hole injectors and a piston cavity to prevent flame impingement of the piston.

2. **Reduction of residual exhaust gas**: This is accomplished using a long 4-2-1 exhaust system to improve the exhaust breathing process. Here the significant role that residual exhaust gas can play in the onset of knock is acknowledged.

3. **Retarding spark timing**: The spark timing is heavily retarded, even after TDC under certain conditions. This would normally result in a much reduced torque and efficiency but it is claimed that this is offset by "low-temperature oxidation reactions" releasing heat before actual spark ignition. It has been argued in [37] and [21] that the post cool flame reactivity of a mixture is significantly enhanced and this may also assist in increasing the flame speed during normal combustion and so reducing the burn duration.

This last point is quite important as the cool flame is actively utilised in the knock prevention strategy of the SKYACTIV-G engine concept. Some of the results of this study regarding the possible effects of the cool flame on the Octane rating process may therefore be directly relevant to this concept and these are discussed in Chapter 7.

Chapter 3

The Multi-Zone Engine Model

This chapter describes the computational model that was developed to simulate the Octane rating tests with the intent of reproducing the characteristic pressure development of knock in the CFR engine.

3.1 Model Description

It was proposed that the non-instantaneous pressure rise at the knock point in the CFR engine under Octane rating conditions is the result of a cascading autoignition caused by a temperature gradient within the engine cylinder. A suitable model would therefore require a description of such a temperature gradient. This was accomplished by use of a quasi-dimensional multi-zone model. This approach was a combination of the 2-zone models traditionally used in the description of normal SI engine combustion through flame propagation [49] and the multi-zone models used in the description of HCCI combustion with thermal and species stratification [54].

The unburned gas in the cylinder was divided into multiple zones by volume. The division was done so as to nominally represent an annular distribution of zones within the cylinder (as shown schematically in Figure 5) but the zones themselves had no geometric description and so were quasi-dimensional. The outer most zone represented a thermal boundary layer for purposes of heat transfer to the cylinder walls. The other zones were modelled as adiabatic with no mass transfer between the unburned zones. The low engine speed and high swirl generated by the shrouded inlet valve was assumed to maintain the effectively cylindrical separation of the zones. A more comprehensive CFD type simulation of the combustion and flow within the CFR engine may inform a more accurate description of the interaction between the zones.

These zones were then each assigned unique initial temperatures to represent an initial thermal gradient at Inlet Valve Closure (IVC). Note that that the specification of different initial temperatures and no heat transfer between zones was different to the method

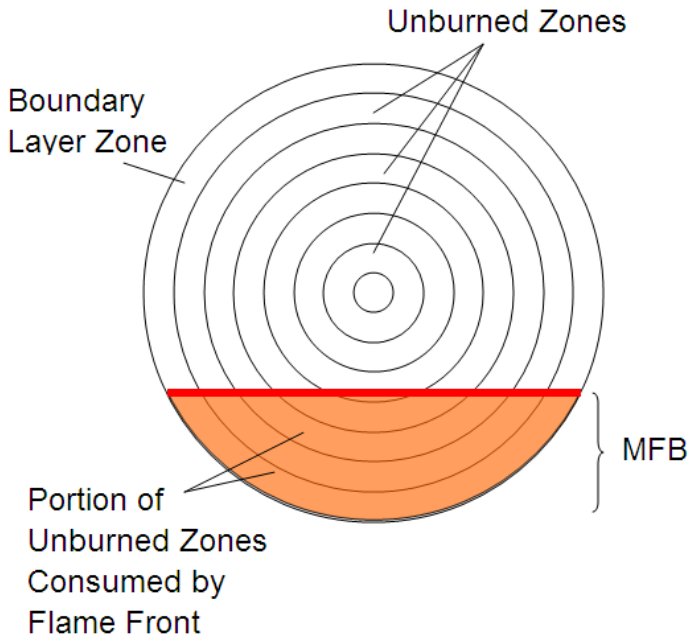

Figure 3.1: *Schematic of concentric unburned zone reference layout showing linear consumption by the advancing flame front*

suggested in [51] of stipulating different polytropic coefficients for the different zones to create a heat transfer gradient.

Normal combustion was simulated by means of a Wiebe Function description of Mass Fraction Burned, with coefficients fit to experimental pressure trace data. For a given mass fraction burned, a proportional amount from each of the unburned zones was transferred to a single burned zone. An equilibrium approach using the CO_2 dissociation and Water-Gas Shift reactions was used to determine the temperature of this burned zone.

In order to predict the onset of autoignition and therefore knock, the Functional Global Autoignition Model (FGAM) was implemented in each zone. The reactions specified by the FGAM were allowed to proceed in each of the zones according to the temperature, pressure and species concentrations. This would serve to predict both the timing and heat release associated with autoignition.

The final model was implemented as shown in Figure 3.2.

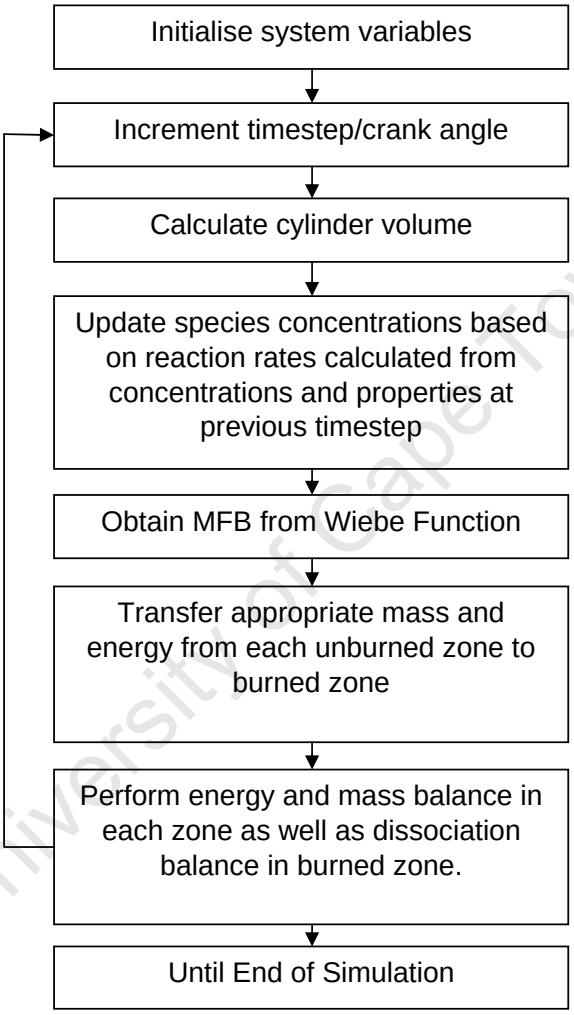

Figure 3.2: *Simulation algorithm of the Multi-zone Engine Model*

3.2 Governing Equations

Piston Motion

At each time step, the cylinder volume is calculated by the formula given in [1]

$$\frac{V_{cyl}}{V_c} = 1 + \frac{1}{2}(r-1)\left[R_{cc} + 1 - \cos\theta - \sqrt{R_{cc}^2 - \sin^2\theta}\right] \tag{3.1}$$

where V_{cyl} is cylinder volume
V_c is clearance volume
r is compression ratio
R_{cc} is conrod-crank length ratio
θ is current crank angle

Energy Balance

For each zone i and timestep s an energy balance is set up

$$Q - \left(\frac{P_{i,s} + P_{i,s-1}}{2}\right)(V_{i,s} - V_{i,s-1}) - (m_{i,s}u_{i,s} - m_{i,s-1}u_{i,s-1} + \delta m_{out}h_{out} - \delta m_{in}h_{in}) = 0 \tag{3.2}$$

where Q is heat transfered into the zone
P is pressure
m is mass
u is internal energy
h is enthalpy
δm is mass transferred
$_{in}$ is a subscript referring to transfer into the zone
$_{out}$ is a subscript referring to transfer out of the zone

Note that although there is no mass transfer from one unburned zone to another, there is mass transfer from each of the unburned zones to the burned zone in order to describe the combustion event. For each of the unburned zones then, $\delta m_{in} = 0$ and for the burned zone, $\delta m_{out} = 0$.

Ideal Gas Law

An equation for the ideal gas law in each zone, at each timestep is set up

$$P_{i,s}V_{i,s} - m_{i,s}R_{i,s}T_{i,s} = 0 \tag{3.3}$$

where R is the mixture gas constant
T is temperature

Volume Balance

The zones were coupled by setting the pressure in each zone to be equal to the total cylinder pressure and by the volume balance

$$V_{cyl,s} - \sum_{i=1}^{n\ zones} V_{i,s} = 0 \tag{3.4}$$

This assumption of constant pressure throughout the cylinder at any moment does not allow for pressure discontinuities and thus shock waves. The model would thus not be able to capture the knock ringing portion of the knock event. As mentioned previously though, the knock intensity reading on the CFR engine is determined by the post knock point pressure rise and not the subsequent knock ringing [10]. The constant pressure assumption should therefore not affect the application of the model to simulation of knock in the CFR engine. This would not necessarily be the case for standard production engines where knock ringing is important. It should be noted though, that typical alternative 2-zone models [43, 53] end the simulation at the point of autoignition and are therefore equally unable to simulate knock ringing.

Flame Propagation

The flame propagation of normal combustion was modeled by means of a Wiebe function representing the mass fraction burned (MFB).

$$\chi = 1 - e^{-a\left(\frac{\theta-\theta_{ign}}{\Delta\theta_{burn}}\right)^{m+1}} \tag{3.5}$$

where
- χ is the Wiebe function
- θ_{ign} is crank angle at ignition
- $\Delta\theta_{burn}$ is burn duration
- a is a tunable constant
- m is a tunable constant

The values of a, m, θ_{ign} and $\Delta\theta_{burn}$ were tuned to match experimental data.

The flame front was regarded as being infinitely thin and consumed mass in the unburned zones in a linear fashion as shown in Figure 3.1. For each MFB value, the segment corresponding to the MFB of the total cylinder volume was calculated and overlaid on the reference zone distribution profile (based on the initial annular division of the cylinder into zones). The appropriate incremental mass and enthalpy from each of the unburned zones lying within the burned segment was then transferred to the burned zone. An enthalpy balance involving the change of species from reactants to products accounted for the heat of combustion.

Note that this does not necessarily mean that the flame itself proceeded linearly. As the flame front expands, it compresses the unburned gas ahead of it. This together with the swirl generated by the shrouded inlet valve would distort any original geometric distribution of the unburned zones. The zone consumption profile of the reference configuration would therefore not be the same as the geometric flame development profile. With the side mounted spark plug of the CFR, a simple linear consumption profile, as proposed by Hsiao [65], was used as the best first approximation.

Burned Zone Composition and Temperature

In the burned zone, the Water-Gas Shift ($CO + H_2O \rightleftharpoons CO_2 + H_2$) and CO_2 dissociation ($CO_2 \rightleftharpoons CO + \frac{1}{2}O_2$) equilibrium reactions were used to determine the final burned temperature by minimizing Gibbs Free Energy and balancing C, H and O atoms. This resulted in the following set of equations:

$$K_{P,WGS} - \frac{N_{CO_2}N_{H_2}}{N_{CO}N_{H_2O}}\left(\frac{P}{P_{atm}N_{tot}}\right) = 0 \tag{3.6}$$

$$K_{P,COD} - \frac{N_{CO}N_{O_2}{}^{\frac{1}{2}}}{N_{CO_2}}\left(\frac{P}{P_{atm}N_{tot}}\right)^{\frac{1}{2}} = 0 \tag{3.7}$$

$$n_C - (N_{CO} + N_{CO_2}) = 0 \tag{3.8}$$

$$n_H - (N_{H_2O} + N_{H_2}) = 0 \tag{3.9}$$

$$n_O - (N_{CO} + 2N_{CO_2} + N_{H_2O} + 2N_{O2}) = 0 \tag{3.10}$$

where
- $K_{P,WGS}$ is the equilibrium K_P value for the Water-Gas Shift equilibrium
- $K_{P,COD}$ is the equilibrium K_P value for the CO_2 Dissociation equilibrium
- N_{CO_2} is the number of moles of CO_2
- N_{CO} is the number of moles of CO
- N_{H_2O} is the number of moles of H_2O
- N_{H_2} is the number of moles of H_2
- N_{O_2} is the number of moles of O_2
- n_C is the number of C atoms (a constant at each timestep)
- n_H is the number of H atoms (a constant at each timestep)
- n_O is the number of O atoms (a constant at each timestep)

Heat Transfer

Heat loss was assumed to occur from the burned zone and the designated boundary layer unburned zone only. A Woschni correlation [1] was used to calculate the convective heat transfer coefficients as follows:

$$h_c = 3.26B^{-0.2}P^{0.8}T^{-0.55}w^{0.8} \tag{3.11}$$

where h_c is the convective heat transfer coefficient
B is the cylinder bore
P is the instantaneous cylinder pressure
T is the instantaneous zone temperature
w is given by:

$$w = \left[C_1 S_p + C_2 \frac{V_d T_r}{P_r V_r} \left(P - P_m \right) \right] \tag{3.12}$$

where S_p is the piston speed
V_d is the displaced volume
T_r is a reference temperature
P_r is a reference pressure
V_r is a reference cylinder volume
P_m is the instantaneous cylinder pressure of an equivalent motored cycle
C_1 is a calibration coefficient
C_2 is a calibration coefficient

The proportional cylinder wall area was apportioned between the burned and unburned zones on a cylinder volume fraction basis. Although the coolant temperature for both RON and MON tests are specified at 100°C, a wall temperature of 150°C was used, based on experimental measurements using surface thermocouples in the CFR [70].

It is acknowledged that in only considering heat transfer from the designated "boundary layer zone" the total heat transfer from the cylinder would be underestimated. In this initial model, interaction between the different unburned zones through mass and heat transfer were intentionally excluded in order to simplify the autoignition chemistry calculations within each zone and due to uncertainty of what these actual interactions would be. It is expected that further development of this model will include such inter-zone interactions and thus better quantify the heat transfer effects.

Solving the Physical Equation Set

For n unburned zones then, there would be n temperatures, n volumes and the overall cylinder pressure values to solve at each timestep. Additionally for the burned zone, 5 concentration variables need to be solved for. This gives a total of $2n + 6$ variables.

A total of n energy balances, n ideal gas law balances, 1 volume balance, 3 atom balances and 2 equilibrium balances also gives $2n + 6$ equations to solve. Such a system of N equations in N unknowns could be solved by a multi-variable Newton's Method [71] by iteratively setting until convergence

$$\mathbf{x}_{n+1} = \mathbf{x}_n + \mathbf{J}_n^{-1} \left(-\mathbf{f}_n \right) \tag{3.13}$$

where **x** is the vector of variables
f is the vector of functions to be set to 0 (ie. the balance equations)
J is the Jacobian matrix of F

Autoignition Chemistry

In each unburned zone the chemical reactions specified by the FGAM were allowed to proceed with reaction rates calculated from the instantaneous temperature, pressure and species concentrations. For a given reaction

$$a_1X_1 + a_2X_2 \rightarrow a_3X_3 + a_4X_4 \tag{3.14}$$

where the X's are reaction species
the a's are stoichiometric coefficients

The reaction rate (RR) was calculated by

$$RR = [X_1]^{n_1}\,[X_2]^{n_2}\,P^{n_p}Ae^{-B/T} \tag{3.15}$$

where n_1, n_2, n_p, A and B are reaction rate coefficients

For each species X then, its rate of change of concentration with time was calculated by

$$\frac{d[X]}{dt} = \sum_{i=1}^{n\ reactions} b_i RR_i \tag{3.16}$$

Where the b_i were the number of moles of X in the reaction equation of reaction i (the corresponding a value in Equation 3.14). If X was a reaction product, $b_i > 0$; if X was a reactant, $b_i < 0$ and if X was not involved in the reaction then $b_i = 0$.

In each zone a system of ordinary differential equations of species concentration with respect to time was thus defined. The differential equations were then solved within each chemical timestep before the physical balances, described in the sections above, were used to solve the pressures, volumes etc. in the next physical timestep. An energy balance was performed in each unburned zone at the end of each chemical timestep to realize any heat release from the intermediate reactions. To increase the resolution of the chemical timescale, multiple chemical timesteps were taken within each physical timestep based on the adaptive timestep method described in Appendix B.3.2. Once an unburned zone had reached a critical temperature (in this case set to 1500 K) it was regarded as having autoignited and its contents were set to the same fractions as the burned zone to ensure the correct final burned temperature.

3.3 Calculation of Thermodynamic Properties

The thermodynamic properties of the chemical species used in this model were obtained from the NIST-JANAF tables [72]. Of principal importance were the values of specific heat capacity at constant pressure (C_p), enthalpy (h), internal energy (u), entropy (s) and Gibbs Free Energy (G). The JANAF Tables give the values of C_p as a function of temperature through a polynomial function of the form

$$C_p = a_0 + a_1 T + a_2 T^2 + a_3 T^3 + a_4 T^4 \tag{3.17}$$

It is these polynomial coefficients $a_{1..5}$ that are listed in the JANAF tables. Sensible enthalpy ($\hat{h}$) is obtained through integration of the relation

$$\mathrm{d}\hat{h} = C_p \mathrm{d}T \tag{3.18}$$

to obtain

$$\hat{h} = a_0 T + \frac{a_1 T^2}{2} + \frac{a_2 T^3}{3} + \frac{a_3 T^4}{4} + \frac{a_4 T^5}{5} + constant \tag{3.19}$$

The constant of integration is obtained by noting that at the standard state ($T = 298\mathrm{K}, P = 1\mathrm{atm}$) the total enthalpy of a substance is equal to its enthalpy of formation (h_f^0). The total enthalpy at a given temperature can thus be written as

$$h(T) = h_f^0 + \hat{h}(T) - \hat{h}^0 \tag{3.20}$$

where $\hat{h}^0$ is the sensible enthalpy at 298 K.

The internal energy can easily be obtained through the relation

$$u = h - RT \tag{3.21}$$

where R is the gas constant.

In order to obtain values for entropy it is noted that for an isentropic process,

$$\delta q = T \mathrm{d}s \tag{3.22}$$

where from the conservation of energy,

$$\delta q = \mathrm{d}u + P \mathrm{d}v \tag{3.23}$$

Further noting that

$$\mathrm{d}h = \mathrm{d}u + P \mathrm{d}v + v \mathrm{d}P \tag{3.24}$$

rearrangement yields

$$\mathrm{d}s = \frac{\mathrm{d}h}{T} - \frac{v\mathrm{d}P}{T} \tag{3.25}$$

$$= \frac{C_p\mathrm{d}T}{T} - \frac{R\mathrm{d}P}{R} \tag{3.26}$$

Substituting in the representation of C_p, considering the entropy at atmospheric pressure s^0 and integrating gives

$$s^0 = a_0 \ln T + a_1 T + \frac{a_2 T^2}{2} + \frac{a_3 T^3}{3} + \frac{a_4 T^4}{4} + s_f^0 \tag{3.27}$$

The Gibbs Function at atmospheric pressure (g^0) can be obtained by taking the definition

$$g^0 = h^0 - Ts^0 \tag{3.28}$$

The K_P values for the equilibria considered in the burned zones can be obtained by noting that

$$K_P = e^{-\Delta G^*/R_u T} \tag{3.29}$$

where

$$\Delta G^*_{WGS} = g^0_{CO_2} + g^0_{H_2} - g^0_{CO} - g^0_{H_2O} \tag{3.30}$$

$$\Delta G^*_{COD} = g^0_{CO_2} - g^0_{CO} - \frac{1}{2} g^0_{O_2} \tag{3.31}$$

for the Water-Gas Shift and CO_2 Dissociation equilibria respectively.

3.4 Object Oriented Implementation

The multi-zone engine model was implemented using a Microsoft Excel spreadsheet user interface, with all the actual calculations performed by Visual Basic for Applications (VBA) subroutines. The use of Object Oriented Programming (OOP) in VBA allowed for a modular approach to the model development. This would allow for different submodels to be used with minimal change to the rest of the code.

For example, in considering the thermodynamic behaviour of the system, the Engine contained a Cylinder. The Cylinder contained multiple Zones. Each Zone contained a Mixture. Each Mixture consisted of multiple Species. Each Species contained a set of Chemical Properties. `Engine`, `Cylinder`, `Zone`, `Mixture`, `Species` and `ChemProp` were all implemented as object classes.

When, for example, the C_p value of a particular zone was required, the `Zone` object would call the C_p property of its `Mixture` member. The `Mixture` object, knowing how to calculate the C_p value of a mixture given the C_p values if its constituent species, would in turn call their C_p properties. Each `Species` object then called on the C_p function of its `ChemProp` member, which calculated the C_p value at the required temperature. This would be performed for each species and the results rolled up to give the final C_p value for the zone.

The advantage of this of approach is that if one only wanted to change the way in which say, the C_p value of nitrogen was calculated, this could easily be accomplished by changing the `ChemProp` member of the `Nitrogen` object and all the other code could remain unchanged. The `Nitrogen` object would otherwise resemble a typical member of the `Species` class. Similarly if a different flame propagation model were to be implemented, only the `CombEvent` object would require change.

A description of each of the object classes used in this model, as well as its properties, methods and dependencies, are given in Appendix C. This, together with the the description of the methods used above, would enable the replication of the multi-zone engine model in virtually any programming language.

Chapter 4

Engine Model Calibration and Parametric Study

This chapter describes how the multi-zone model was calibrated to simulate the operation of the CFR engine under the ASTM Octane Rating test conditions. The results of a parametric study are then presented to show that the model responded appropriately to changes in operating and simulation parameters.

4.1 Experimental Data

A large collection of knocking and non-knocking CFR pressure traces from previous studies [6–12] was used to calibrate the model and validate its results. This data will hereafter be referenced as [73]. A description of the method used in the prior study is contained in this section. The subsequent analysis of the raw data, performed in this current work, is presented in Section 4.2

4.1.1 Experimental Setup

The experiments were performed in a modified CFR engine fitted with a water-cooled piezo-electric pressure transducer, positioned diametrically opposite the spark plug. The original detonation pickup for the knockmeter was left intact so that knock intensity readings could still be made and compared to the pressure readings.

The pressure readings were sampled using a 12 bit data acquisition card and coupled either to an external shaft encoder or an internal clock on the data acquisition board. The external shaft encoder provided signal pulses at 0.2 CAD intervals. The internal clock provided signal pulses at 50 kHz (0.02 ms intervals). An additional TDC marker was also sampled as a time position reference.

The higher timescale resolution of the internal clock provided more reliable data for calculation of pressure derivatives. However the large number of data points produced meant that the entire engine cycle could not be captured. Data sets captured with the internal clock thus all begin at TDC after the compression stroke. The compression and early combustion pressure development were not captured in these traces. Due to the drift inherent in the charge amplifier connected to the pressure transducer, there was also no way of setting a reference point for pressure traces starting at TDC. This signal could however be digitally differentiated and filtered to emulate the operation of the knockmeter system. The pressure traces coupled to the external shaft encoder were therefore used during the multi-zone model calibration. The filtered pressure trace from the internal clock coupled runs were used to compare the pressure rise rate results.

A lambda sensor was also connected to the exhaust system so that the air-fuel ratio could be measured. It was found that for the PRFs, maximum knock was achieved at a λ value of approximately 0.9 for the RON test and between 0.9 and 1.0 for the MON test. Test results used were therefore at these air-fuel ratios rather than under stoichiometric conditions as in the multi-zone model simulations. For the limited number of stoichiometric tests performed, the trends observed were consistent with the $\lambda = 0.9$ tests, although the actual values differed slightly.

4.1.2 Test Matrix

As it was important to compare the performance of PRFs to other fuels, the Toluene Standardisation Fuels (TSFs) were selected as a direct comparison. The Octane numbers of the TSFs are well documented and used in the calibration of the CFR engine itself. Additionally most of the TSFs had a sensitivity of approximately 10, which is quite similar to commercial gasolines. The PRF blends that were tested were thus selected to match either the RON or MON number of each of the TSF blends. There were some real gasolines and other fuel blends tested in the original experimental study but these have not been considered here. The fuels test results that were used for validation in this work are summarised in Tables 4.1 and 4.2.

In analysing the results of these tests, the noisy pressure traces were smoothed by averaging over 1 CAD intervals. The first and second derivative traces were then obtained by a three-point approximation. For the set of cycles in each test case, average values of Peak Pressure, Peak Pressure Rise Rate, Position of Knock Point and MFB at Knock Point were calculated. The knock point was assumed to coincide with the peak value of the 2nd derivative of pressure. MFB was calculated using the Rassweiler and Withrow method described in Equation 2.4.

Table 4.1: *Description of fuels used in the experimental study of [73]*

Designation	RON	MON	%iso-octane	%n-heptane	%toluene
TSF998	99.8	88.7	10%	16%	74%
TSF892	89.2	78.2	0	30%	70%
PRF100	100	100	100%	0	0
PRF97	97	97	97%	3%	0
PRF93	93	93	93%	7%	0
PRF89	89	89	89%	11%	0
PRF85	85	85	85%	15%	0
PRF78	78	78	78%	22%	0
PRF76	76	76	76%	24%	0
PRF67	67	67	67%	33%	0
PRF65	65	65	65%	35%	0
PRF58	58	58	58%	42%	0
PRF50	50	50	50%	50%	0
PRF40	40	40	40%	60%	0

Table 4.2: *CFR engine test results [73] used for calibration and validation of the multi-zone model*

Fuel	Test Condition	Comp Ratio	Air-Fuel Ratio (λ)	Signal Coupling
PRF100	RON100	7.82	0.9	int
PRF100	RON97	7.32	0.9	int
PRF100	RON93	6.87	0.9	int
PRF100	RON89	6.58	0.9	int
PRF100	RON85	6.34	0.9	int
PRF100	RON76	5.96	0.9	int
PRF100	RON65	5.66	0.9	int
PRF100	RON100	7.82	0.9	ext
PRF97	RON97	7.32	0.9	ext
PRF93	RON93	6.87	0.9	ext
PRF89	RON89	6.58	0.9	ext
PRF85	RON85	6.34	0.9	ext
PRF65	RON65	5.66	0.9	ext
PRF50	RON50	5.36	0.9	ext
PRF40	RON40	5.25	0.9	ext
TSF998	RON100	7.82	0.9	ext
TSF892	RON90	6.58	0.9	ext
PRF100	MON100	8.03	1.0	ext
PRF93	MON93	7.10	1.0	ext
PRF85	MON85	6.28	1.0	ext
PRF75	MON75	5.53	1.0	ext
PRF67	MON67	5.29	1.0	ext
PRF50	MON50	4.91	1.0	ext
PRF40	MON40	4.78	1.0	ext

4.2 Analysis of Experimental Results

Examples of typical knocking and non-knocking traces are presented in comparison with model results in Figures 4.5 and 4.6. The key measurable features of these traces are presented below for PRFs running under their respective Octane Number test conditions for both RON and MON. For each of the results presented, the standard deviation of the set of cycles was also calculated in order to gauge the distribution due to cycle-to-cycle variation. In the subsequent analysis, error bars on graphs represent 1 standard deviation in the distribution. It is important to note that the results presented here are for PRFs only and do not necessarily apply to other fuels.

Peak Pressure

The peak pressures recorded for PRFs running at SKI at their critical compression ratios are presented in Figure 4.1 for both RON and MON tests. As expected, the peak pressure increased with increasing Octane number and thus compression ratio. The RON peak pressures were consistently higher than those of the equivalent MON test. Although the critical compression ratios for MON are less than RON below an Octane Number of approximately 87, MON CCRs above this point are higher than those of RON so one would in turn expect higher peak pressures. It is possible that at the higher MON engine speed, the already compromised breathing process of the CFR engine is further reduced, leaving a larger residual exhaust gas fraction. Less combustible inlet gas in the cylinder would result in less heat liberated during combustion and thus lower peak pressures.

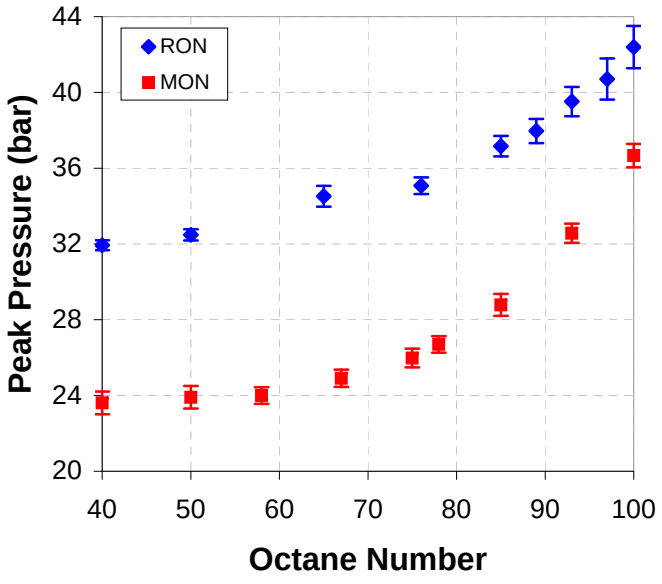

Figure 4.1: *Peak pressure for PRFs at standard knock intensity under RON and MON test conditions*

Peak Pressure Rise Rate

Peak knock pressure rise rates showed differing trends for RON and MON, as shown in Figure 4.2. Although generally of similar magnitude at Octane Numbers below 80, at ONs higher than this, increasing Octane Number resulted in increasing pressure rise rates for MON tests and decreasing pressure rise rates for RON tests. The reason for these diverging trends was uncertain. The standard deviation of peak pressure rise rate values between cycles was generally of the order of 1 bar/ms, which can be regarded as fairly consistent. For the sake of comparison it is worth noting that for the RON test at 600 rpm, 1 bar/ms is equivalent to 0.28 bar/CAD and for the MON test at 900 rpm, 1 bar/ms is equivalent to 0.19 bar/CAD.

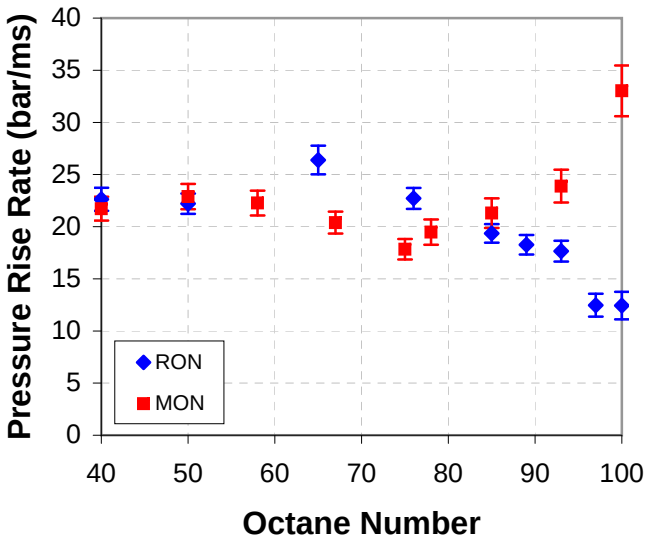

Figure 4.2: *Peak pressure rise rate at standard knock intensity under RON and MON test conditions*

Knock Point

The position of the knock point varied significantly for both RON and MON as seen in Figure 4.3 (though more so for MON). Although for RON it may be possible to discern a trend of later onset of knock with increasing Octane Number, the variation in knock point position for MON rendered any possible trend identification questionable. It is interesting to note that, though the cycle-to-cycle variation resulted in this large variation in knock point position, the peak pressure rise due to knock was far more consistent.

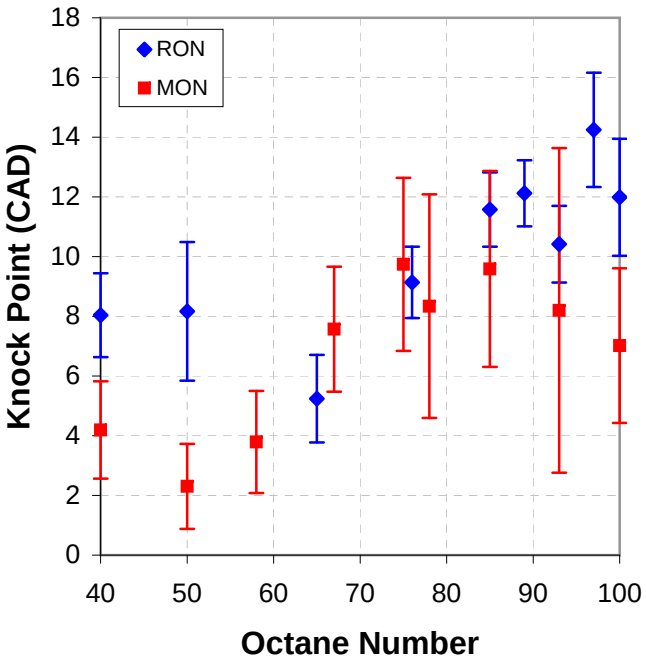

Figure 4.3: *Position of knock point for PRFs at standard knock intensity under RON and MON test conditions*

Mass Fraction Burned at Knock Point

If one assumes that the pressure rise rate due to knock is proportional to the fraction of end-gas involved in the knock event, then the analysis of the MFB at knock point (Figure 4.4) is consistent with the diverging peak pressure rise rate trends of RON and MON. For Octane numbers greater than 80, an increase in ON results in an increase in MFB at knock point for RON and a decrease for MON. Although the end-gas fraction involved in the knock event reduces to about 30% for RON100, knock in the MON test consistently involves more than 50% of the unburned charge. It is likely that the more consistent mass fraction burned values at knock point for MON are due to the changing spark advance applied in the MON test.

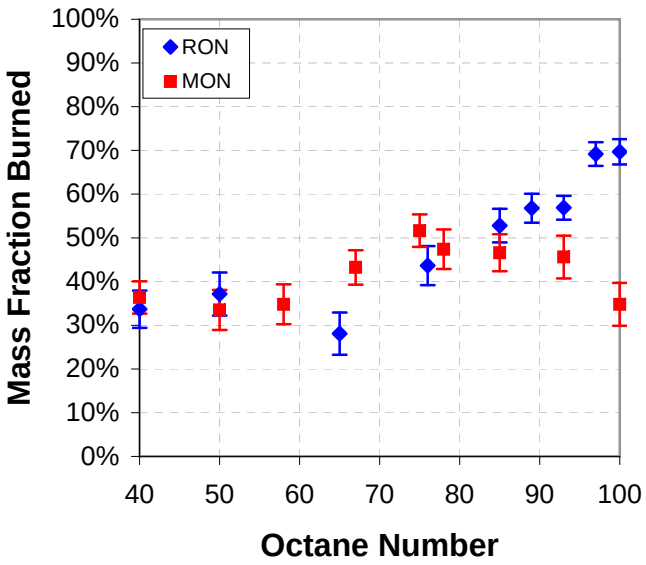

Figure 4.4: *Mass fraction burned at knock point for PRFs at standard knock intensity under RON and MON test conditions*

4.3 Model Calibration Methodology

The multi-zone model was calibrated to initially simulate the RON tests. Initial conditions at IVC were set to the initial conditions of the the test. A uniform temperature distribution was initially specified. Standard textbook values for the Wiebe combustion description and Woschni heat transfer description were also specified. The initial test to be calibrated on was RON100 as FGAM co-efficients for PRF100 (iso-octane) were already available, as was experimental data of PRF100 running under SKI knocking conditions at RON100 as well as PRF100 running without knock under RON80 conditions.

The simulation was then performed using 20 zones and 600 timesteps between IVC and EVO. The results were then compared to typical experimental pressure traces for the 2 test conditions considered.

The initial pressure values and Woschni coefficients were manually adjusted to better represent the compression phase of the engine cycle before combustion. The Wiebe coefficients were then adjusted to represent the combustion phasing in the non-knocking pressure trace. Parameters to be matched were: a) onset of observable combustion, b) CAD at 10% MFB, c) CAD at 90% MFB and d) overall pressure development.

It was found that by setting the Wiebe ignition timing to 5 CAD before actual spark timing, and using Wiebe a and m values of 9 and 5 respectively, a satisfactory description of non-knocking combustion could be achieved. The ignition timing used for RON simulation was thus set to -18 CAD in the model, instead of -13 CAD as specified in the ASTM standard [3]. By varying the value for burn duration, the cycle-to-cycle variation in the CFR engine could be reproduced. After initially fitting the non-knocking traces with a burn duration of 52 CAD, the burn duration was reduced to 48 CAD, in order to fit the knocking pressure traces. This was considered reasonable as the higher compression ratio under RON100 test conditions would likely result in a reduction in burn duration.

The initial temperature was adjusted so that the onset of autoignition would coincide with the knock point identified in the experimental trace. The temperature gradient was then increased. A more gradual pressure rise after the original point of autoignition was noted and the duration over which the remainder of unburned gas autoignited could be adjusted to match the post-knock-point pressure development of the experimental traces.

This was an important milestone in the model development as it showed that an in-cylinder temperature gradient, in combination with the operating conditions of the CFR engine under the RON test, could produce a cascading autoignition as simulated by the multi-zone model. Although this is insufficient to conclude that this is in fact the cause of the unique CFR knock pressure development, confirmation that such a temperature gradient is in fact set up and maintained would provide strong evidence for such a causal relationship.

It was at this stage noted that the pressure rise due to combustion that was predicted by the model was in the region of 10% to 20% higher than that seen in both knocking and non-knocking experimental traces. Adjustment to several of the operating parameters were attempted including initial temperature, initial pressure, heat transfer parameters and residual exhaust gas fraction. It was found that only by setting REG to 20% could the combustion pressure rise of the simulation be brought in line with the experimental traces. This is discussed further in the next section.

The procedure described above has been presented in a very linear fashion. However it is important to note that each of the model input parameters had an effect on each of the

behavioural attributes required to be described. In the initial stages of this study it was not clear what the magnitude and directionality of these effects would have necessarily been. An iterative approach of manual adjustment of the parameters, followed by simulation and comparison to experimental traces was thus adopted. This enabled an understanding of the above mentioned effects to be developed. Although an optimisation algorithm could have been applied to automatically solve for the appropriate parameters, it was considered beneficial to go through the manual adjustment process in order to gain this understanding.

4.4 Results of Calibration

Each engine model simulation was run from Inlet Valve Closure (IVC) to Exhaust Valve Opening (EVO). Determination of IVC cylinder temperature distribution and residual exhaust gas is extremely challenging to determine experimentally [9]. For this preliminary investigation, initial conditions were selected to best match experimental pressure traces and were checked against a basic engine breathing model and values from literature [74] to ensure these conditions were within reason.

The model parameters were adjusted to match the experimental runs of PRF100 knocking at SKI under RON100 conditions, and at RON80 test conditions to compare non-knocking traces. A comparison of the non-knocking and knocking RON pressure traces are given in Figures 4.5 and 4.6 and a list of the operating parameters used is given in Table 4.3.

Parameter	Value	Unit
IVC	-146	CAD
EVO	140	CAD
Engine Speed	600	rpm
Bulk Temperature at IVC	400	K
Temperature Gradient at IVC	20	K
Pressure at IVC	0.97	bar
REG fraction at IVC	20%	
θ_{ign}	-18	CAD
$\Delta\theta_{burn}$	48	CAD
Wiebe a	9	
Wiebe m	5	
Number of Unburned Zones	20	
Number of Timesteps	600	

Table 4.3: *Simulation parameters used in the multi-zone model to fit experimental pressure traces*

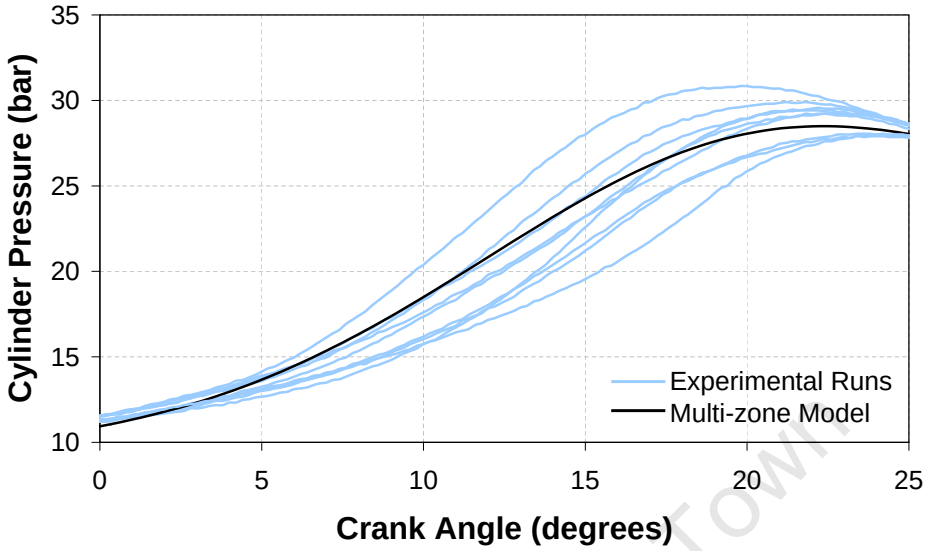

Figure 4.5: *Comparison of non knocking simulations in multi-zone model with experimental engine cycles of [73]. Iso-octane (PRF100) running under RON80 test conditions.*

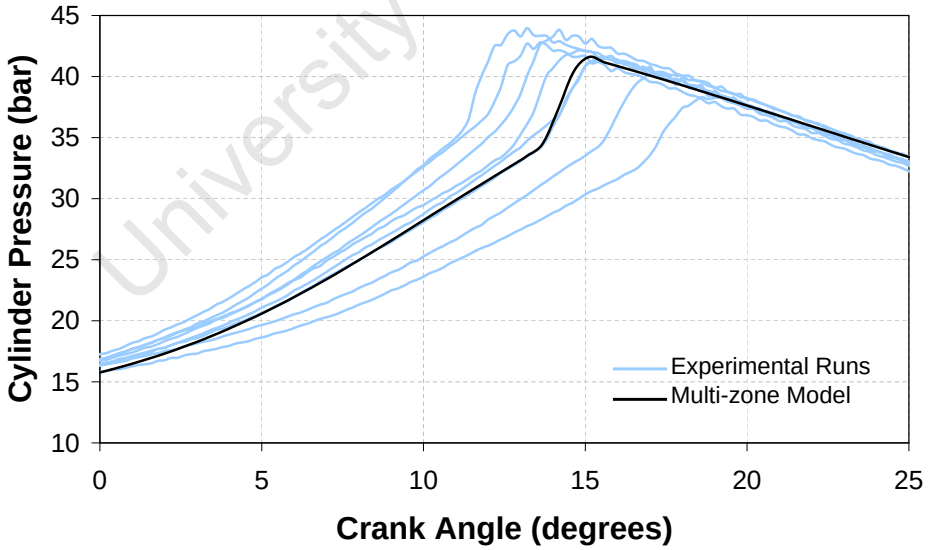

Figure 4.6: *Comparison of knocking simulations in multi-zone model with experimental engine cycles of [73]. Iso-octane (PRF100) running under RON100 test conditions*

Note that all experimental traces shown were run under identical conditions. The variation in these traces was purely due to cycle-to-cycle variation in the breathing and combustion processes. Figure 4.5 shows that the simulation parameters chosen resulted in a modelled non-knocking pressure trace that was approximately median in the distribution of experimental traces.

Figure 4.6 shows that the knock pressure development produced by the model was very similar to that seen in the experimental CFR pressure traces. The knock-point was clearly visible at 14 CAD for the modeled trace and the mass fraction burned at this point was 70%, which was the same as the average calculated from the experimental pressure traces using the Rassweiler and Withrow method described in [12]. However, as mentioned in the model formulation chapter (Section 3.2), the model results did not show any knock ringing.

It should be noted that the temperature gradient at IVC of 20 K is consistent with that determined by the CFD model of Hsiao [65] discussed in Section 2.5.3. Additionally the bulk gas temperature at IVC of 400 K is slightly less than determined by Swarts [51], but still significantly higher than the inlet air temperature of 325 K (51.7°C).

The Residual Exhaust Gas (REG) fraction of 20% may seem high and it is in fact higher than that predicted by the basic engine breathing model of 11%. This value was adjusted to reduce the pressure rise due to combustion in order to bring the model predictions in line with the experimental pressure traces. Adjustment to the REG value was more effective in this regard than adjustments to other values. This is further discussed in the next section.

It is notable in the appendix of Taylor [74] that describes the calculation of residual exhaust gas fraction, that the margin of error in this calculation at low engine speeds in the CFR can be very large with the maximum being just under 20%. The reduced flow area created by the shroud on the inlet valve and lack of valve overlap would also inhibit the normal breathing process and improve the likelihood that more residual exhaust gas would be retained in the cylinder for the next cycle. It was decided therefore to use this REG value for this initial study.

Figure 4.7 shows the temperature in each of the zones during the knocking simulation. The burned zone is shown in orange, the unburned zone used as the boundary layer is in green, the remainder of the unburned zones in purple and the average temperature in the cylinder is shown in black. Once a zone has been completely consumed by the flame front, the temperature trace appears to “flat-line” and remains constant till the end of the simulation. The actual value of this flat line temperature has no significance and the abrupt change in temperature at this point is merely a mathematical artifact caused by calculation in a zone with zero mass. This discontinuous behaviour does however provide a convenient way to identify the points at which each zone is fully consumed.

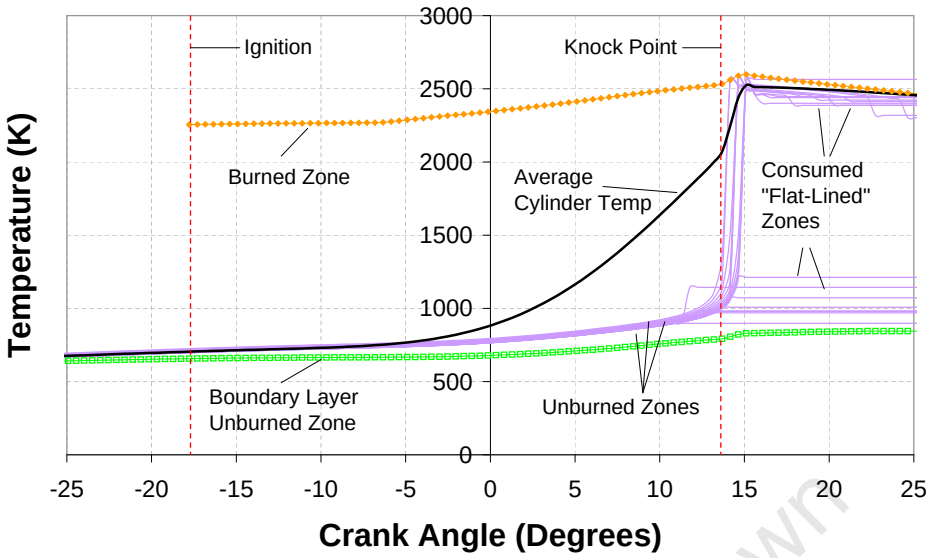

Figure 4.7: *Temperature development in each of the zones of the multi-zone model. Zones that flat-line have been completely consumed by the flame front. Simulation parameters are for PRF100 running under RON100 test conditions.*

An analysis of these temperature traces clearly showed multiple autoignition events in succession after the knock point, simulating a cascading autoignition. By looking at the average cylinder temperature in Figure 4.7 it is apparent how this phenomenon results in the same pressure development as the knocking CFR engine. Simulations run with smaller timesteps (as shown in Figure 4.8) proved that it was not simply the timestep spacing that dictated the timing of the separate autoignition events and thus the rate of knock pressure increase.

A set of simulations were performed to identify the minimum number of zones required in the multi-zone model. The pressure traces generated are shown in Figure 4.9. Using more zones than necessary would obviously require unnecessary computational expense. Simulations with 1 and 2 unburned zone produced the same type of results as in [15] with the entire unburned end-gas autoigniting at once at the knock point. Simulations with 10 zones produced distinct autoignition events but this resulted in a non-smooth pressure development. This was similar to the results of [56] using 5 and 9 zone models to simulate HCCI combustion. Simulations with 20 unburned zones produced a smooth cascading autoignition pressure development and so this was the number of zones used in the rest of the study.

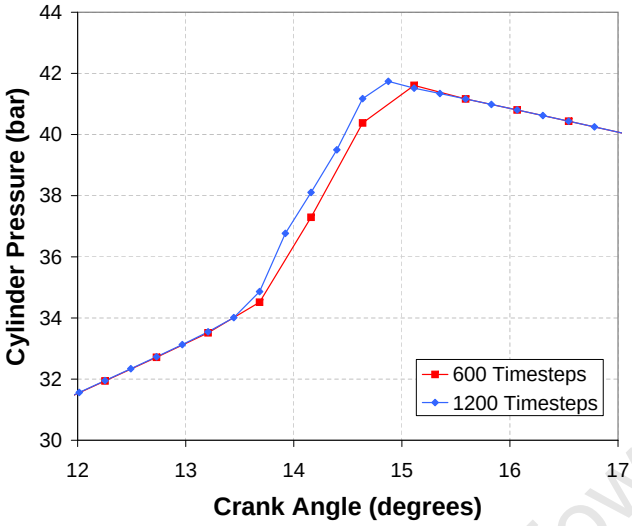

Figure 4.8: *Pressure traces showing pressure development during knock, generated by multi-zone model using 600 timesteps ($\Delta\theta$ = 0.5 CAD) and 1200 timesteps ($\Delta\theta$ = 0.25 CAD). Data points correspond to the actual simulation timesteps. Simulation parameters are for PRF100 running under RON100 test conditions.*

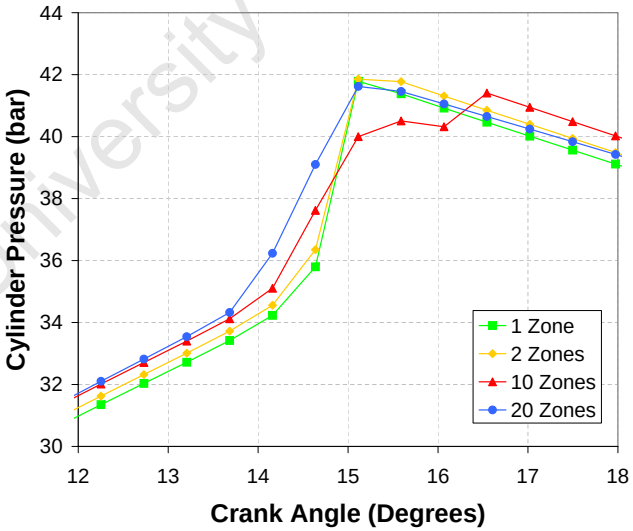

Figure 4.9: *Pressure traces showing pressure development during knock, generated by multi-zone model using 1, 2, 10 and 20 unburned zones. Data points correspond to the actual simulation timesteps. Simulation parameters are for PRF100 running under RON100 test conditions.*

4.5 Parametric Study

A parametric study was conducted in order to investigate how the model would react to a change in initial conditions and simulation parameters. A baseline run was performed with parameters for PRF100 fuel running at SKI under RON100 conditions with other conditions as given in Table 4.3. In each set of simulations, all parameters were kept at the same baseline value except for one which was varied within a given range. The independent influence of each of the model parameters could thus be assessed. Changes in the inlet temperature with inlet pressure held constant (and vice versa) would also be accompanied by a proportional change in inlet density and thus trapped mass in the cylinder. Although this would affect the total heat released during normal combustion and autoignition, the heat per unit mass would not be directly affected by this change in density.

Some of the results of this study provided possible explanation for the effect of the operating parameters on the cascading autoignition phenomenon. Other results, which may appear obvious, still had value in that they validated that the model responded to changes in the input parameters in the appropriate manner. The results of this parametric study are described below with graphs of the pressure trace and time resolved rate of change of pressure. In each of the figures, the dark (black) line represents the baseline case and the other results are represented by the lighter (blue) lines. The direction of change in the variable of interest is indicated by an arrow.

4.5.1 Compression Ratio

The compression ratio was varied between 7.0 and 8.4 in increments of 0.2 with the results shown in Figures 4.10 and 4.11. This is perhaps the most important response as it is the compression ratio at which Standard Knock Intensity is measured that determines a fuel's octane rating. Changing the compression ratio resulted in a uniform shift of the pressure trace during the normal combustion development. The knock-point occurred later with decreasing compression ratio resulting in a smaller fraction of unburned gas involved in the knock event.

Figure 4.11 shows how the maximum pressure rise rate due to knock reduced rapidly with decreasing compression ratio in a fairly linear manner. The decrease from a compression ratio of 7.8 to 7.0 (or equivalent RON from 100 to 94) resulted in a decrease in this maximum from 19.5 bar/ms to 8.5 bar/ms. It is important to note that fuels generally still exhibit knock in the CFR engine at compression ratios corresponding to several Octane numbers lower than rated. However the knock intensity recorded would be reduced, due to the lower knock pressure rise rate seen here.

The comparison in Figure 4.12 with experimental runs of PRF100 running at increased compression ratios revealed a similar trend. At compression ratios below 7, the peak pressure rise rate remained relatively flat around 5 bar/ms, associated with normal combustion.

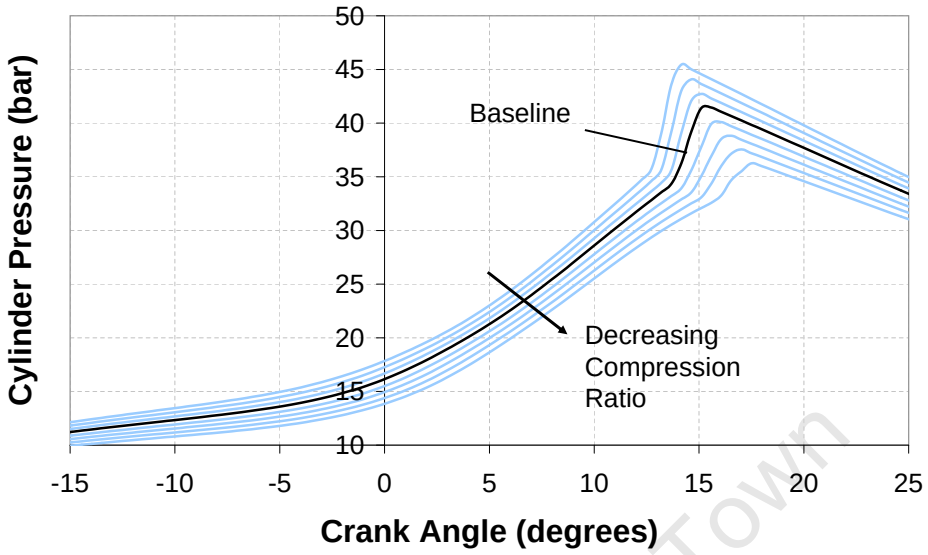

Figure 4.10: *Parametric Study: Effect of compression ratio on pressure trace. CR = 7.0 to 8.4 in increments of 0.2*

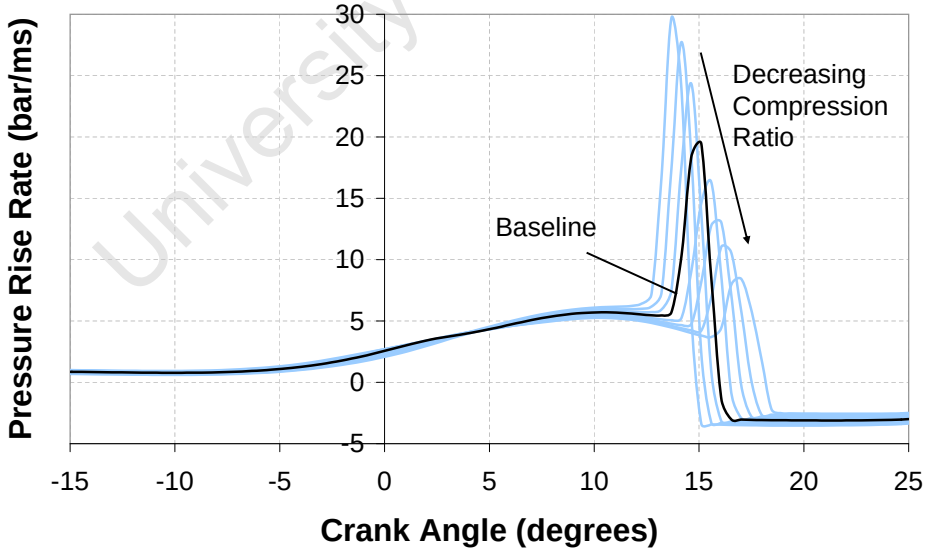

Figure 4.11: *Parametric Study: Effect of compression ratio on rate of change of pressure. CR = 7.0 to 8.4 in increments of 0.2*

Above this point, knock begins to occur and the peak pressure rise rate increases rapidly until SKI at the critical compression ratio (CCR). The response of the model to change in compression ratio was thus seen to be very similar to that of experiments.

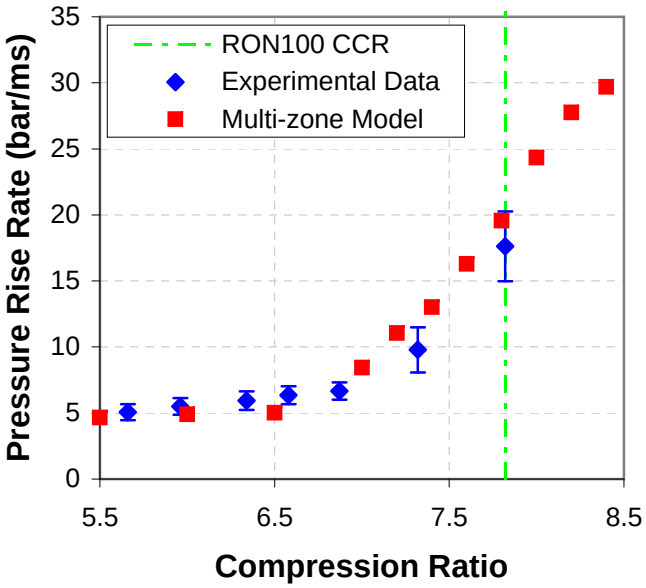

Figure 4.12: *Peak pressure rise rate for PRF100 running under various compression ratios compared with experimental data of [73]*

4.5.2 Burn Duration

The Burn Duration was varied between 45 CAD and 54 CAD in increments of 1 CAD, with the results shown in Figures 4.13 and 4.14. As expected, the pressure traces were identical until the start of combustion at which point normal combustion proceeded either faster or slower depending on the burn duration. The knock point in the modelled traces moved incrementally later with longer burn duration, though the intensity of knock appeared consistent.

The differences in pressure developments in Figure 4.13 were very similar to the cycle-to-cycle variation seen in Figure 4.6. Furthermore comparison of pressure rise rates from the model in Figure 4.14 and actual experimental cycles in Figure 4.15 confirmed this similarity. This suggests that cycle-to-cycle variation can be accounted for in the model by changes in burn duration.

This was an important result in this study as it reduced the need to accurately predict the burn duration for the different fuels and test conditions that were subsequently run.

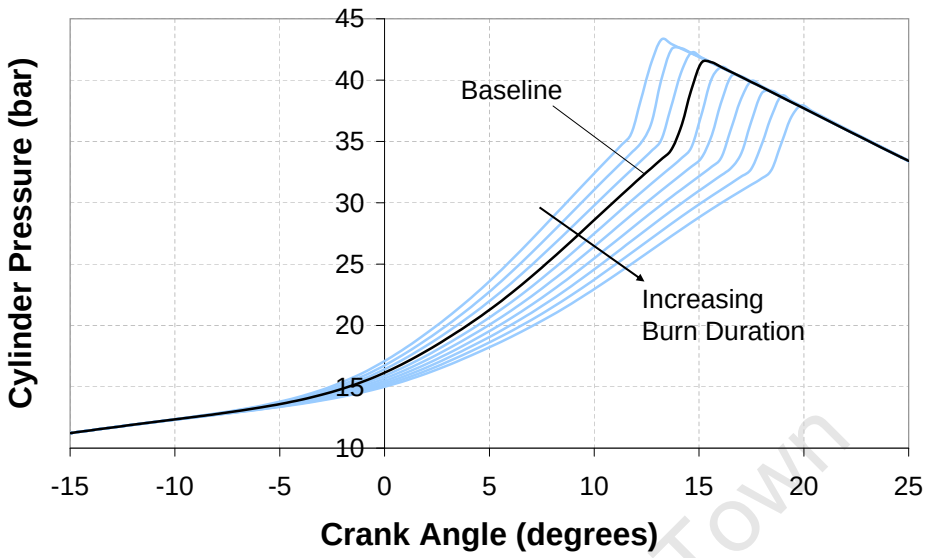

Figure 4.13: *Parametric Study: Effect of burn duration on pressure trace.* $\Delta\theta_{burn}$ *= 45CAD to 54CAD in increments of 1CAD*

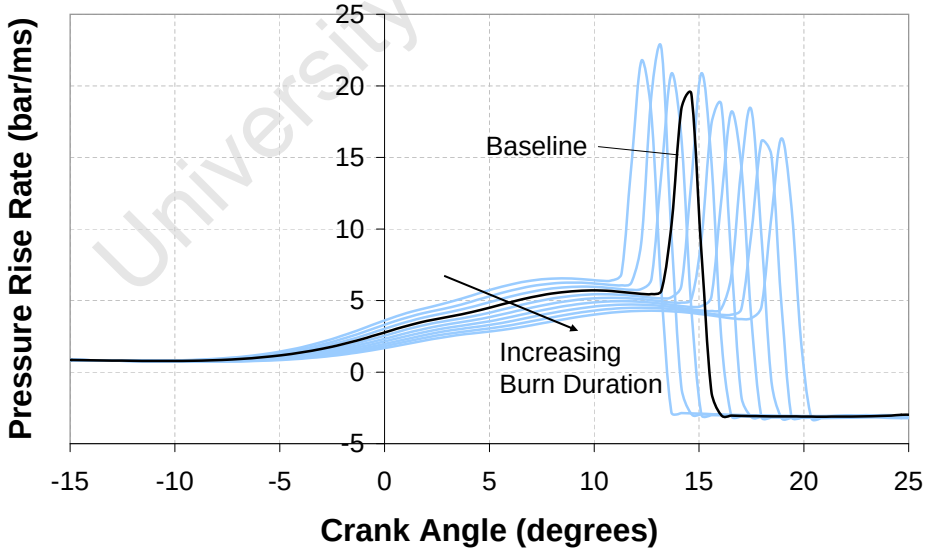

Figure 4.14: *Parametric Study: Effect of burn duration on rate of change of pressure.* $\Delta\theta_{burn}$ *= 45CAD to 54CAD in increments of 1CAD*

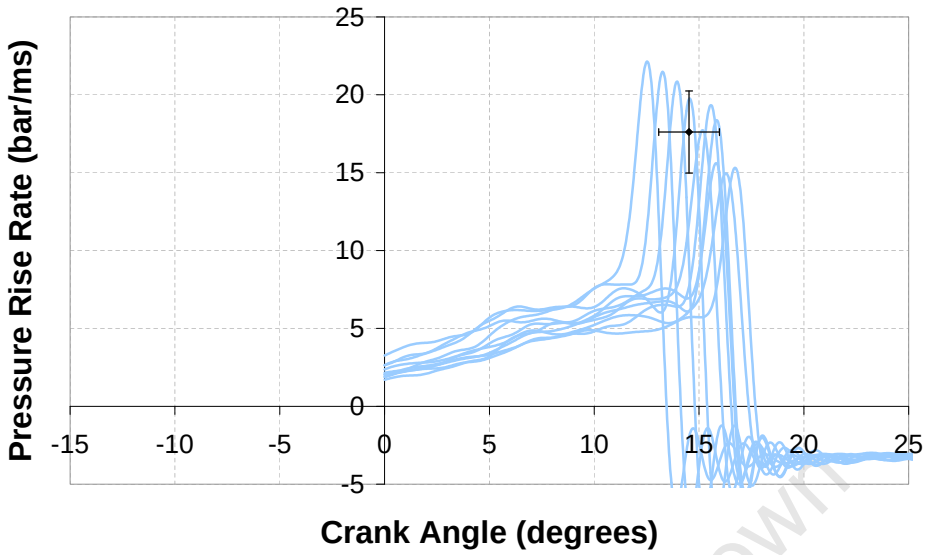

Figure 4.15: *Filtered rate of change of pressure traces for PRF100 under RON100 conditions from [73]. Error bars represent 1 standard deviation in position and magnitude of peak pressure rise rate for cycle-to-cycle variation.*

This further negated the need to deal with complex turbulent effects in the modeling of cycle-to-cycle variation.

4.5.3 Residual Exhaust Gas

Residual Exhaust Gas (REG) Fraction was varied between 5% and 35% in increments of 5%. The effect of REG fraction was much greater than initially anticipated. The dilution of unburned inlet charge with exhaust gas has the dual effect of reducing the amount of fuel which can combust to release heat and increasing the overall cylinder temperature at IVC. The results in Figures 4.16 and 4.17 show only the dilution effect with the inlet temperature held the same for each of the runs.

With the reduced heat release from an increase in REG, the pressure traces showed a later onset of knock and of lower intensity. The high sensitivity of pressure rise rate to REG% highlights the importance of correctly modelling the inlet conditions. This also agreed with the logic of using a comparison to PRFs as the metric of knock resistance, rather than simply the compression ratio, as the reference fuels would be subject to the same REG effects as the test fuel, thus improving the reproducibility of test results.

A similar logic was applied in this study to justify the use of the seemingly large REG fraction of 20%, to bring the peak pressures predicted by the model in line with experimental

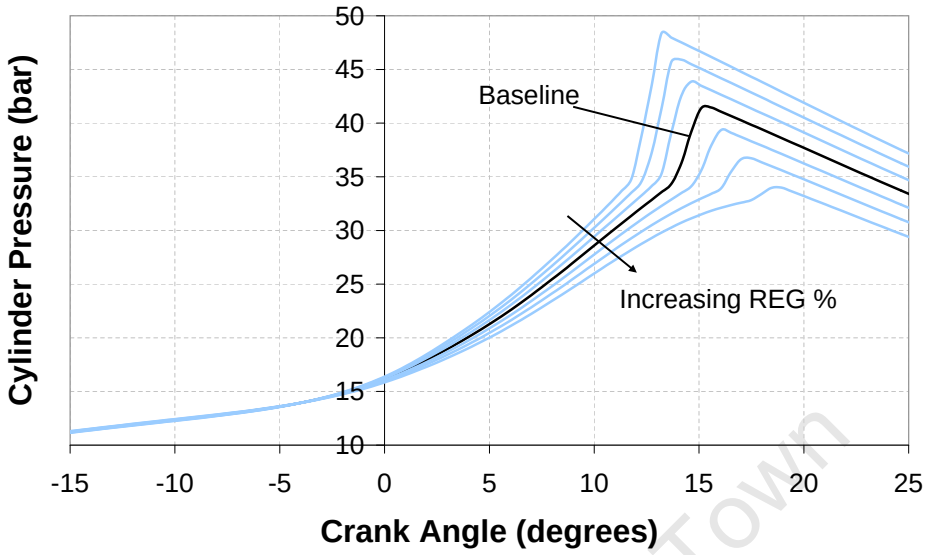

Figure 4.16: *Parametric Study: Effect of residual exhaust gas fraction on pressure trace. REG = 5% to 35% in increments of 5%*

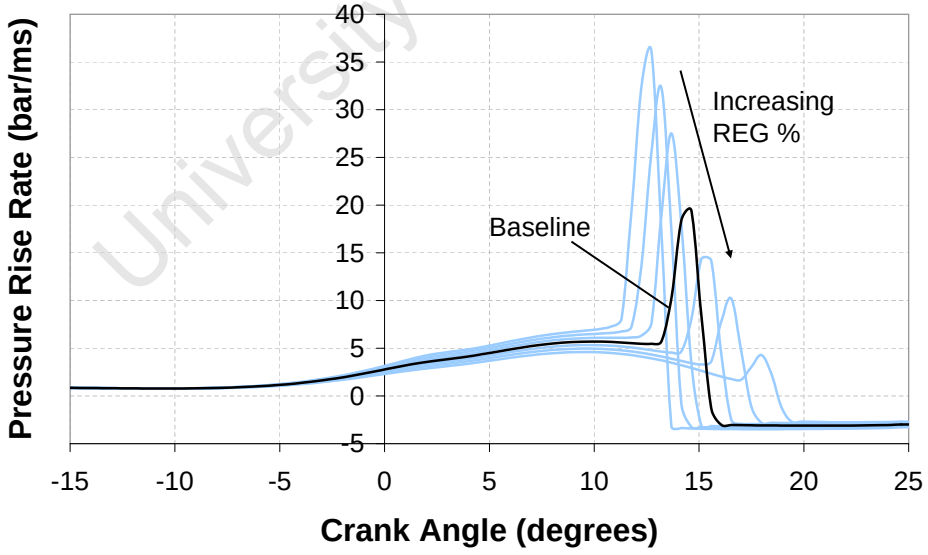

Figure 4.17: *Parametric Study: Effect of residual exhaust gas fraction on rate of change of pressure. REG = 5% to 35% in increments of 5%*

results. As all fuels run would be subject to these same conditions, it is the comparison of their responses which is of interest.

4.5.4 Inlet Pressure

Inlet Pressure was varied between 0.95 bar and 1.0 bar in increments of 0.01 bar. The model response to changes in inlet pressure was the least sensitive of all the variables tested. Figure 4.18 shows that the different pressure traces generated were barely discernible and the pressure rise rates in Figure 4.19 were likewise of very similar magnitude. This implies that the Octane test results are not influenced too greatly by small variations in the inlet pressure, which may be caused by differences in ambient conditions or modifications of the intake system.

Larger variations in atmospheric pressure such as that caused by change in altitude would have had a more appreciable effect, which is why slightly different test conditions are stipulated for larger differences in atmospheric pressure. However this would be more to bring the knockmeter readings in line with the expected values and should not influence the relative performance of different fuels greatly.

4.5.5 Inlet Bulk Temperature

The inlet bulk temperature at IVC was varied between 370 K and 450 K in increments of 10 K with the results shown in Figures 4.20 and 4.21 using 20 K increments for clarity. Given the uncertainty in measurement of the in-cylinder temperature, a broad range was investigated. The resultant pressure traces reached approximately the same peak pressure of 40 bar. Simulations with increased inlet temperature produced slightly lower pressures during normal combustion. This can be attributed to the fact that all simulations reached approximately the same peak temperature due to dissociation equilibrium reactions. Simulations with higher initial temperatures therefore experienced a lower total temperature rise due to combustion, resulting in a lower pressure at the same crank angle.

The onset of knock was predictably earlier for simulations with higher initial temperature, and therefore involved a larger fraction of the unburned gas. The pressure rise rate due to knock increased by between 5 and 10 bar/ms for an increase of 20 K in the initial temperature.

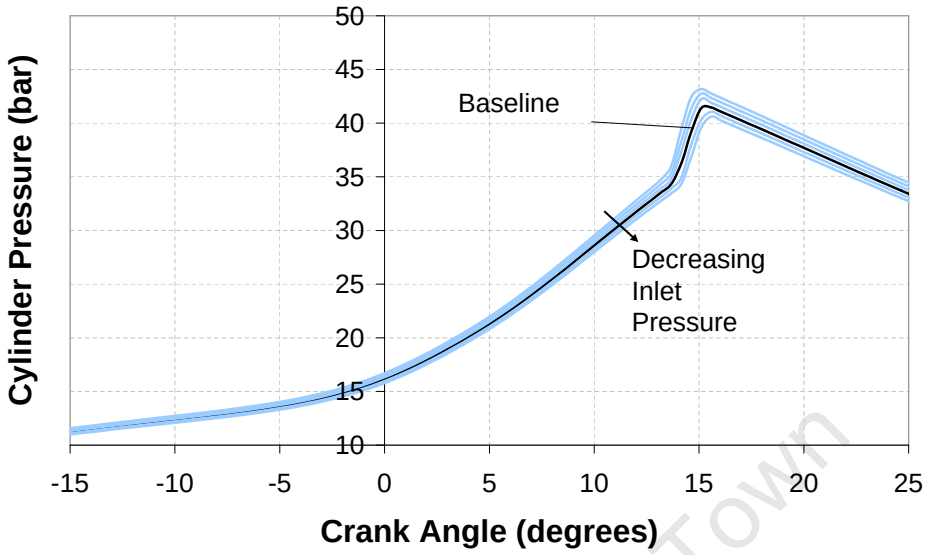

Figure 4.18: *Parametric Study: Effect of inlet pressure on pressure trace. P_{IVC} = 0.95 bar to 1.0 bar in increments of 0.01 bar*

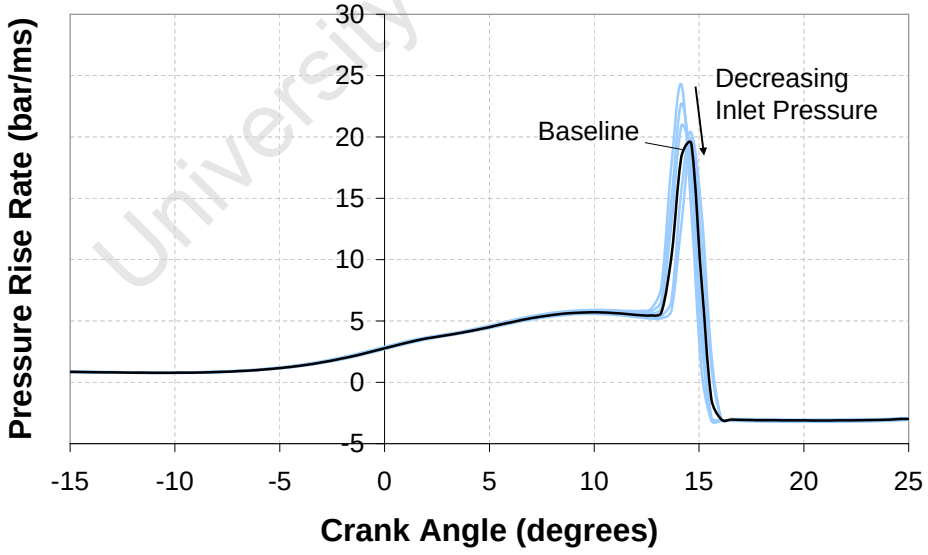

Figure 4.19: *Parametric Study: Effect of inlet pressure on rate of change of pressure. P_{IVC} = 0.95 bar to 1.0 bar in increments of 0.01 bar*

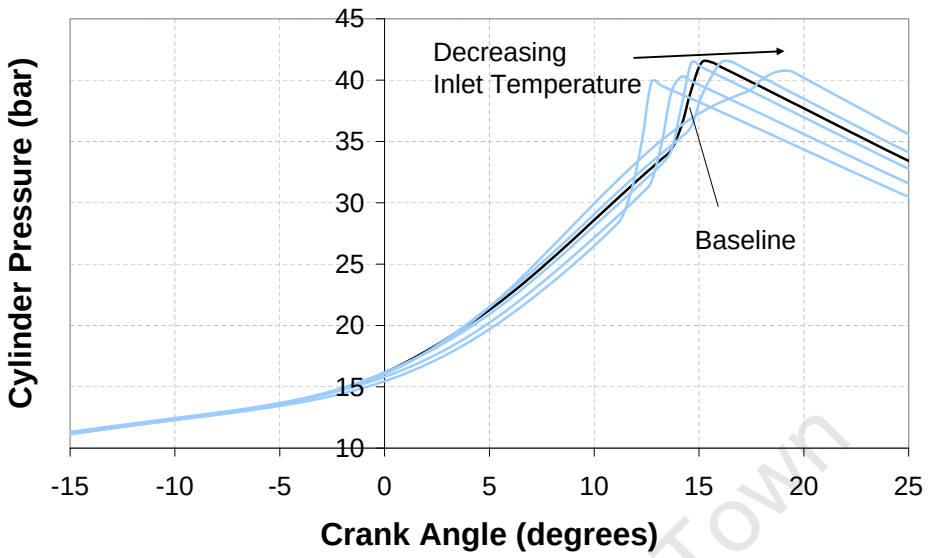

Figure 4.20: *Parametric Study: Effect of bulk inlet temperature on pressure trace. T_{IVC} = 370 K to 450 K in increments of 20 K*

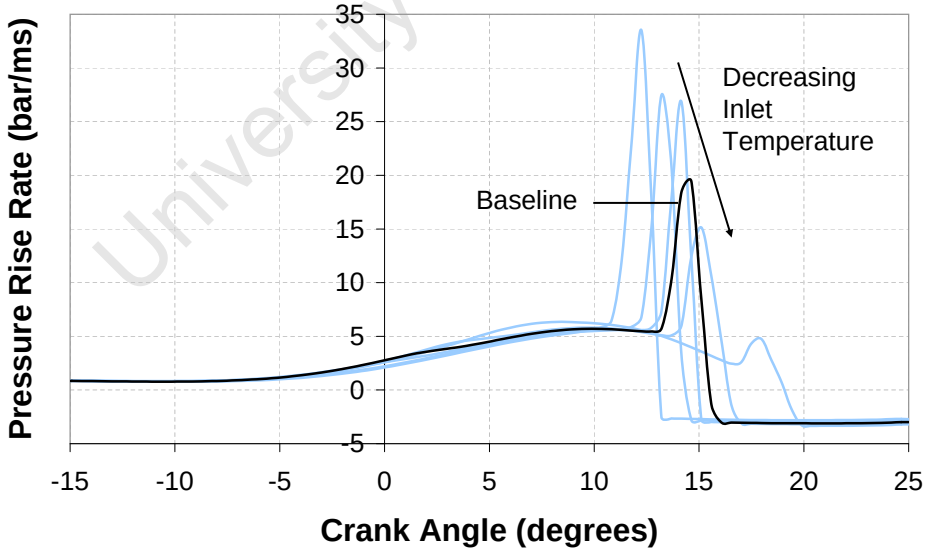

Figure 4.21: *Parametric Study: Effect of bulk inlet temperature on rate of change of pressure. T_{IVC} = 370 K to 450 K in increments of 20 K*

4.5.6 Inlet Temperature Profile

The in-cylinder temperature gradient was varied between 0 K and 40 K in increments of 10 K. In order to achieve this, the bulk temperature was kept constant and the minimum and maximum temperatures adjusted, applying the same temperature profile, so that the difference between T_{max} and T_{min} in the unburned zones at IVC would be the temperature gradient required. The results of these simulations are shown in Figures 4.22 and 4.23.

Decreasing the temperature gradient had the effect of delaying the knock point (since the zone with the highest initial temperature would have autoignited first and would have started off at a lower initial temperature than other simulations). The other expected result is that the slope of the pressure trace after the knock point steepened with decreased temperature gradient, since zones at closer initial temperatures would autoignite in quicker succession. Similar results were noted by Xu et al [56] in their multi-zone HCCI model.

For an initial temperature gradient of 20 K, it is interesting to note that at TDC, the difference between maximum gas temperature and minimum temperature in the unburned zones was 30 K and at 5 CAD before knock-point it was 40 K. The temperature gradient resulting in cascading autoignition can therefore be much greater than at initial conditions. For fuel-air mixtures with different autoignition delays, the temperature gradient at the point of autoignition would also therefore be different.

Assuming an in-cylinder temperature gradient does exist, it is uncertain what the shape of the temperature profile would be. Several options of axisymmetric profiles were considered, as shown in Figure 4.24. Profiles **a**, **b** and **c** assumed a higher initial temperature at the walls, reducing inwards in either a convex, linear or concave profile. Profiles **d**, **e** and **f** assumed a higher temperature at the centre, reducing toward the walls.

The shapes of each of the pressure developments after the knock point were all slightly different. However Figure 4.26 shows that the peak pressure rise rate was approximately the same for all the profiles except **a** and **b**. This may be explained by the fact that the annular initial distribution of the zones meant that the outer most zones inherently contained more mass than the zones near the center. Profiles **a** and **b** therefore contained more mass at higher temperature, which would have resulted in a higher rate of pressure rise when they autoignited. The knock point of profiles **e** and **f** were delayed slightly because the hottest zones that would have autoignited first were completely consumed by the flame front before the knock point.

Profile **c** was used for the rest of this study as it best matched the experimental pressure traces and this was consistent with the findings of [65]. However more detailed CFD modelling of the CFR in-cylinder flow and fuel evaporation would be required to verify this, as the very similar pressure traces of the different profiles may have produced quite different results when filtered to produce the knockmeter reading.

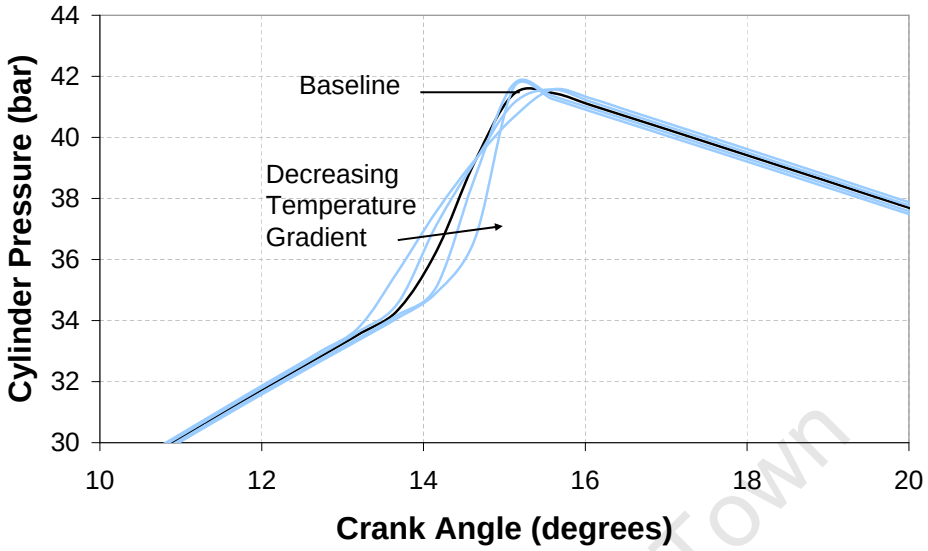

Figure 4.22: *Parametric Study: Effect of in-cylinder temperature gradient on pressure trace.* ΔT_{IVC} *= 0 K to 40 K in increments of 10 K*

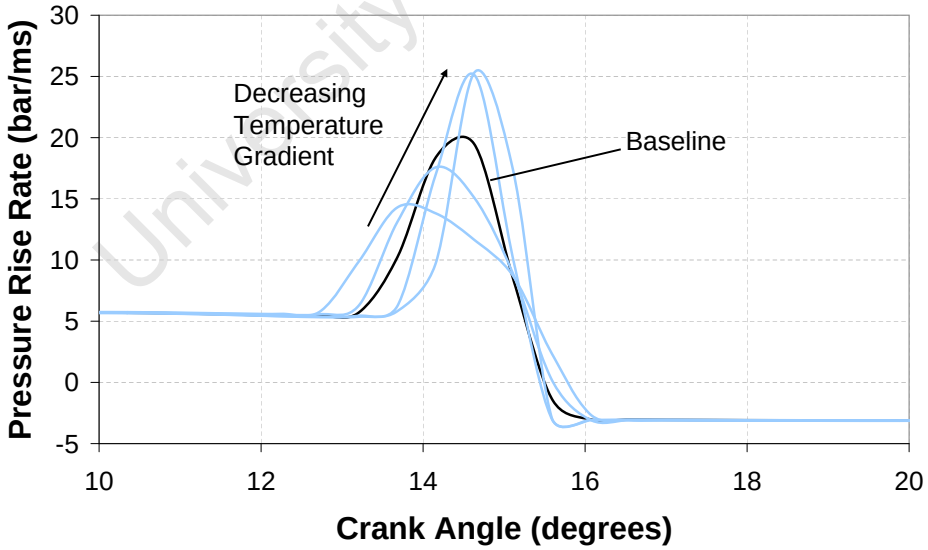

Figure 4.23: *Parametric Study: Effect of in-cylinder temperature gradient on rate of change of pressure.* ΔT_{IVC} *= 0 K to 40 K in increments of 10 K*

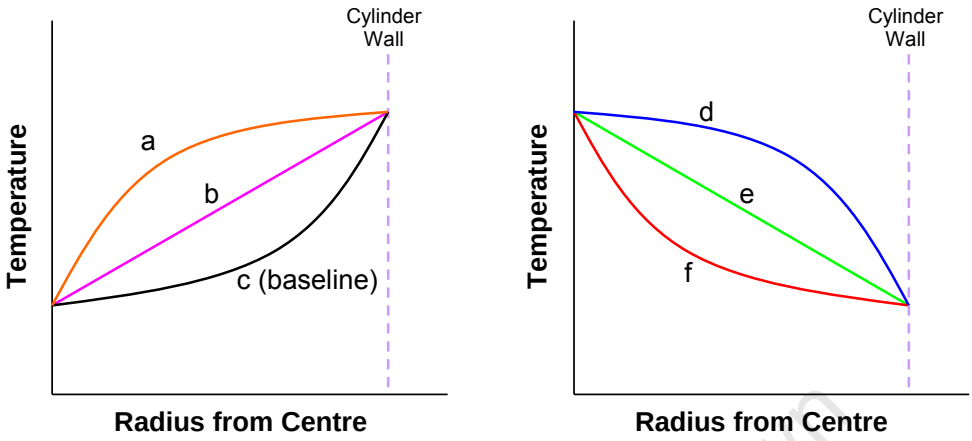

Figure 4.24: *Temperature profiles considered in the parametric study. Profiles* ***a****,* ***b*** *and* ***c*** *increase in temperature from the centre toward the cylinder wall. Profiles* ***d****,* ***e*** *and* ***f*** *decrease in temperature from the centre toward the cylinder wall.*

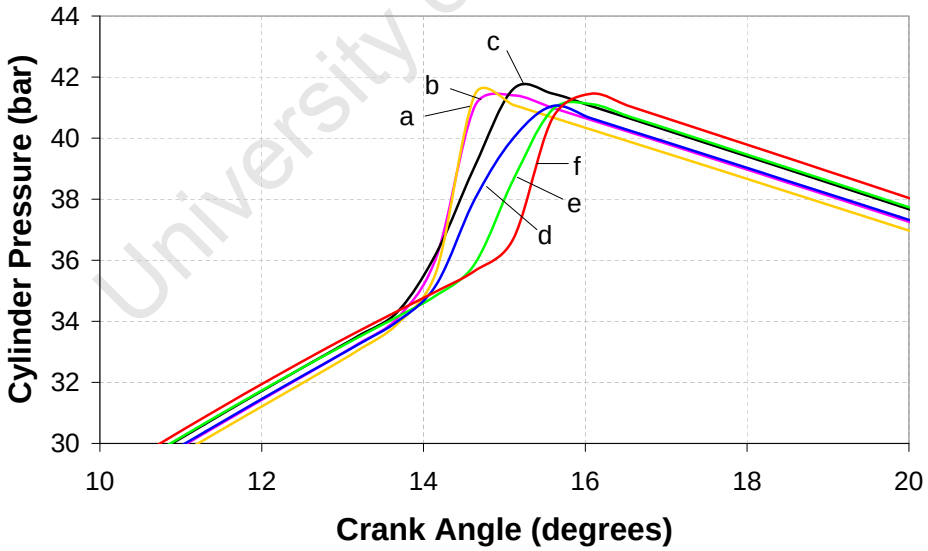

Figure 4.25: *Parametric Study: Effect of temperature gradient profile on pressure trace. Temperature profiles are as shown in Figure 4.24.*

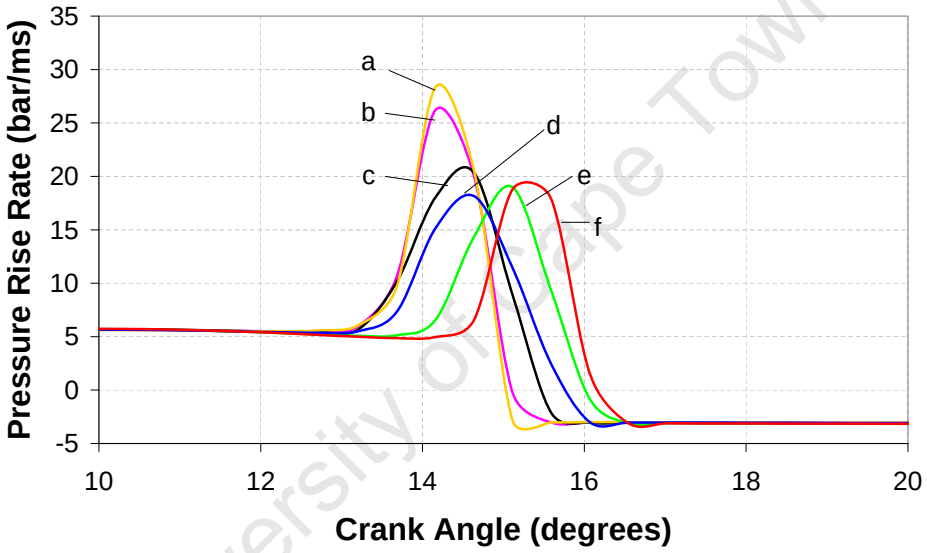

Figure 4.26: *Parametric Study: Effect of temperature gradient profile of rate of change of pressure. Temperature profiles are as shown in Figure 4.24.*

Chapter 5

Calibration of the Functional Global Autoignition Model

5.1 Calibration Methodology

The FGAM was calibrated to fit the autoignition profiles of the PRF and TSF blends considered in this study. These autoignition profiles were generated from a set of constant volume autoignition simulations performed using Chemkin^{TM} 4.1 [75] and the detailed kinetic mechanism developed at Lawrence Livermore National Laboratory (LLNL) [24].

For each fuel, 100 simulations were conducted at stoichiometric fuel-air ratio, REG fraction of 15%, temperatures spanning 600 K to 1200 K and pressures spanning 10 bar to 40 bar. It is known that, for example in the RON test, PRF blends produce maximum knock at fuel-air ratios just rich of stoichiometric. However, the FGAM had not been validated for rich mixtures, and as such, this modelling study was restricted to stoichiometric conditions.

The results of the DKM simulations were plotted as per Figure 2.2 to show the key autoignition features of overall ignition delay, cool flame ignition delay, cool flame ceiling temperature, and post cool flame ignition delay. Simulations under the same conditions were then performed using the FGAM as the reaction mechanism. The results of these FGAM simulations were overlaid on the DKM results and the two sets compared. This was first done for iso-octane (PRF100) as FGAM calibration coefficients were already available [39].

The FGAM coefficients were then manually adjusted to bring the autoignition behaviour of the FGAM results in line with the DKM results. Because of the interdependent and non-linear nature of the reacting system, it was not possible to a match a single behaviour characteristic to a single coefficient. As such, obtaining a good fit through simple manual adjustment was found to be very challenging.

An optimisation algorithm known as Particle Swarm Optimisation (PSO) was therefore applied to the system to obtain FGAM coefficients that provided the best fit. Details of this algorithm are contained in Appendix B but a brief summary is presented below.

5.1.1 Use of the PSO to solve for FGAM coefficients

The solution space is the multi-dimensional continuum of all possible values that each of the FGAM coefficients can take (each of the FGAM coefficients is a dimension). A *particle* can occupy one position in the solution space and so represent a possible solution with values of each of the coefficients. How good a solution this particle represents is measured by a *fitness function*. In this case the fitness function was the area between the respective temperature-time traces generated by the DKM and FGAM. The smaller the area, the better the agreement of the two mechanisms. This fitness function is given mathematically by:

$$err = \frac{\int_{t=0}^{ID} |T_{DKM} - T_{FGAM}| \, dt}{T_{AI} \times ID} \tag{5.1}$$

where
- err is the error in fit or fitness function
- t is time
- ID is the overall ignition delay (the maximum of that given by either the DKM and the FGAM is used).
- T_{DKM} is the instantaneous temperature calculated using the DKM.
- T_{FGAM} is the instantaneous temperature calculated using the FGAM.
- T_{AI} is the temperature above which autoignition is assumed to be complete. In this case T_{AI} was set to 1500K to provide balance between fitting overall ignition delay and cool flame behaviour.

The solution space is then randomly populated by a small, fixed number of particles (in this case 20). The collection of these particles is known as the *swarm*. Each particle "knows" the best position that it has previously occupied (*personal best*), as well as the best position previously occupied by any member of the swarm (*global best*). The particles are then allowed to move through the solution space, each drawn toward its personal best, the global best and given a random component. This process repeats until the swarm converges on a solution.

This approach was suited to solution of the FGAM coefficients for several reasons:

1. The multiple coefficients are solved for simultaneously.

2. As particles converge on a solution, they approach from multiple directions. In this way different combinations of coefficient adjustment are attempted, which is useful for a non-linear problem such as this one.

3. The slightly random nature of the particle movement ensures that the solution space is well explored, which decreases the likelihood of getting stuck in local minima as can be the case using traditional gradient based solvers.

The solutions obtained from the PSO solver were then compared once again to the DKM, to ensure that the AI behaviour was indeed adequately represented. An average error in fit (as measured by the fitness function) of between 6% and 15% was obtained for each of the fuels considered. The calibration coefficients, thus derived, are contained in Appendix A. As noted previously, the differences between Detailed Kinetic Models can be as much as 38% in overall ignition delay so an overall fit of less than 10% may be regarded as quite acceptable.

As an aside, the Functional Global Autoignition Model may be seen as functional both in Floweday's intended sense, that it describes the cool flame and autoignition behaviour of fuels adequately, but also in the fact that the model is itself a *functional* in the mathematical sense. A functional is a mapping from a vector space to its underlying scalar field. In this case the vector space is the solution space of possible FGAM calibration coefficients and each vector of coefficients is mapped onto the scalar value of the evaluated fitness function. The best fit is thus found by minimising the functional.

5.2 Calibration of PRF blends

5.2.1 PRF Autoignition Profiles

An example of the data points used to generate the autoignition profile for each of the fuels (in this case PRF80) is given in Figure 5.1. For clarity, only overall ignition delay is shown and not the other cool flame autoignition behaviour characteristics. The majority of the data points were chosen to describe the S-shape behaviour of the NTC region with additional points extending to the more linear high temperature and low temperature regions.

Although it is known that autoignition delay is more weakly dependent on pressure than on temperature, it can be seen that increasing the initial pressure from 10 bar to 40 bar, reduces the ignition delay by an order of magnitude in the NTC region. By contrast the effect of pressure in the low temperature region is significantly less noticeable. This lack of pressure response in cool flame ignition delay was one of the behavioural aspects specifically targeted in Floweday's formulation of the FGAM [39], however there does appear to be a slightly more noticeable effect in the 10 bar initial pressure simulations than in the 20 - 40 bar simulations. This can also be seen in Figure 5.2, where there is also a difference in the cool flame ignition delay for different initial pressures, even at temperatures below the onset of the cool flame hook.

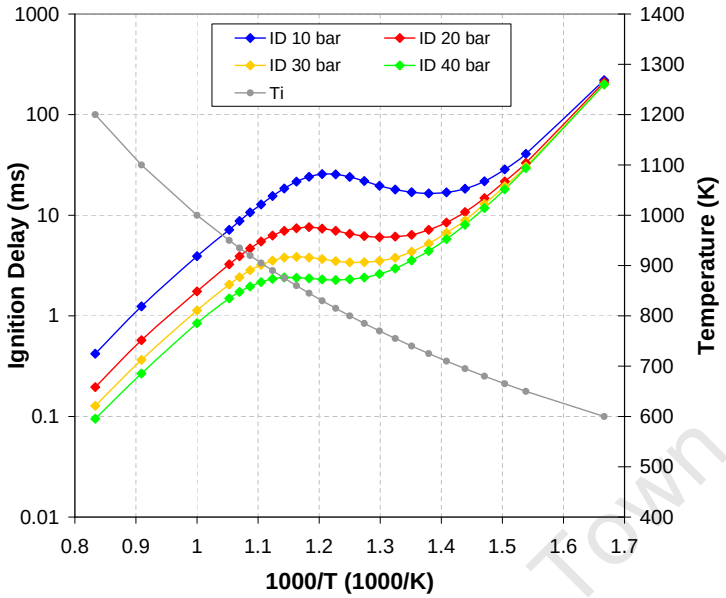

Figure 5.1: *Autoignition profile of PRF80 at varying initial temperatures and initial pressures: $\phi = 1$, REG% = 15%*

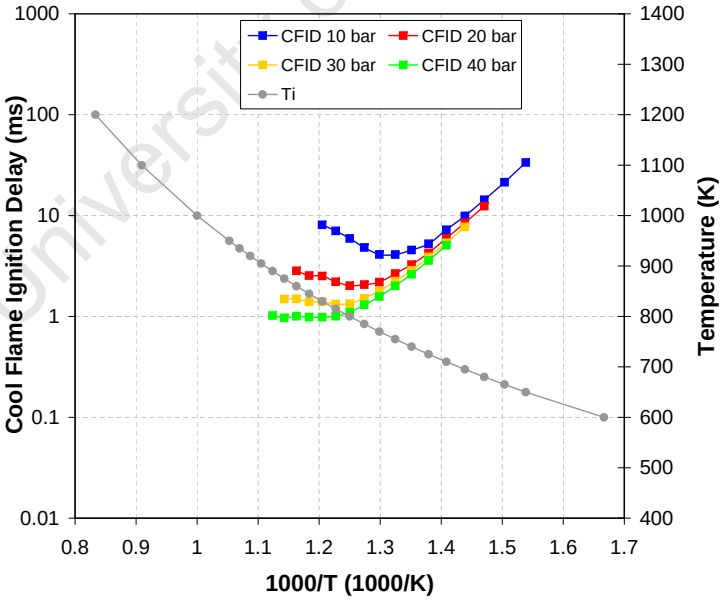

Figure 5.2: *Cool flame ignition delay of PRF80 at varying initial temperatures and initial pressures: $\phi = 1$, REG% = 15%*

Given the changing temperature-pressure environment of the engine, accurate response of ignition delay to pressure is imperative in a model simulating the Octane rating tests. Further development of the FGAM should therefore consider a reassessment of the ignition delay response to pressure at low temperatures.

Autoignition delay profiles of the PRF blends considered are shown for initial pressures of 20 bar in Figure 5.3. All PRFs showed very similar autoignition delays at high temperature, however the profiles diverge rapidly from about 900 K as temperatures decrease into the transition NTC region. It can be seen that at approximately 800 K, the local maximum ID for PRF100 in the NTC region, corresponds with the local minimum ID for PRF40. From this point, the profiles converge once again until about 700 K, where ignition delay is effectively linear with constant offset between the different PRF ID profiles. It should be noted that although these ID values appear quite similar due to the log scale used, the difference between them is actually quite large.

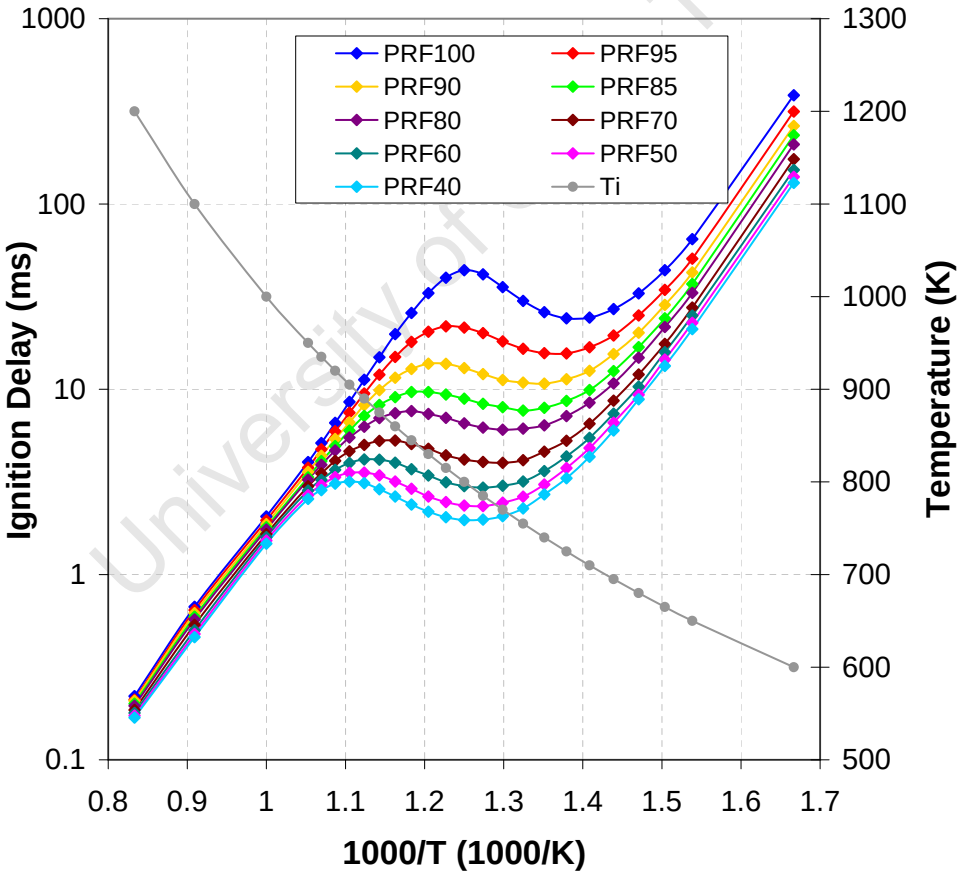

Figure 5.3: *Comparison of autoignition profiles of PRF blends: $P = 20$ bar, $\phi = 1$, REG% = 15%*

5.2.2 Evaluation of PRF fits obtained

The fit to overall ignition delay, obtained for PRF80, is shown in Figure 5.4. Qualitatively, the ID profile generated by the FGAM is very similar to that of the DKM for all pressures considered. Fits to other PRF blends were similarly good.

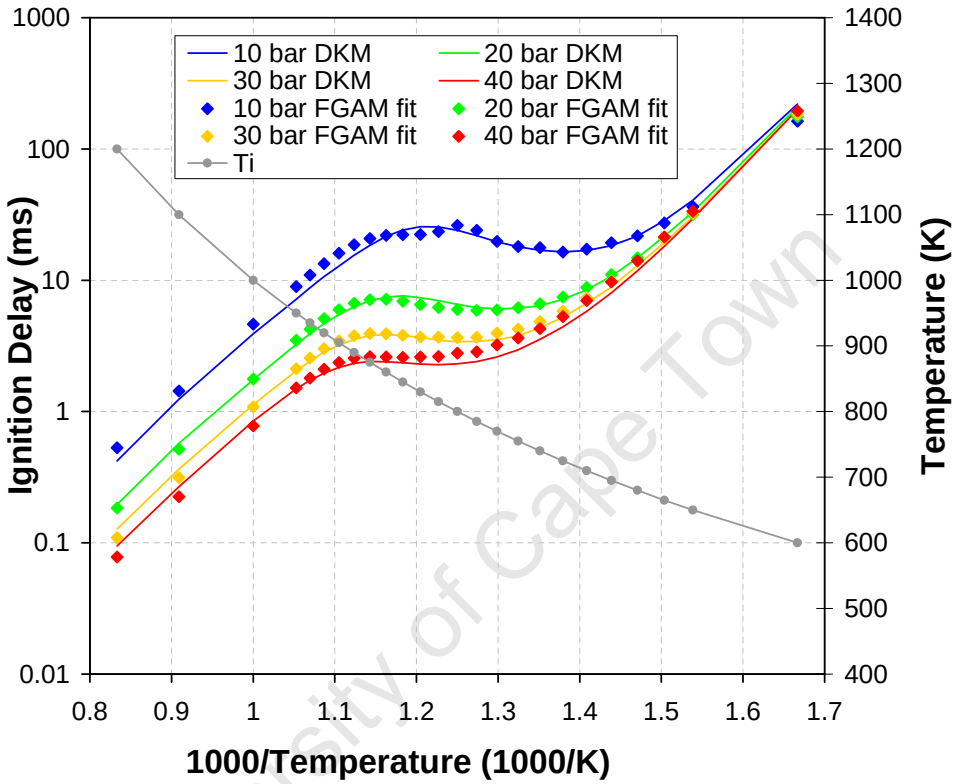

Figure 5.4: *Overall ignition delay fit of the FGAM to DKM simulations for PRF80 blend: ϕ = 1, REG% = 15%*

In order to demonstrate that the cool flame behaviour was also well described by the FGAM, selected temperature-time traces for individual constant volume simulations, at 30 bar and various initial temperature, are shown in Figure 5.5. This fit of the FGAM showed a slight under-prediction of the cool flame ignition delay and ceiling temperature and a slight over-prediction in post-cool flame ignition delay. However the overall trends for these parameters were directionally consistent.

Once the calibration coefficients for the PRFs considered were found, consideration was given to whether a best fit function could be assigned to each of the coefficients, in order to interpolate for PRF blends in between. As an example, the pre-exponential A coefficients obtained for each of the PRFs are shown in Figure 5.6.

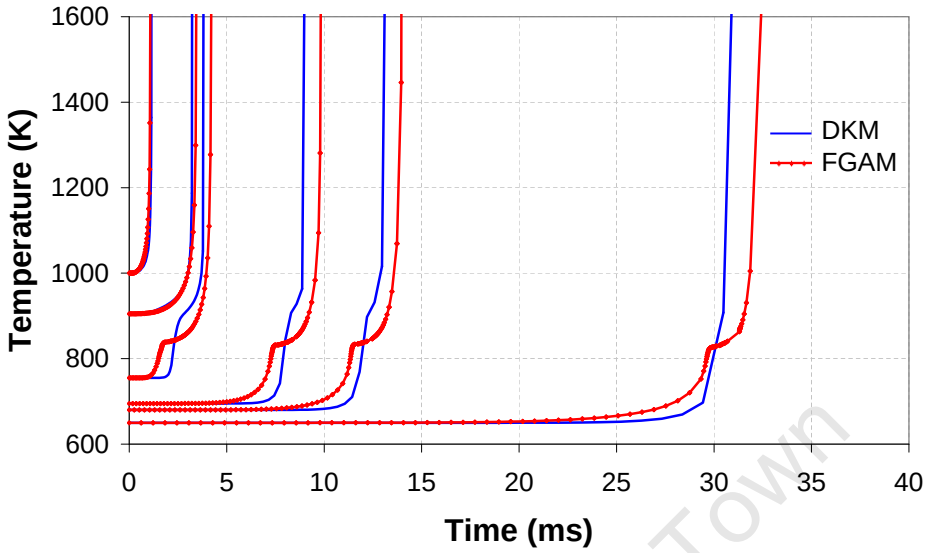

Figure 5.5: *Examples of temperature vs time traces for PRF80 at $P = 30bar$, $\phi = 1$, $REG\% = 15\%$ and various initial temperatures showing FGAM fit to DKM simulations of overall ignition delay and cool flame behaviour*

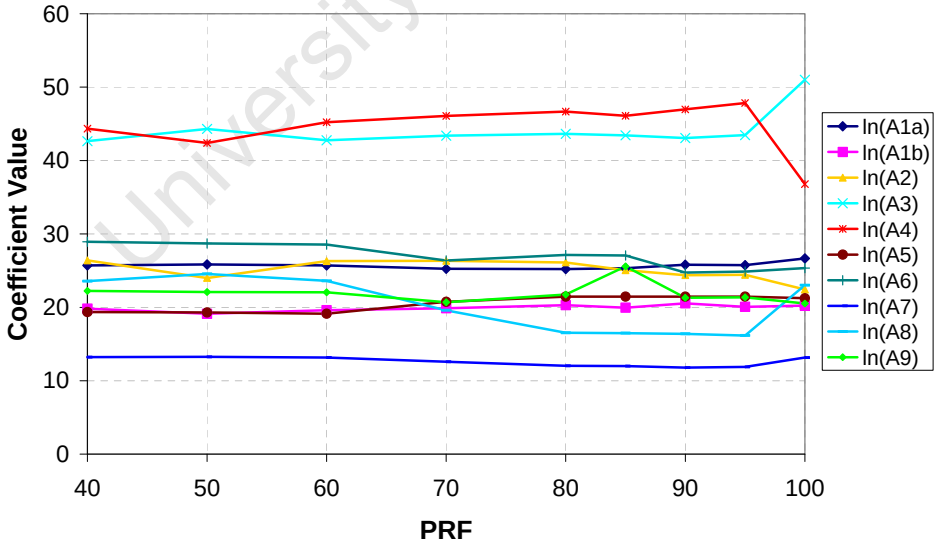

Figure 5.6: *FGAM A calibration coefficients obtained for PRFs*

Although at first glance these values may appear to be following some form of trend, normalising each of the coefficients to its average value paints a different picture in Figure 5.7. It can be seen that most of the variation in each of the coefficients is within 10% and the changes in value are quite erratic, with no clear increasing, decreasing or constant trends. No interpolating functions could thus be found. This highlights the extremely non-linear behaviour that required the use of an algorithm such as PSO to optimise for the best fit.

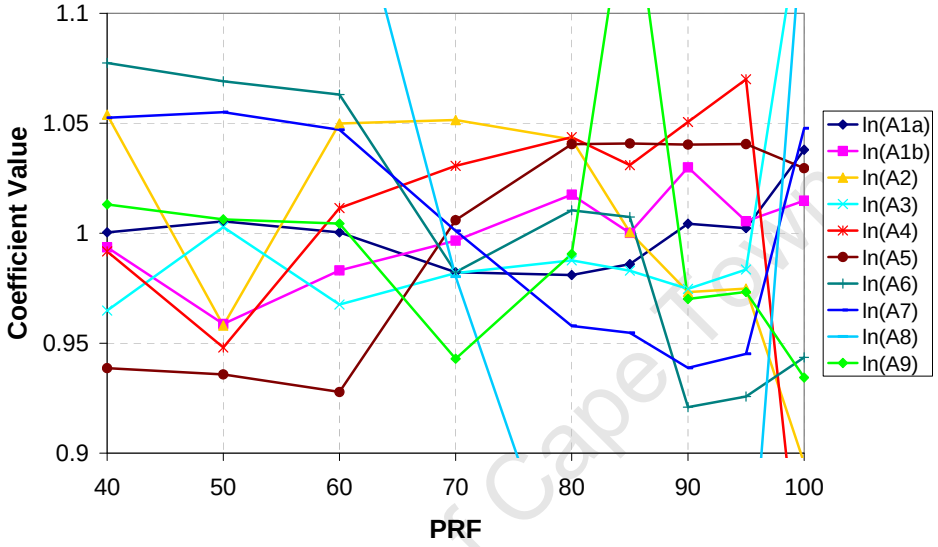

Figure 5.7: *FGAM A calibration coefficients obtained for PRFs normalised to the average value of each coefficient*

5.3 Calibration of TSF blends

5.3.1 TSF Autoignition Profiles

Two Toluene Standardisation Fuel blends were considered in this study. Designated TSF998 and TSF892, their composition and Octane Numbers are given in Table 5.1. The autoignition behaviour of these blends was significantly different to that of the PRF blends. A comparison with the PRF blends corresponding to the nearest RON and MON values of the TSFs, at initial pressures of 20 bar, is given in Figure 5.8.

At high temperature, ignition delay of the TSFs was seen to be significantly higher than for the PRF blends. This is due to the autoignition behaviour of toluene dominating in this region. The NTC region of the TSF manifests simply in an inflection point in the slope of the ignition delay curve as opposed to an actual increase in ignition delay with increasing temperature as seen with the PRFs. The ignition delay of TSF892 was in fact

Table 5.1: *Description of TSF fuels considered in the autoignition modelling study*

Designation	RON	MON	%iso-octane	%n-heptane	%toluene
TSF998	99.8	88.7	10%	16%	74%
TSF892	89.2	78.2	0%	30%	70%

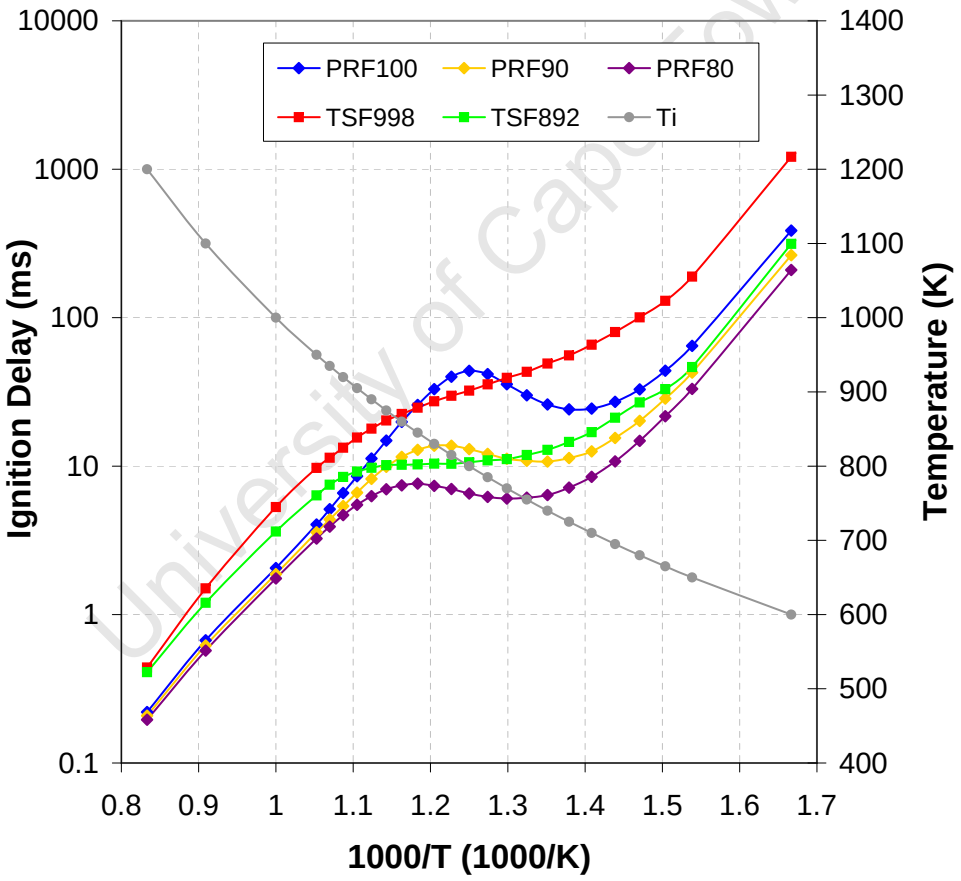

Figure 5.8: *Comparison of TSF autoignition profiles with PRF blends of similar Octane number: $P = 20$ bar, $\phi = 1$, REG% = 15%*

almost constant for temperatures between 750 K and 900 K. Because of this differing NTC behaviour, there is in fact overlap between the autoignition profiles of TSF998 and PRF100 as well as TSF892 and PRF90. The ignition delay times for TSF892 are fairly similar to PRF90 in the low and intermediate temperature region, however TSF998 has significantly longer ignition delay times than PRF100 at low temperature.

5.3.2 Evaluation of TSF fits obtained

The overall ignition delay fit obtained for both TSF998 and TSF892 were fairly reasonable, with average errors in fit of 12% for each. The fit obtained for TSF998 is shown in Figure 5.9. A slight deviation can be noted in the 10 bar simulations and in the fact that the FGAM fit shows a more pronounced NTC region than is manifested in the DKM simulations.

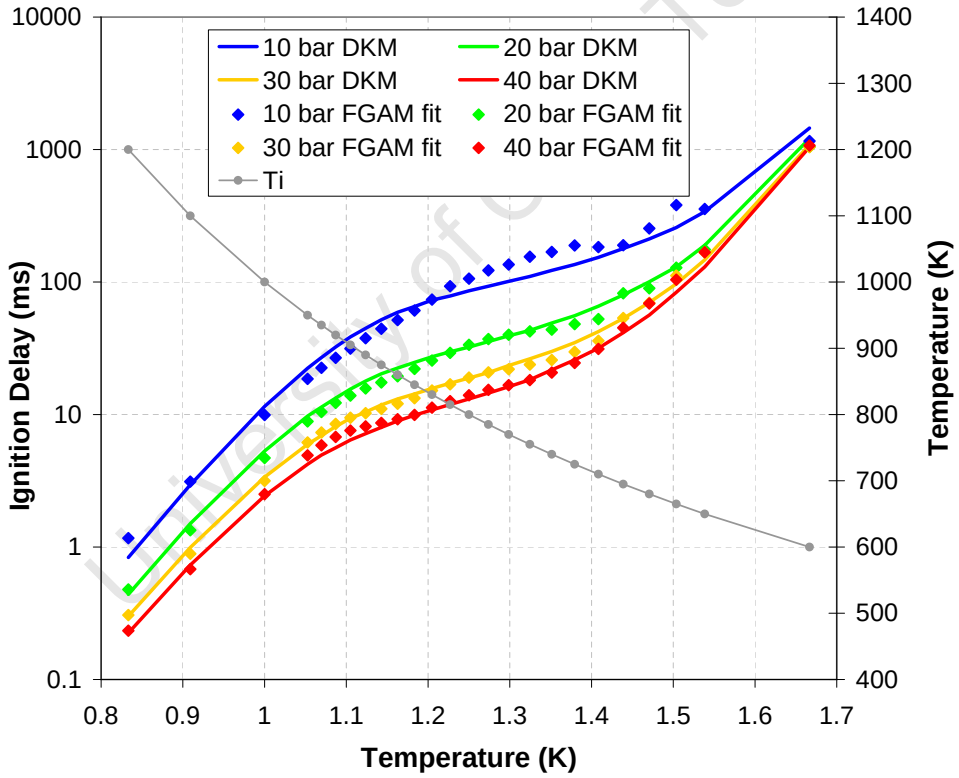

Figure 5.9: *Overall ignition delay fit of the FGAM to DKM simulations for TSF998 blend: ϕ = 1, REG% = 15%*

An interesting feature of the autoignition behaviour of the TSF blends is the manifestation of the cool flame. Recall that for PRFs the cool flame is generally identifiable as a distinct event with a fairly steep temperature increase after the cool flame ignition delay, plateauing

off at a cool flame ceiling temperature with little heat release until the final autoignition delay. By contrast many of the TSF simulations display a more "smeared out" cool flame as shown in Figure 5.10.

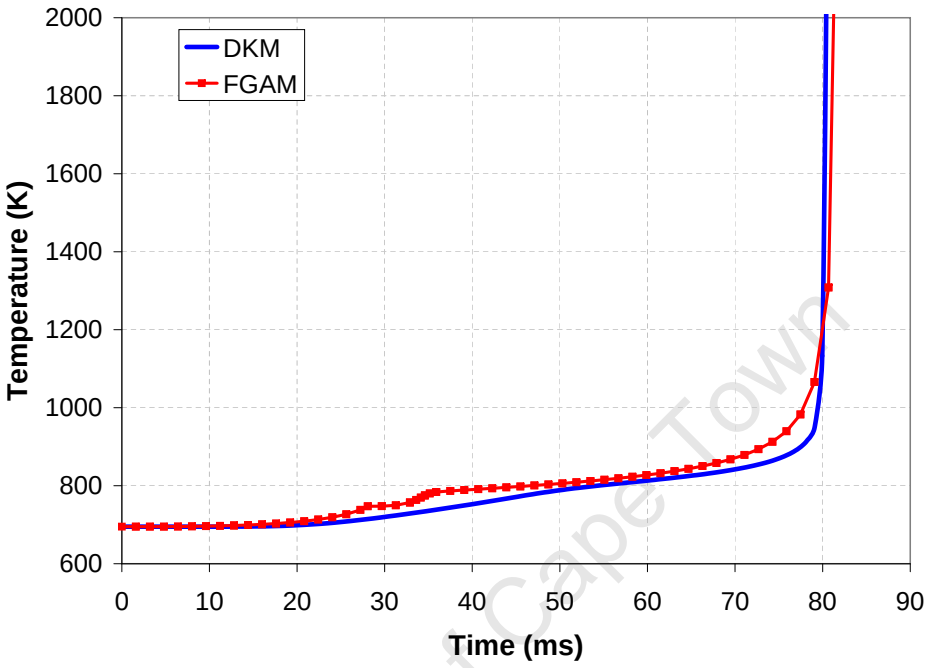

Figure 5.10: *Temperature-time traces of TSF998 at initial temperature of 695 K and initial pressure of 20 bar, showing fit of FGAM to DKM simulation*

At about 25 ms, the cool flame begins with gradual heat release until about 50 ms, where the rate of heat release decreases slightly. There is still a gradual heat release until final ignition delay at 80 ms. The change in gradient at 50 ms suggests that it is fact a cool flame heat release at 25 ms and not simply a gradual heat release through the high temperature reaction pathway only. The FGAM was able to simulate this behaviour but only through multiple changes in gradient during the initial heat release. This was accomplished through "misuse" of the two reverse reactions ($F \rightleftharpoons J$ and $I \rightleftharpoons Q$) instead of their intended function of controlling the *cool flame hook* and *cool flame kill* behaviour [39]. This in turn resulted in the slight irregular behaviour in the overall ignition delay profiles. This may simply be a result of the particular FGAM fit used and it may be possible for the FGAM to accurately simulate this gradual heat release behaviour with a different combination of calibration coefficients.

Part of the reason for the differing behaviour of the TSFs to the PRFs is that the TSFs consist of a blend of a single-stage fuel (toluene) and two-stage fuels (iso-octane and n-heptane). The interaction between these components is complex, especially between toluene and iso-octane, with Vanhove et al [18] noting that the addition of toluene to

iso-octane actually *increased* the reactivity above 830 K. Expanding on this, Andrae [25] noted the antagonistic MON blending behaviour of iso-octane and toluene. Iso-octane has a MON of 100 and toluene has a MON of approximately 106. However 50%/50% and 75%/25% blends of iso-octane in toluene had MON values *less* than 100.

Furthermore, the inclusion of toluene in the DKM of [24] was based on the PRF/toluene mechanism proposed by Sakai et al [28] where it is specifically stated that "*the acceleration by the addition of toluene to iso-octane is not fully reproduced*". Additionally it is claimed that the mechanism had been validated over temperatures spanning 500 K to 1700 K and pressures spanning 2 atm to 50 atm, however no validation of the PRF/toluene interaction below 900 K is actually shown. Battin-Leclerc [29] in his review of fuel surrogates notes that "*several models are now available for the oxidation of PRF/toluene mixtures but they suffer from the uncertainties in the mechanism of the oxidation of toluene at low temperature and high pressure*". Vanhove et al [18] also note that the blending behaviour of toluene with iso-octane changes dramatically for blends containing more than about 60% toluene. The results presented in [28] were for a blend containing only 20% toluene.

Although the above analysis does not necessarily mean that the DKM results for the toluene containing blends are wrong, they should be treated with caution. In later application of the FGAM in the multi-zone model, the simulation results for TSF998 showed poor agreement with experimental results, even though the FGAM fit to the DKM autoignition profile was reasonable. For this reason, the results in the remainder of this thesis focus on the simulations of PRF blends and the TSF892 blend that does not contain any iso-octane. An alternate explanation, which cannot be discounted, is of course simply that either the initial conditions or the multi-zone model simulations themselves are incorrect. The good results obtained for the PRF blends would however suggest otherwise.

Chapter 6

Simulation of Octane Number Tests

The FGAM was calibrated for PRF blends between PRF40 and PRF100 and the coefficients obtained are provided in Appendix A. The ASTM standards [2,3] list the compression ratios corresponding to SKI for the PRF blends and these are resultantly the critical compression ratios for their respective Octane Numbers. A Toluene Standardization Fuel designated TSF892 comprising 70% Toluene and 30% n-heptane was also fitted with the FGAM. This TSF has a RON of 89.2 and MON of 78.2. The fitted blends were run in the multi-zone model under RON test conditions at their critical compression ratios with simulation parameters as per Table 4.3.

6.1 RON Simulations

The pressure traces generated from the PRF blends running under their critical compression ratios for RON are shown in Figure 6.1. Note that the model had been calibrated on the PRF100 blend only and so the RON test simulations for other fuels were therefore purely predictive. These results showed good agreement with the experimental data of PRF blends run under these conditions [73]. The results for TSF892 simulated under RON90 conditions are also displayed. This showed a knock response similar to the PRF90 though slightly lower.

The mass fraction burned at knock point for the multi-zone model simulations were very consistent with the experimental results of the RON tests for PRF blends as seen in Figure 6.2. Generally a decrease in ON from RON100 resulted in a lower MFB at the knock point, and resultantly a higher mass fraction involved in the knock event. The increase in MFB for the RON50 test and subsequent decrease for RON40 was unexpected but confirmed by the experimental results. It is unclear why this deviation from the trend exists but it had been previously noted in [51]. The MFB for the TSF892 simulation is also shown. Although this value was lower than for the equivalent PRF, the difference was within the spread of the cycle-to-cycle variation of the experimental data. It should not however be

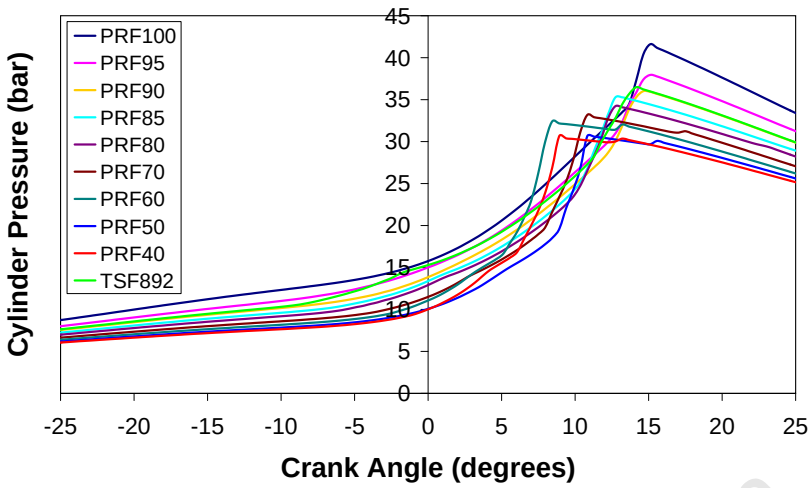

Figure 6.1: *Pressure traces of PRF blends and TSF892 running at their respective RON test conditions*

assumed that the mass fraction burned at knock point would be the same for all fuels.

The peak pressure rise rates for model simulations are shown in Figure 6.3. As with the experimental results, a decrease in Octane number resulted in an increase in peak pressure rise rate up till about RON60. The deviation to slightly reduced pressure rise rates for RON40 and RON50 were also simulated. Comparison of the magnitudes of pressure rise rates from simulation and experiment should be done with caution, as the experimental traces were first smoothed before analysis and this had the effect of reducing derivative values from the original noisy signal. However, the trends observed in change of peak pressure rise rate with Octane Number were consistent. The simulated pressure rise rate for TSF892 was however noticeably lower than for PRF90.

The one anomalous simulation point was ironically for the calibration point of RON100. It is uncertain why the peak pressure rise rate at this point was significantly higher than expected from the trend of the previous points. However two observations are worth mentioning. Firstly the experimental results show the RON100 peak pressure rise rate did not decrease from that of RON97, as would be expected from the trend, so at least some deviation should be expected from the simulation. Additionally the autoignition response of pure iso-octane is significantly different from that of blends with even small amounts of n-heptane. In Floweday's original calibration of the FGAM [39], it was noted that as good a fit for n-heptane was not obtained for iso-octane. It is therefore possible that the autoignition heat release rate predicted by the FGAM for PRF100 was too high, resulting in an over-prediction of the knock pressure rise rate. Further discussion on possible reasons for this deviation is presented in the next chapter.

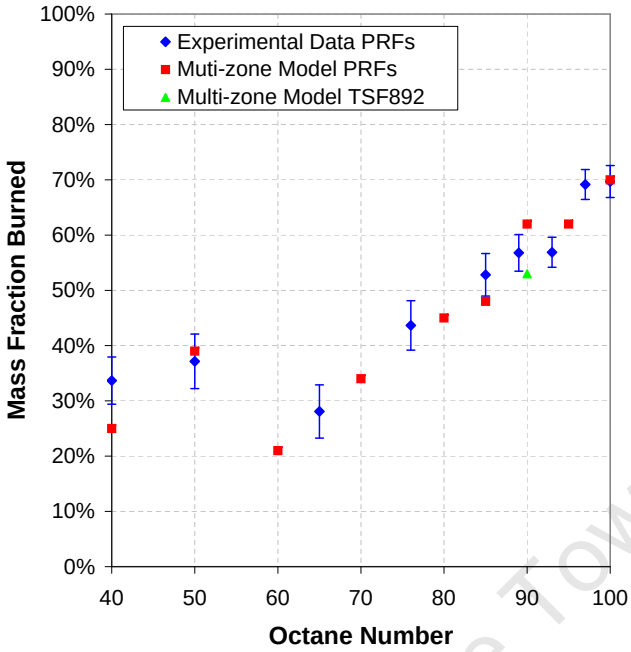

Figure 6.2: *Mass fraction burned at knock point for RON simulations compared with experimental results of [73]*

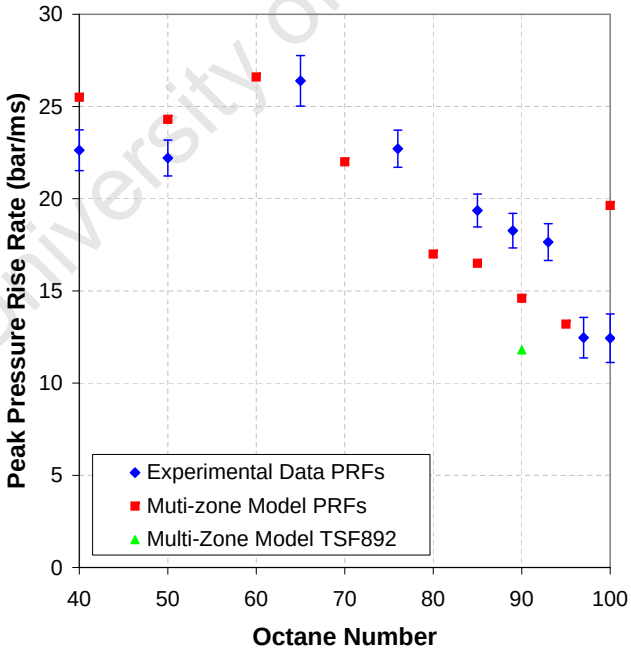

Figure 6.3: *Peak pressure rise rates for RON simulations compared with experimental results of [73]*

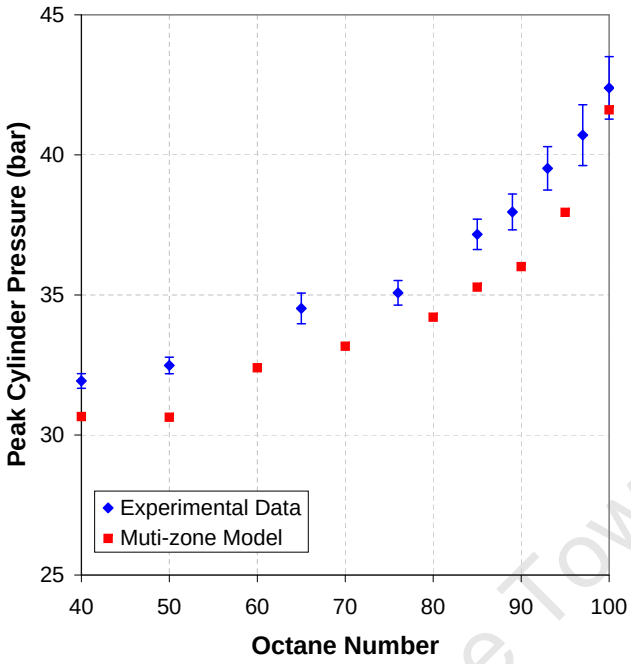

Figure 6.4: *Peak pressure values for RON simulations compared with experimental results of [73]*

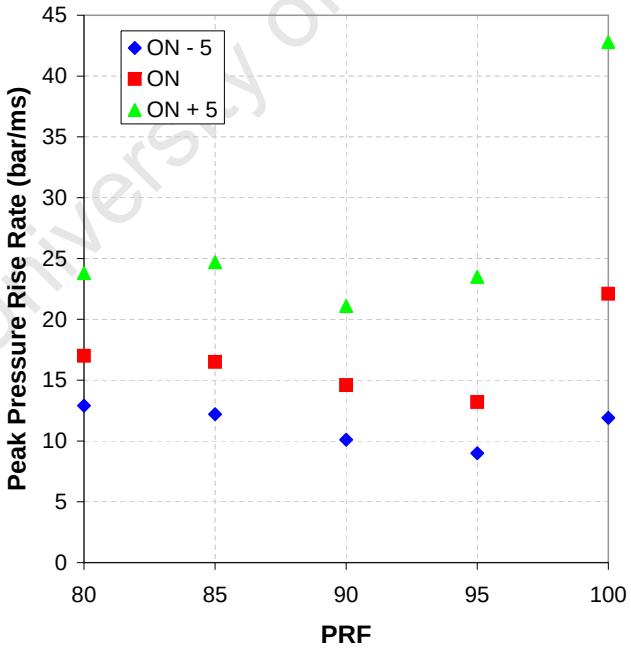

Figure 6.5: *Peak cylinder pressure rise rates for PRFs at Critical Compression Ratio (CCR) and at CCR corresponding to PRFs 5 ON above and 5 ON below*

The peak pressure values predicted by the multi-zone model at SKI (shown in Figure 6.4) were all slightly lower than obtained from the experimental data, with the exception of the PRF100 simulation, which lay within the 1 standard deviation distribution band. The increasing peak pressure with increasing ON trend was however well replicated. As the PRF100 test was used as the calibration point and, as noted above, this point produced a pressure rise rate that deviated from the trend observed in lower ON simulations, it is possible that a different calibration test point would have resulted in the overall simulation results matching the experimental data much more closely. The agreement that was achieved was nevertheless considered to be very good.

The PRF blends between RON80 and RON 100 were then run at compression ratios corresponding to 5 ON above and below their own. A comparison of the results is given in Figure 6.5. The pressure rise rates associated with the standard knock intensity were quite distinct from the higher and lower compression ratios run. Noting that the experimental cycle-to-cycle variation in peak pressure rise rate was generally in the region of 2 bar/ms, the model was therefore seen to differentiate between the RON of PRF blends above 80 within 5 ON.

6.2 MON Simulations

Following the good results obtained in simulation of the RON tests, the multi-zone model was then applied to simulation of the MON tests. Recall that the primary differences for the MON tests are the faster engine speed, controlled mixture temperature at 149°C and adjusted spark timing for changing ON. It was initially assumed then, that the major changes in the initial condition and simulation parameters would be engine speed, inlet temperature, ignition timing and burn duration.

These adjustments were made so as to best match the SKI pressure trace of the MON100 test. Once the model had been recalibrated for MON, the same fuels tested in the RON simulations were run under their respective MON test conditions. These results were compared to experimental data of the actual MON tests run for PRF fuels as shown in Figures 6.6-6.8.

It is immediately apparent that the results obtained for the MON simulations did not correspond as well with the experimental results as did the RON simulations. The peak knocking pressures of the simulations were significantly higher than those in experiments. The peak pressure rise rates did not show good correlation with experimental results in either magnitude or trend. Although the mass fraction burned at knock point in the simulations are in a reasonably consistent range for MON70 to MON100, the trends observed are not consistent and the results for lower ON are significantly different.

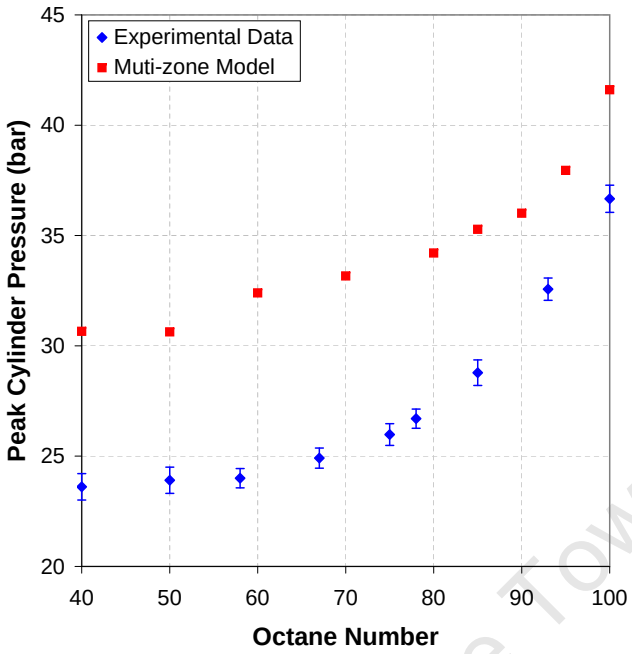

Figure 6.6: *Peak cylinder pressure values for MON simulations compared with experimental results of [73]*

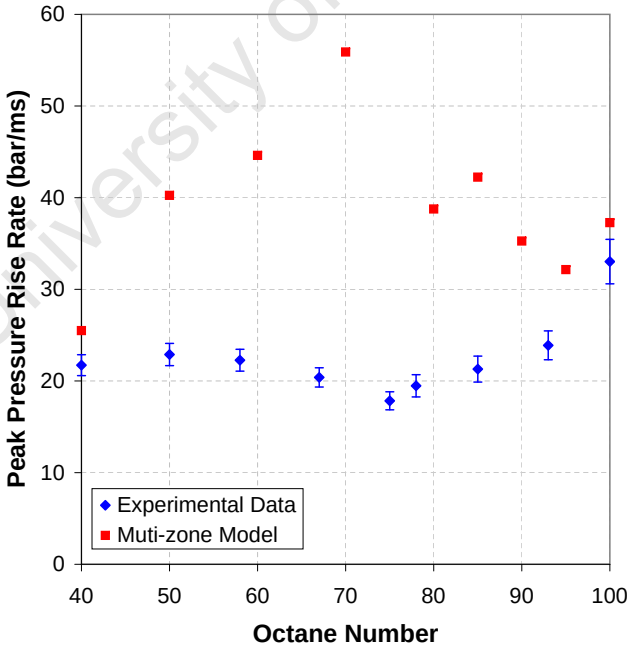

Figure 6.7: *Peak pressure rise rates for MON simulations compared with experimental data of [73]*

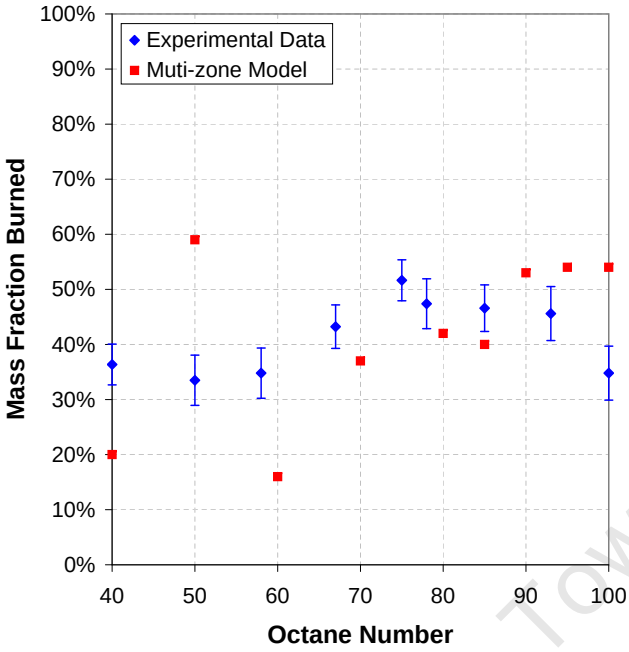

Figure 6.8: *Mass fraction burned at knock point for MON simulations compared with experimental data of [73]*

The poor agreement for the MON tests may be as a result of using the MON100 test as a calibration point, due to the deviant behaviour observed in the RON simulations. It may even be the case that the multi-zone model, or one of its submodels, is unable to simulate the MON test accurately. However it is considered more likely that the assumption of similar inlet conditions to the RON test, requiring only minor adjustments, was false. A more thorough study of the MON inlet conditions and independent calibration to fit a characteristic MON pressure trace (as was performed for the RON tests) would enable better simulation of MON test results.

Chapter 7

Discussion

This chapter deals with some of the issues and results encountered in this study in further detail. The results of the RON100 simulation, which deviated from the trend observed from other RON simulations, are first analysed to attempt to explain this behaviour. Then the Functional Global Autoignition Model that was used as the autoignition descriptor in the multi-zone engine model is discussed, highlighting its benefits and shortcomings in a study such as this, as well as identifying possible areas for future development of the FGAM. Finally the performance of the multi-zone engine model itself is discussed, in particular the potential to use it as a virtual CFR engine in order predict the Octane Number of an unknown fuel.

7.1 Anomalous Behaviour of the RON100 Simulation

Although the multi-zone engine model was calibrated to simulate the results of the RON100 test running on PRF100 fuel, the results of this particular simulation produced a higher peak pressure and peak pressure rise rate than either exhibited by the experimental results or predicted by the trend of simulations of lower ON tests. These results were displayed previously in Figures 6.3 and 6.4. Whereas the rest of the RON simulations matched the experimental data quite well, this single data point remained unsatisfactorily represented.

The data from all the RON simulations were therefore re-analysed from a different perspective. Figure 7.1 shows the gas properties of zone 19 (the first zone to autoignite in all the simulations) plotted in the Temperature-Pressure domain for each of the RON simulations as well as a RON100 simulation with autoignition chemistry disabled to produce a non-knocking trace. Given the adiabatic and closed zone assumption, and the fact that the initial temperature and pressure conditions were identical for all simulations, all of the temperature-pressure curves were coincident with the adiabatic compression curve up until the onset of autoignition heat release.

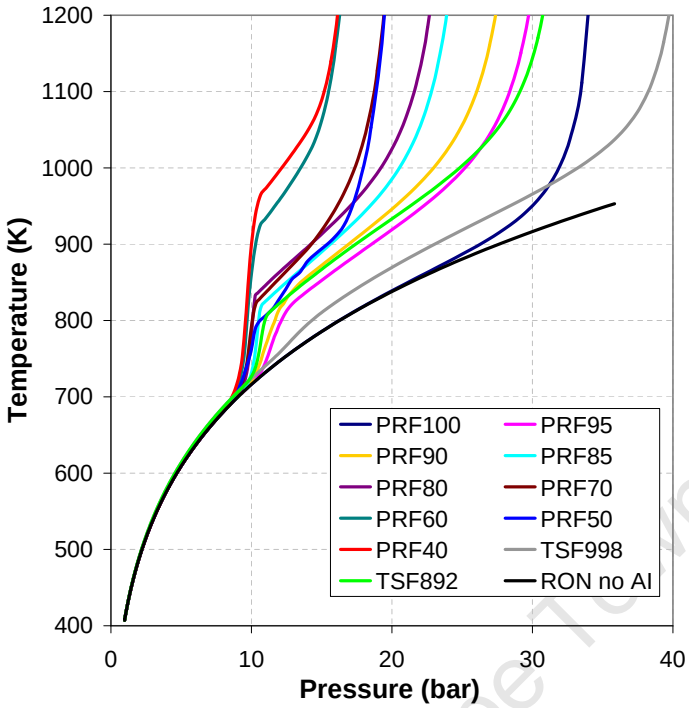

Figure 7.1: *Temperature-pressure histories from multi-zone model simulations in the first zone to autoignite for PRF and TSF blends at SKI*

It was noted that all the curves experienced a departure from this adiabatic compression curve in the region of 700 - 750 K and 10 bar, indicating a cool flame heat release, except for the PRF100 curve. Also notable is the more subdued response of the TSF998 curve, indicative of the "smeared out" cool flame heat release behaviour discussed in Section 5.3.2. It was surprising that all the fuels except the PRF100 should experience cool flame behaviour at this point and consideration was given to the possibility that this was merely a numerical artifact of either the FGAM or the multi-zone model itself. In order to check this, the cool flame ignition delay values of the various fuels obtained from the DKM simulations were examined in the region of interest. The cool flame ignition delay curves in this region are displayed in Figure 7.2.

It can be seen that all PRF fuels except PRF100 have a cool flame ignition delay in the range of 5 to 10 ms at a pressure of about 10 bar and the temperature range of 700 - 750 K. To confirm that the unburned gas was exposed to these temperatures for long enough to result in a cool flame, the temperature traces for zone 19 were plotted as function of crank angle for each of the simulations as in Figure 7.3. At the RON engine speed of 600 rpm, 5 to 10 ms corresponds to 18 to 36 CAD. Although the results of the static DKM simulations should be applied with caution to the changing temperature-pressure environment of the engine, given the relatively flat temperature response at around 700 K in the 30 CAD prior to TDC, it is certainly conceivable that a cool flame would manifest for the fuels considered.

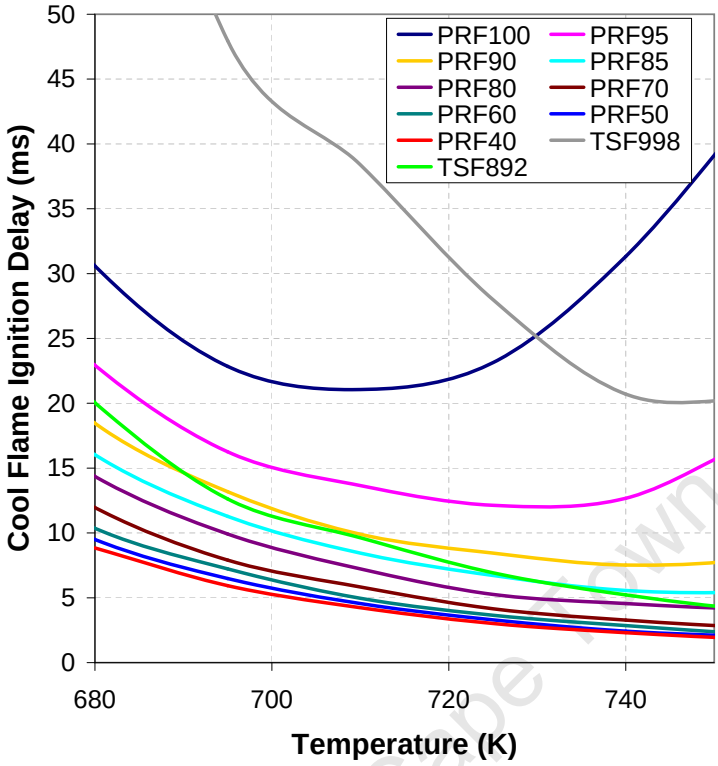

Figure 7.2: *Cool flame ignition delay from DKM simulations for PRF and TSF blends at 10 bar*

As PRF100 had a much longer CFID in this region, it then failed to exhibit a cool flame heat release. Resultantly, when autoignition did finally occur in the RON100 simulation, more energy was released than in the lower ON simulations, where some available energy had already been released during the cool flame. This increased heat release for the PRF100 simulation at knock, in nominally the same period of time as the other simulations, could conceivably result in the higher pressure rise rate observed. In short, the PRF100 RON simulation behaved differently to the other RON simulations because it did not exhibit cool flame behaviour during the RON test whereas the other PRFs did exhibit cool flame behaviour.

This may explain why the PRF100 RON simulation differed from the trend of the other RON simulations but not necessarily why it differed from the experimental results. The FGAM fit of overall ignition delay attained for PRF100 is shown in Figure 7.4. Although a generally good fit has been achieved for most initial temperatures and pressures, a significant deviation can be noted for the 10 bar simulations between 700 and 800 K. This is exactly the region in which the other PRF blends experienced cool flames in the RON simulations, while the PRF100 blend did not.

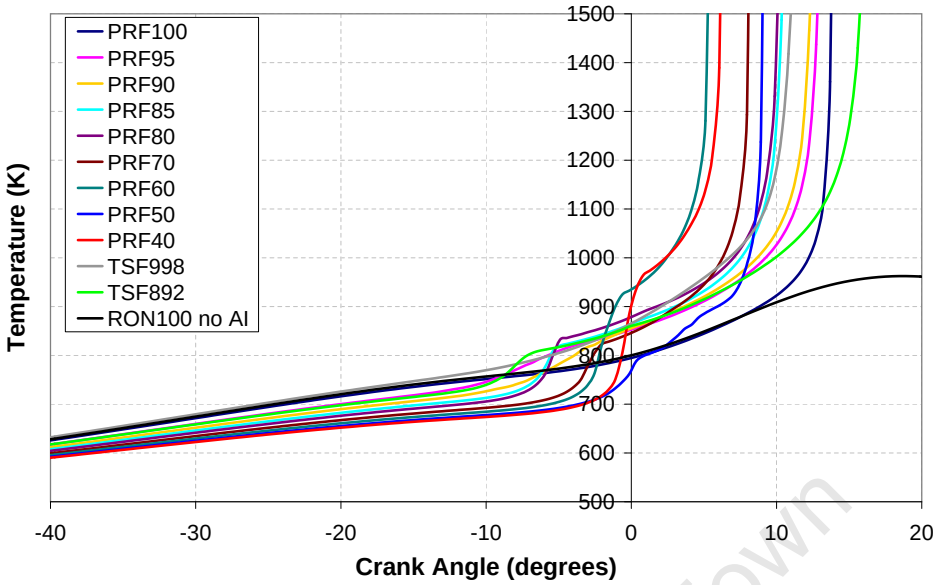

Figure 7.3: *Temperature traces of the first zone to autoignite for PRF and TSF blends at SKI*

When the FGAM fit was originally performed in this study, this discrepancy was not considered important as it was assumed that the most relevant portion of the autoignition profile would be that experienced by the end-gas immediately prior to the autoignition event. For PRF100 under RON conditions this would be in the region of 30 bar and 900 K. A better fit of the autoignition behaviour in the low temperature, low pressure region may have resulted in some minor heat release prior to final autoignition. That said, the longer CFID for PRF100 noted in Figure 7.2 was obtained directly from the DKM results and not the FGAM fit. It is also possible that in the real engine, species and radicals in the residual exhaust gas have an effect on the autoignition behaviour when mixed with the fresh charge [76]. The REG has been simply modelled as an inert diluent in this study. These may be some reasons why the experimental pressure trace produced a lower peak pressure rise rate than predicted by the model for the RON100 test.

Returning to the Temperature-Pressure domain plot in Figure 7.1, some other interesting observations can be made. Following the initial cool flames (where applicable), the curves continue along new compression lines until final autoignition at around 900 - 950 K and various pressures. Comparisons of the DKM post cool flame ignition delay results at 900 K and the relevant pressure for each of the PRFs (for example PRF80 at 900 K and 20 bar) once again yielded ignition delays in the region of 5 - 10 ms for all the fuels. The overall ignition delay for PRF100 at 900 K and 30 bar was also in this range.

For fuels exhibiting only single stage behaviour in the RON test such as PRF100 the onset of autoignition would seem to coincide with a temperature of approximately 900 K and

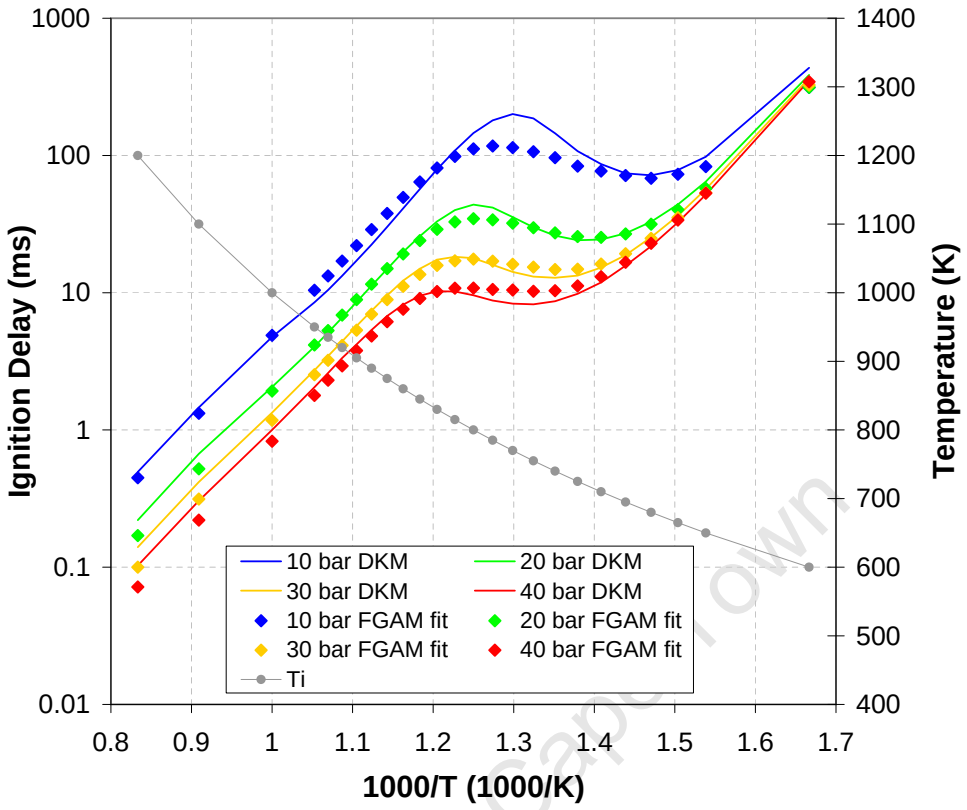

Figure 7.4: *FGAM fit to the DKM overall ignition delay profile for PRF100*

the corresponding pressure along the compression curve. For fuels exhibiting cool flame behaviour during the RON test, the onset of autoignition would thus seem to be dependent on two characteristic operating points:

1. The cool flame ignition delay at approximately 700 K and 10 bar

2. The post cool flame ignition delay at approximately 900 K and the pressure corresponding to compression from the post cool flame ceiling temperature and pressure to 900 K.

In the previous studies of Yates et al [11] and Mehl et al [66], the compression curves of the RON and MON test were overlaid on contour plots of overall ignition delay in the temperature-pressure domain. In these studies it was implied that the intersection of these compression curves with the contour line of some characteristic ignition delay time, would yield the onset of autoignition and thus knock. The above analysis of this study would indicate that such an approach is perhaps too simplistic for description of the RON test, as both the cool flame ignition delay and the fact that the engine compression curve deviates from the adiabatic compression curve after the cool flame, would affect the onset of knock.

If this cool flame manifestation in the RON test is in fact real and measurable, the above analysis may become increasingly relevant to future production engines. The Mazda SKYACTIV-G concept, for example, actively uses the cool flame as part of its knock control strategy [69]. A single stage fuel may therefore have a very high octane rating but perform poorly in such an engine due its lack of cool flame behaviour. This would also apply to a supposedly 2-stage fuel such as iso-octane, which does not exhibit cool flame behaviour under the specific engine operating conditions.

It must be stressed that the above analysis is based on the assumption that the results of the multi-zone model are in fact representative for the RON40 to RON95 simulations. The initial conditions, specifically the initial temperature at IVC and residual exhaust gas fraction, have not been confirmed. However the good agreement between the simulations and experimental results would suggest that they offer appropriate representation.

Having shown that the choice of the RON100 test as a calibration point for the multi-zone model may have been erroneous, the multi-zone model was recalibrated to fit the experimental results of PRF85 running under RON85 test conditions. This required a minor adjustment in the residual exhaust gas fraction from 20% to 15%. All the RON simulations were then re-run with this reduced REG fraction of 15%. The peak pressure values and MFB at knock point for this set of simulations are shown in Figures 7.5 and 7.6. The initial results with a REG fraction of 20% are included for comparison.

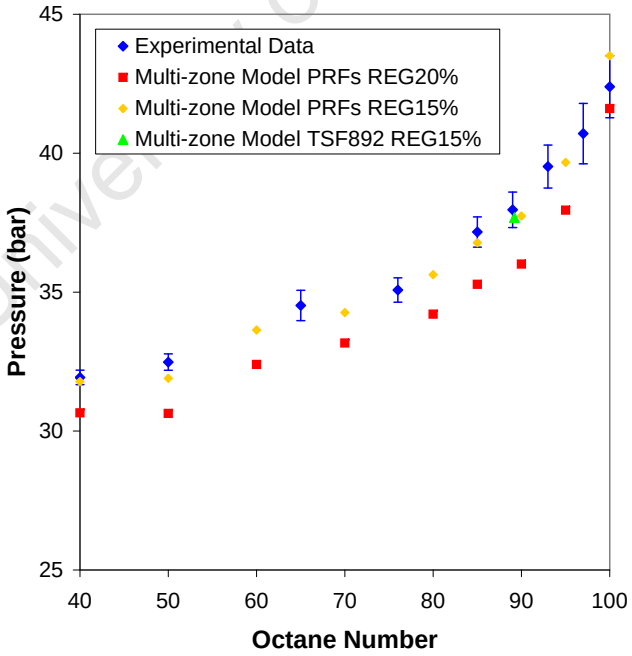

Figure 7.5: *Peak pressure values for RON simulations with 15% REG compared with experimental data of [73] and simulations using 20% REG*

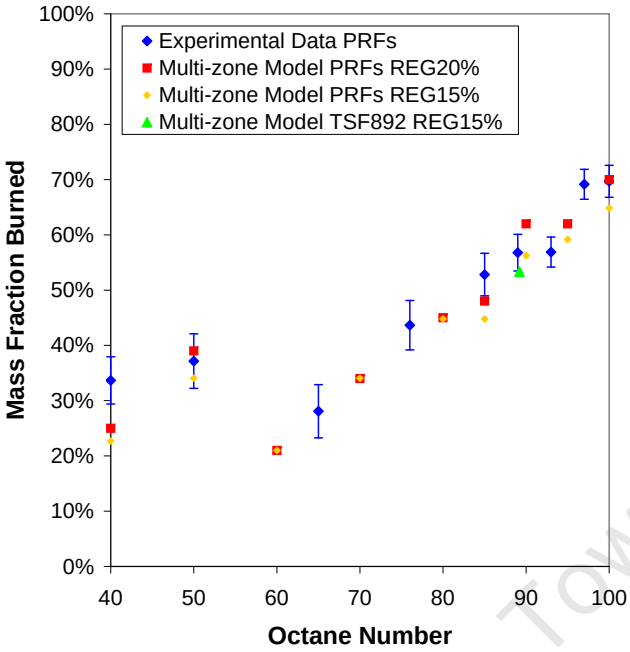

Figure 7.6: *MFB at knock point for RON Simulations with 15% REG compared with experimental data of [73] and simulations using 20% REG*

It can be seen that the peak pressure values with the new REG value compare very well with the experimental results. Furthermore the MFB values at knock point remained fairly consistent. The results of the TSF892 simulation are also much more consistent with the values for the PRFs. These results indicate that:

1. The multi-zone model is able to simulate the RON test with even better accuracy than previously thought.

2. All conclusions from previous analysis, even though based on the less satisfactory calibration on the RON100 test, should still hold.

7.2 Use of the FGAM as an autoignition prediction model

The use of the FGAM, instead of a detailed kinetic model substantially reduced the computational time required by the Multi-zone model. A typical 20 zone Engine simulation required approximately 30 minutes on a standard desktop PC (Dual Core 2GHz Processor with 2GB of RAM) . By contrast a single, constant volume Detailed Kinetic Simulation run in CHEMKIN^{TM} 4.1 required between 30-60 minutes. Running multiple zones with a DKM in a changing temperature-pressure simulation would take a single run to the order of days.

In order to fit the FGAM to a given fuel, generating the required DKM autoignition profile would take on average 2 days and optimising the reaction rate coefficients an additional 2 days. From thereon the FGAM could be used repeatedly with significantly lower computational effort. The calibrated FGAM would also not be limited to these simulations but could be further used for HCCI and other auto-ignition simulation applications by other researchers. The continuous improvement of computation technology will likely enable the use of DKMs in this multi-zone model in the near future. The FGAM does still have the advantage that its computational efficiency enables more simulations to be run in a given amount of time, which is of great value in an investigative study such as this.

An alternate option would be the use of reduced or skeletal models, which are more computationally efficient than DKMs. However it must be recalled that the cool flame behaviour of such models is generally not well validated. Use in an application such as this, where cool flame behaviour is potentially very important (as discussed in the previous section) would therefore need to be done with caution.

Although the FGAM was found to be able to fit the autoignition profiles of the PRF blends with good accuracy, some difficulty was encountered in fitting the ternary TSF blends of toluene, iso-octane and n-heptane, particularly with regards to the cool flame heat release rates. It has been documented that the autoignition behaviour of toluene/iso-octane blends is not fully understood, with some peculiarities in the blending behaviour [18]. This may explain why the FGAM, which was developed primarily with paraffin autoignition chemistry in mind, could not provide as good a fit for the blend TSF998 (74% toluene, 10% iso-octane, 16% n-heptane). As a result only the blend of TSF892, which consists only of toluene and n-heptane, was included in this study.

Based on the good results obtained in this implementation of the FGAM, it is proposed that further validation and investigation of this autoignition model would enable TSF and other blends to be more reliably modelled. In particular the FGAM requires validation for rich mixtures. Although all simulations in this study were performed under stoichiometric conditions, the Octane rating tests require that the air-fuel ratio be set to that producing maximum knock and for many fuels this would be just rich of stoichiometric [73].

The numerical methods used in the implementation of the FGAM also require some consideration. A simple Euler integration method was used to integrate the reaction rate differential equations set up by the FGAM. Many faster and more accurate integration techniques are available and discussed in Appendix B. Given the relatively stiff set of equations to be dealt with, their use does require some careful consideration but there exist methods designed specifically for such systems. Use of such methods would not only speed up the implementation of the FGAM in the multi-zone model but also the calibration process in which 1000s of autoignition simulations are potentially performed.

In this study, a Particle Swarm Optimisation (PSO) method was used to optimise the calibration coefficients of the FGAM to fit the various autoignition profiles. The PSO itself can be calibrated to more efficiently explore the solutions space and converge on a solution for a given problem. Traditional gradient based solvers were considered inappropriate for optimising a non-linear system such as this. However they may still be able to be applied to "polish" solutions generated by the PSO. Other optimisation methods such as genetic algorithms [77] are also available and their use should be investigated.

7.3 Performance of the Multi-zone Engine Model

This implementation of a multi-zone model showed proof of concept in its ability to emulate the pressure development in the CFR engine. Even with the acknowledged large simplifications and assumptions made, the results still showed very good agreement with experimental data in the parametric study and simulation of the RON test. It may be possible to further increase the accuracy of the model results by incorporating various other sub-models.

A manifold and in-cylinder fuel evaporation study would provide a better set of initial conditions for both the temperature magnitude and in-cylinder distribution. It is notable that despite the extensive studies of the CFR engine and CFD studies of other engines, there is a distinct void in the literature of CFD modelling of the CFR engine under Octane test conditions.

The knock measurement device in the Octane Rating tests makes use of a filtered rate of change of pressure signal. The effect of filtering is not only to eliminate high and/or low frequencies but also to make the peak value of the signal dependent on the development of the signal immediately prior to that point. Swarts et al [12] have already shown that simulation of the output of such a filtering system is possible on the actual pressure traces recorded in the engine. Applying such a filter to the results of the multi-zone model should also therefore be possible but would require simulations with a much higher timescale resolution (ie. smaller timesteps of approximately 0.02ms). In this way the results of the model could be directly interpreted in terms of Knock Intensity readings of the Octane Rating tests.

A flame propagation model would remove the need for the empirically calibrated Wiebe description of flame propagation that was used. Various possible flame propagation models have been described in Section 2.5.2. Additionally heat transfer effects, both between zones and to the cylinder walls, could be more accurately described. The combination of all these submodels including the FGAM and pressure signal filter could take the form of a fully inclusive CFD model of the CFR engine.

The unsatisfactory MON results have been attributed to the use of inappropriate initial conditions. The initial conditions used were minor modifications of the RON simulation parameters. A re-evaluation of the MON results in Figures 6.6-6.8 show that the trends observed in the MON simulations, whilst not resembling the trends of the experimental results, are quite similar to the trends observed in the RON simulations. Again looking back at the comparison between the experimental results of the RON and MON tests in Figures 4.2-4.4, the actual behaviour of the PRF fuels under RON and MON test conditions are completely different, with divergent trends exhibited.

This would suggest that the initial conditions of RON and MON test conditions are also substantially different, resulting in the autoignition behaviour of the various fuels manifesting differently under the two test conditions. This initial condition argument is supported by the peak pressure results of Figure 4.1, where at higher Octane numbers, the peak pressures of the RON test remain significantly higher than the those of the MON test, even though the critical compression ratios corresponding to the MON test are higher than those for RON at these points.

It is worth mentioning that in order to control the mixture temperature for the MON test, an additional heating section is added to the inlet system and a different sized venturi is used for the carburettor [2,3]. This has the effect of both lengthening the flow path of the inlet gas and adding additional obstacles to the flow. These effects together with the higher engine speed of the MON test could significantly alter the flow dynamics and therefore the gas exchange process of the CFR engine, resulting in vastly different initial conditions for the two tests. It is notable that the Mazda SKYACTIV-G concept pays particular heed to manifold design in order to reduce residual exhaust gas, in recognition of the important roles that REG and initial temperature play in the manifestation of knock [69].

A detailed investigation of the CFR engine breathing process and resultant inlet conditions is outside the scope of this thesis. However a CFD modelling study of the CFR intake system is currently underway at the Sasol Advanced Fuels Laboratory and further experimental work to better determine the initial conditions of the Octane rating tests is planned. If these initial conditions can be more accurately determined and used to re-apply the multi-zone model to the MON test, it would provide a valuable tool in the study of Fuel Octane Sensitivity.

Chapter 8

Conclusions

Following the development of the Multi-zone engine model and its application to simulation of the Octane rating tests, a few concluding remarks can be made.

1. The characteristic knock pressure development in the CFR engine must be adequately modelled in order to determine standard knock intensity and thus classify the Octane rating of modelled fuels. Current modelling approaches which use detailed chemical kinetic models in a single unburned zone can accurately model the onset of autoignition, but are unable to reproduce the distinct post-knock point pressure development in the CFR engine.

2. A multi-zone model, incorporating the Functional Global Autoignition Model proposed in [39] and an initial temperature gradient within the cylinder, is able to both predict the onset of autoignition and simulate a cascading autoignition. This results in a pressure development matching that exhibited under knocking RON test conditions in the CFR engine and strongly suggests that cascading autoignition is in fact the cause of this pressure development.

3. The multi-zone model responds appropriately to changes in the operating parameters of inlet pressure, temperature and compression ratio.

4. Variation of the burn duration was shown to emulate the effects of cycle-cycle variation, both in the position of the knock point in varying cycles and with the uniformity of pressure rise rate in each cycle.

5. Simulations of PRF blends running at the critical compression ratios for their respective RON ratings produced results consistent with real engine experiments, under these conditions, with respect to knock peak pressure rise rate and mass fraction burned at knock point.

6. The simulation of PRF100 under RON conditions deviated from the trends of lower ON PRFs and experimental results. It has been argued that the cool flame behaviour prior to final autoignition delay plays a pivotal role in the onset of autoignition. It is

differences between the cool flame behaviour of PRF100 and the other PRFs, as well as the less satisfactory fit of the FGAM in the low temperature, low pressure region of the PRF100 autoignition profile that has resulted in this deviation.

7. Cool flame behaviour during the Octane rating tests may be extremely relevant to future production engines that actively make use of cool flame heat release in knock control strategies.

8. The experimental results of MON tests were not adequately simulated by the multi-zone engine model. It is proposed that this is due to the use of incorrect initial conditions particularly with regards to initial temperature at IVC and residual exhaust gas fraction.

9. Fitting the FGAM to a set of detailed chemical kinetic simulations allowed the use of a computationally efficient model to simulate autoignition in multiple zones, subject to a changing temperature-pressure environment, whilst still accurately emulating cool flame timing and heat release dynamics. The natural extension of this is implementation in a CFD code with more accurate submodels.

Chapter 9

Recommendations

Although the results of this initial implementation of the Multi-zone engine model and Functional Global Autoignition Model were quite satisfactory, it would certainly be possibly to improve their performance. It is in this light that the following recommendations are made for future implementations of the Multi-zone engine model and the FGAM:

1. An in-depth CFD modelling and experimental study should be performed in order to obtain more accurate initial conditions for input into the Multi-zone model. Of particular interest is the residual exhaust gas fraction and in-cylinder temperature.

2. The use of a combustion model, that is able to depict flame propagation in the unique geometry and flow environment of the CFR engine, should be investigated to account for minor differences in burn rates between different fuels and under different operating conditions.

3. The unburned zones in the multi-zone model were modelled as being closed and adiabatic. A CFD model of normal combustion in the CFR engine may inform a more realistic representation, which may include mass and heat transfer between zones. This may also result in a better description of heat transfer to the cylinder walls.

4. Residual exhaust gas has been treated as as inert diluent in this model. The actual effect of REG on autoignition should be further investigated and incorporated in the model if possible.

5. The code for the implementation of the multi-zone model was written in VBA for reasons of compatibility with previous work. More computation focused languages such as C^{++} and Matlab may be a better choice for future versions of the model and result in a decrease in computation time.

6. As a proof of concept model, very basic numerical methods were used in the implementation to ensure stability of the model. Methods are available that are more computationally efficient and accurate and these should be incorporated into the model where possible.

7. A thorough mathematical treatment of the FGAM should be performed including:
   (a) Better numerical methods for solving the reaction rate system of differential equations.
   (b) Optimisation methods for fitting the FGAM to autoignition profiles.
   (c) Investigation of the applicability of the FGAM to single stage fuels, olefins, blends and rich mixtures

8. With improving technological resources, it may be possible that a full detailed kinetic mechanism can be implemented in the multi-zone model. However the computational efficiency of the FGAM is still valuable in enabling comprehensive studies with a large data set of simulations to be performed in a reasonable period of time. Full DKM simulations may prove useful in validating the results of the FGAM in the changing temperature-pressure environment of the engine as validation has only previously been performed in constant volume simulations.

9. The multi-zone model incorporating the FGAM has been used specifically to model the peculiarities of knock in the CFR engine. It may prove valuable to apply this approach to the modelling of standard production engines as well as new technologies such as spark-assisted HCCI and the Mazda SKYACTIV-G concept.

References

[1] J. B. Heywood, *Internal Combustion Engine Fundamentals*. New York: McGraw Hill, 1988.

[2] "Standard test method for knock characteristics of motor fuels by the motor method." ASTM Standard D2700-83, 1984.

[3] "Standard test method for knock characteristics of motor fuels by the research method." ASTM Standard D2699-83, 1984.

[4] V. Mittal and J. B. Heywood, "The shift in relevance of fuel RON and MON to knock onset in modern SI engines over the last 70 years," SAE Technical Paper Series, 2009-01-2622, 2009.

[5] G. Kalghatgi, "Fuel anti-knock quality - part I. engine studies," SAE Technical Paper Series, 2001-01-3584, 2001.

[6] A. D. B. Yates, A. Swarts, and C. L. Viljoen, "An investigation of anomalies identified within the ASTM Research and Motor Octane scales," SAE Technical Paper Series, 2003-01-1772, 2003.

[7] A. Swarts, C. Viljoen, and R. Coetzer, "The analysis of observed burn rates in a spark-ignition engine and the relation to fuel properties," SAE Technical Paper Series, 2003-01-3125, 2003.

[8] A. Swarts and A. Yates, "In-cylinder fuel evaporation and heat transfer information inferred from the polytropic character of the compression stroke in a spark-ignition engine," SAE Technical Paper Series, 2004-01-1856, 2004.

[9] A. Swarts, A. Yates, C. Viljoen, and R. Coetzer, "Standard knock intensity revisited: Atypical burn rate characteristics identified in the CFR Octane rating engine," SAE Technical Paper Series, 2004-01-1850, 2004.

[10] A. Swarts, A. Yates, C. Viljoen, and R. Coetzer, "A further study of inconsistencies between autoignition and knock intensity in the CFR Octane rating engine," SAE Technical Paper Series, 2005-01-2081, 2005.

[11] A. D. B. Yates, A. Swarts, and C. L. Viljoen, "Correlating auto-ignition delays and knock-limited spark-advance data for different types of fuel," SAE Technical Paper Series, 2005-01-2083, 2005.

[12] A. Swarts and A. Yates, "Insights into the role of autoignition during octane rating," SAE Technical Paper Series, 2007-01-0008, 2007.

[13] A. Thiart, "A CFD investigation of fuel evaporation in the CFR engine." Unpublished Masters Thesis, University of Cape Town, 2011.

[14] M. M. Andreae, W. K. Cheng, T. Kenney, and J. Yang, "On HCCI engine knock," SAE Technical Paper Series, 2007-01-1858, 2007.

[15] R. Nates, "The quantification of knock in terms of engine durability," tech. rep., University of Cape Town, 1993.

[16] R. Stone, *Introduction to internal combustion engines*. Basingstoke, UK: Palgrave-Macmillan, 3rd ed., 1999.

[17] S. Tanaka, F. Ayala, J. C. Keck, and J. B. Heywood, "Two-stage ignition in HCCI combustion and HCCI control by fuels and additives," *Combustion and Flame*, vol. 132, pp. 219–239, 2003.

[18] G. Vanhove, G. Petit, and R. Minetti, "Experimental study of the kinetic interactions in the low-temperature autoignition of hydrocarbon binary mixtures and a surrogate fuel," *Combustion and Flame*, vol. 145, pp. 521–532, 2006.

[19] B. M. Gauthier, D. F. Davidson, and R. K. Hanson, "Shock tube determination of ignition delay times in full-blend and surrogate fuel mixtures," *Combustion and Flame*, vol. 139, pp. 300–311, 2004.

[20] M. A. Oehlschlaeger, D. F. Davidson, and R. K. Hanson, "Investigation of the reaction of toluene with molecular oxygen in shock-heated gases," *Combustion and Flame*, vol. 147, pp. 195–208, 2006.

[21] G. Floweday, "A new functional global auto-ignition model for hydrocarbon fuels - part 1 of 2: An investigation of hydrocarbon fuel auto-ignition behaviour and existing global auto-ignition models," SAE Technical Paper Series, 2010-01-2161, 2010.

[22] G. Floweday, *Two Contrasting Approaches to Auto-Ignition Modelling for HCCI Engines*. PhD thesis, University of Cape Town, February 2010.

[23] J. Griffiths, "Reduced kinetic models and their application to practical combustion systems," *Progress in Energy and Combustion Science*, vol. 21, pp. 25–107, 1995.

[24] M. Mehl, H. J. Curran, W. J. Pitz, and C. K. Westbrook, "Detailed kinetic model of gasoline surrogate mixtures," in *Proceedings of the European Combustion Meeting 2009*, 2009.

[25] J. C. G. Andrae, "Development of a detailed kinetic model for gasoline surrogate fuels," *Fuel*, vol. 87, pp. 2013–2022, 2008.

[26] T. Lu and C. K. Law, "Toward accommodating realistic fuel chemistry in large-scale computations," *Progress in Energy and Combustion Science*, vol. 35, pp. 192–215, 2009.

[27] D. Flowers, B. Pitz, M. Mehl, M. Sarthy, C. Westbrook, S. Aceves, N. Killingsworth, M. McNenly, T. Piggott, M. Havstad, and R. Whitesides, "Chemical kinetics research on HCCI & diesel fuels and compuationally efficient modeling of high-efficiency clean combustion engines," in *DEER Conference*, (Detroit,MI), September 2010.

[28] Y. Sakai, A. Miyoshi, M. Koshi, and W. J. Pitz, "A kinetic modeling study on the oxidation of primary reference fueltoluene mixtures including cross reactions between aromatics and aliphatics," *Proceedings of the Combustion Institute*, vol. 32, pp. 411–418, 2009.

[29] F. Battin-Leclerc, "Detailed chemical kinetic models for the low-temperature combustion of hydrocarbons with application to gasoline and diesel fuel surrogates," *Progress in Energy and Combustion Science*, vol. 34, pp. 440–498, 2008.

[30] W. J. Pitz, N. P. Cernansky, F. L. Dryer, F. N. Egolfopoulos, J. T. Farrell, D. G. Friend, and H. Pitsch, "Development of an experimental database and chemical kinetic models for surrogate gasoline fuels," SAE Technical Paper Series, 2007-01-0175, 2007.

[31] K. Naitoh and T. Ise, "Autoignition model optimized based on simple artificial brain," SAE Technical Paper Series, 2003-01-3229, 2003.

[32] I. P. Androulakis, "Kinetic mechanism reduction based on an integer programming approach," *AIChE Journal*, vol. 46, pp. 361–371, February 2000.

[33] M. Schreiber, A. S. Sakak, A. Lingens, and J. Griffiths, "A reduced thermokinetic model for the autoignition of fuels with variabel octane ratings," in *Twenty-Fifth Symposium (International) on Combustion*, pp. 933–940, The Combustion Institute, 1994.

[34] U. C. Müller, N. Peters, and A. Linan, "Global kinetics for n-heptane ignition at high pressures," in *Twenty-Fourth Symposium (International) on Combustion*, pp. 777–784, The Combustion Institute, 1992.

[35] A. M. Douaud and P. Eyzat, "Four-octane-number method for predicting the anti-knock behaviour of fuels and engines," SAE Technical Paper Series, 780080, 1978.

[36] J. C. Livengood and P. C. Wu, "Correlation of autoignition phenomena in internal combustion engines and rapid compression machines," in *5th Symposium (International) on Combustion*, The Combustion Institute, 1955.

[37] A. D. B. Yates and C. L. Viljoen, "An improved empirical model for describing auto-ignition," SAE Technical Paper Series, 2008-01-1629, 2008.

[38] F.-A. Lafossas, M. Castagne, J. P. Dumas, and S. Henriot, "Development and validation of a knock model in spark ignition engines using a CFD code," SAE Technical Paper Series, 2002-01-2701, 2002.

[39] G. Floweday, "A new functional global auto-ignition model for hydrocarbon fuels - part 2 of 2: Model formulation, development and performance assessment," SAE Technical Paper Series, 2010-01-2169, 2010.

[40] D. R. Mott, *New Quasi-Steady-State and Partial-Equilibrium Methods for Integrating Chemically Reacting Systems*. PhD thesis, University of Michigan, 1999.

[41] Waukesha Engine Division Dresser Industries Inc., "An International Historic Mechanical Engineering Landmark: The Waukesha CFR Fuel Reaserch Engine." Bulletin No. 1163, Waukesha, WI, June 1980.

[42] Waukesha Engine Division Dresser Industries Inc. Available: http://www.waukeshaengine.com/images/CFR_Downloads/f1f2_octane_unit_lowres.jpg [19 January 2011], 2011.

[43] V. Mittal, J. B. Heywood, and W. H. Green, "The underlying physics and chemistry behind fuel sensitivity," SAE Technical Paper Series, 2010-01-0617, 2010.

[44] "Unleaded petrol." SABS Standard SANS 1598, 2006.

[45] D. P. Moran and A. B. Taylor, "An evaporative and engine-cycle model for fuel octane sensitivity prediction," SAE Technical Paper Series, 952524, 1995.

[46] V. Arrigoni, G. Cornetti, G. Spallanzi, F. Calvi, and A. Tontodonati, "High speed knock in SI engines," SAE Technical Paper Series, 741056, 1974.

[47] G. Konig, R. Maly, D. Bradley, A. Lau, and C. Sheppard, "Role of exothermic centres on knock initiation and knock damage," SAE Technical Paper Series, 902136, 1990.

[48] H. J. Curran, W. J. Pitz, C. K. Westbrook, P. Gaffuri, and W. R. Leppard, "Autoignition chemistry in a motored engine: An experimental and kinetic modeling study," in *Western States section meeting, Tempe, AZ (United States)*, 1996.

[49] S. Hajireza, F. Mauss, and B. Sundn, "Two-zone model of gas thermodynamic state in SI engines with relevance for knock," in *The Fourth International Symposium COMODIA 98*, 1998.

[50] S. Hajireza, B. Sundn, and F. Mauss, "A three-zone model for investigation of gas behavior in the combustion chamber of si engines in relation to knock," SAE 1999-01-0219 SAE Technical Paper Series, 1999.

[51] A. Swarts, *Insights relating to octane rating and the underlying role of autoignition.* PhD thesis, University of Cape Town, 2006.

[52] A. Yates, A. Bell, and A. Swarts, "Insights relating to the autoignition characteristics of alcohol fuels," *Fuel*, vol. 89, pp. 83–93, 2010.

[53] G. D'errico, T. Lucchini, and A. Onorati, "Development and experimental validation of a combustion model with detailed chemistry for knock predictions," SAE Technical Paper Series, 2007-01-0938, 2007.

[54] S. M. Aceves, D. L. Flowers, C. K. Westbrook, J. R. Smith, W. Pitz, R. Dibble, M. Christensen, and B. Johansson, "A multi-zone model for prediction of HCCI combustion and emissions," SAE Technical Paper Series, 2000-01-0327, 2000.

[55] M. Mehl, A. Tardani, T. Faravelli, and E. Ranzi, "A multizone approach to the detailed kinetic modeling of HCCI combustion," SAE Technical Paper Series, 2007-24-0086, 2007.

[56] H. Xu, M. Liu, S. Gharahbaghi, S. Richardson, M. Wyszynski, and T. Megaritis, "Modelling of hcci engines: Comparison of single-zone, multi-zone and test data," 2005-01-2123, 2005.

[57] C. S. Daw, R. M. Wagner, K. D. Edwards, and J. B. G. Jr., "Understanding the transition between conventional spark-ignited combustion and HCCI in a gasoline engine," *Proceedings of the Combustion Institute*, vol. 31, pp. 2887–2894, 2007.

[58] W. J. Glewen, R. M. Wagner, K. D. Edwards, and C. S. Daw, "Aanlysis of cyclic variability in spark-assisted hcci combustion using a double wiebe function," *Proceedings of the Combustion Institute*, vol. 32, pp. 2885–2892, 2009.

[59] D. Veynante and L. Vervisch, "Turbulent combustion modeling," *Progress in Energy and Combustion Science*, vol. 28, pp. 193–266, 2002.

[60] A. Teraji, T. Tsuda, T. Noda, M. Kubo, and T. Itoh, "Development of a novel flame propagation model (UCFM: Universal Coherent Flamelet Model) for SI engines and its application to knocking prediction," SAE Technical Paper Series, 2005-01-0199, 2005.

[61] F. Perini, F. Paltrinieri, and E. Mattarelli, "A quasi-dimensional combustion model for performance and emissions of SI engines running on hydrogen-methane blends," *International Journal of Hydrogen Energy*, vol. 35, pp. 4687–4701, 2010.

[62] M. Mehl, T. Faravelli, E. Ranzi, F. Giavazzi, P. Scorletti, D. Terna, T. Lucchini, G. DErrico, and A. Onorati, "Experimental and kinetic modeling study of octane number and sensitivity of hydrocarbon mixtures in CFR engines," SAE Technical Paper Series, 2005-24-077, 2005.

[63] M. Mehl, T. Faravelli, E. Ranzi, T. Lucchini, A. Onorati, F. Giavazzi, P. Scorletti, and D. Terna, "Kinetic modeling of knock properties in internal combustion engines," SAE Technical Paper Series, 2006-01-3239, 2006.

[64] J. Beeckmann, J. Keppner, T. Glatz, and N. Peters, "Laminar burning velocities of dimethyl ether, n-heptane and iso-octane at high pressure," SAE Technical Paper Series, 2009-01-2656, 2009.

[65] T.-P. Hsiao, "Flame propagation model for the CFR engine inder knocking and non-knocking conditions," Master's thesis, University of Cape Town, 2006.

[66] M. Mehl, T. Faravelli, F. Giavazzi, E. Ranzi, P. Scorletti, A. Tardani, and D. Terna, "Detailed chemistry promotes understanding of octane numbers and gasoline sensitivity," *Energy and Fuels*, vol. 20, pp. 2391–2398, 2006.

[67] S. M. Aceves, D. L. Flowers, F. Espinosa-Loza, A. Babajimopoulos, and D. N. Assanis, "Analysis of premixed charge compression ignition combustion with a sequential fluid mechanics-multizone chemical kinetics model," SAE Technical Paper Series, 2005-01-0115, 2005.

[68] M. Hitomi, N. Iwata, M. Yamakawa, T. Nishimoto, T. Tohso, and T. Hayashi, "Spark-ignition gasoline engine." U.S. Patent 7 784 443 B2,, 31 August 2010.

[69] Mazda Motor Corporation, "Next-Generation Technologies: SKYACTIV," press information, Hiroshima Japan, 2010.

[70] M. A. Marr, J. S. Wallace, S. Chandra, L. Pershin, and L. Mostaghimi, "A fast response thermocouple for internal combustion engine surface temperature measurements," *Experimental Thermal and Fluid Science*, vol. 34, pp. 183–189, 2010.

[71] W. H. Press, S. A. Teukolsky, W. T. Vetterling, and B. P. Flannery, *Numerical Recipes in C: The Art of Scientific Computing*. Cambridge, UK: Cambridge University Press, 1992.

[72] M. W. Chase Jr., ed., *NIST-JANAF Thermochemical Tables*. Gaithersburg, MD: National Insititute of Science and Technology, 4th ed., 1998.

[73] A. Swarts, A. Yates, C. Viljoen, and R. Coetzer, "Experimental data from previous CFR engine studies [10-16]." kindly provided by the authors, 2003-2007.

[74] C. F. Taylor, *The Internal-Combustion Engine in Theory and Practice*, vol. 1. Cambridge, MA: The MIT Press, 2nd ed., 1966.

[75] R. J. Kee, F. M. Rupley, J. A. Miller, M. E. Coltrin, J. F. Grcar, E. Meeks, H. K. Moffat, A. E. Lutz, G. Dixon-Lewis, M. D. Smooke, J. Warnatz, G. H. Evans, R. S. Larson, R. E. Mitchell, L. R. Petzold, W. C. Reynolds, M. Caracotsios, W. E. Stewart, P. Glarborg, C. Wang, C. L. McLellan, O. Adigun, W. G. Houf, C. P. Chou, S. F.

Miller, P. Ho, P. D. Young, D. J. Young, D. W. Hodgson, M. V. Petrova, and K. V. Puduppakkam, "CHEMKIN release 4.1." Reaction Design, San Diego, CA, 2006.

[76] A. A. Burluka, K. Liu, C. Sheppard, A. J. Smallbone, and R. Woolley, "The influence of simulated residual and NO concentrations on knock onset for PRFs and gasolines," SAE Technical Paper Series, 2004-01-2998, 2004.

[77] A. P. Engelbrecht, *Computational Intelligence: An Introduction*. Chichester: John Wiley & Sons, Ltd, 2002.

[78] C. Sanderson, "Armadillo: An open source C++ linear algebra library for fast prototyping and computationally intensive experiments," tech. rep., NICTA, Brisbane, Australia, 2010.

[79] E. Anderson, Z. Bai, C. Bischof, S. Blackford, J. Demmel, J. Dongarra, J. Du Croz, A. Greenbaum, S. Hammarling, A. McKenney, and D. Sorensen, *LAPACK Users' Guide*. Philadelphia, PA: Society for Industrial and Applied Mathematics, third ed., 1999.

[80] MATLAB Release 2010b Natick, Massachusetts: The MathWorks Inc., 2010.

Appendix A

Calibration Coefficients for the Functional Global Autoignition Model

Table A.1: *FGAM Coefficients for PRF100, PRF95, PRF90, PRF85 and PRF80*

	PRF100	**PRF95**	**PRF90**	**PRF85**	**PRF80**
Error in Fit	13%	12%	9%	9%	10%
% iso-octane	100	95	90	85	80
% n-heptane	0	5	10	15	20
% toluene	0	0	0	0	0
Coefficients					
ln(A1a)	26.671	25.755	25.807	25.335	25.208
B1a	-15254	-14490	-14346	-14133	-14043
a1	-0.137	-0.159	-0.146	-0.146	-0.145
b1	0.712	0.77	0.77	0.853	0.81
ln(A1b)	20.244	20.057	20.546	19.95	20.298
n1b	-2.8	-2.748	-2.782	-2.723	-2.737
B1b	-14493	-17243	-17579	-17894	-18165
a2	1.208	1.009	1.08	1.123	1.137
c2	0.596	0.633	0.627	0.608	0.613
ln(A2)	22.43	24.418	24.379	25.06	26.117
n2	-1.111	-1.149	-1.156	-1.147	-1.167
B2	-7995	-8239	-8466	-8171	-8316
d3	2.81	2.859	2.842	2.925	2.841
ln(A3)	50.997	43.463	43.074	43.44	43.647
B3	-30694	-24088	-24404	-25540	-26177
c4	0.015	0.034	0.033	0.024	0.033
ln(A4)	36.791	47.84	46.972	46.095	46.662
B4	-23536	-33192	-33345	-30556	-30335
a5	0.987	0.634	0.891	0.894	0.92
b5	0.794	0.844	0.849	0.849	0.855
ln(A5)	21.235	21.462	21.457	21.468	21.461
n5	-0.556	-0.552	-0.503	-0.616	-0.57
B5	-17263	-16390	-16583	-16688	-16863
d6	5.875	5.149	5.16	5.738	5.703
b6	0.149	0.151	0.152	0.149	0.154
ln(A6)	25.342	24.864	24.733	27.056	27.139
n6	-0.034	-0.037	-0.037	-0.03	-0.031
B6	-15488	-15412	-15645	-16400	-15713
e7	2.578	0.704	0.701	1.739	2.016
b7	0.148	0.155	0.151	0.153	0.151
ln(A7)	13.161	11.872	11.792	11.992	12.032
n7	2.035	1.793	1.803	1.802	1.794
B7	-14863	-13384	-13175	-13505	-13494
f8	3.916	-0.102	-0.101	0.741	0.733
b8	0.216	0.145	0.144	0.166	0.166
ln(A8)	23.022	16.168	16.39	16.483	16.528
B8	-1340	-15726	-15615	-14447	-14603
g9	0.903	1.085	1.034	1.329	1.016
ln(A9)	20.513	21.367	21.298	25.574	21.747
B9	-45761	-44349	-45557	-45079	-45817

Table A.2: *FGAM Coefficients for PRF70, PRF60, PRF50, PRF40 and TSF892*

	PRF70	**PRF60**	**PRF50**	**PRF40**	**TSF892**
Error in Fit	9%	10%	6%	11%	15%
% iso-octane	70	60	50	40	0
% n-heptane	30	40	50	60	30
% toluene	0	0	0	0	70
Coefficients					
ln(A1a)	25.24	25.707	25.834	25.706	26.906
B1a	-13889	-14311	-14393	-14278	-15124
a1	-0.151	-0.151	-0.158	-0.152	-0.178
b1	0.931	0.731	0.724	0.747	0.702
ln(A1b)	19.881	19.611	19.126	19.821	22.202
n1b	-2.716	-2.574	-2.622	-2.57	-2.934
B1b	-19041	-18223	-17808	-19317	-20500
a2	1.724	2.19	2.198	2.339	1.006
c2	0.617	0.645	0.693	0.64	0.67
ln(A2)	26.338	26.3	23.998	26.399	23.293
n2	-1.391	-1.658	-1.658	-1.695	-1.515
B2	-9020	-7929	-8232	-7849	-7651
d3	2.827	2.633	2.383	2.877	2.255
ln(A3)	43.393	42.759	44.315	42.639	40.047
B3	-25412	-25626	-24671	-25093	-24641
c4	0.034	0.034	0.034	0.032	0.03
ln(A4)	46.08	45.221	42.387	44.341	46.797
B4	-30701	-28921	-31083	-29102	-33071
a5	0.94	0.933	0.751	0.941	0.909
b5	0.869	0.928	0.939	0.943	0.805
ln(A5)	20.749	19.137	19.302	19.36	22.084
n5	-0.553	-0.545	-0.541	-0.54	-0.488
B5	-16641	-15773	-15764	-15787	-18129
d6	5.675	5.623	5.603	5.659	5.182
b6	0.157	0.159	0.163	0.16	0.169
ln(A6)	26.383	28.552	28.715	28.938	25.162
n6	-0.031	-0.03	-0.032	-0.031	-0.036
B6	-15955	-16169	-16292	-15898	-16587
e7	1.686	1.674	1.693	1.735	0.731
b7	0.152	0.155	0.162	0.154	0.185
ln(A7)	12.575	13.152	13.253	13.221	11.509
n7	1.745	1.773	1.793	1.784	1.623
B7	-13489	-13565	-13728	-14148	-13149
f8	0.732	0.753	0.752	0.678	-0.118
b8	0.192	0.189	0.192	0.188	0.162
ln(A8)	19.597	23.61	24.553	23.573	17.397
B8	-13946	-13585	-12509	-13831	-14966
g9	1.011	0.942	0.912	0.885	0.873
ln(A9)	20.701	22.05	22.092	22.241	22.317
B9	-46819	-46704	-54226	-46704	-45525

Appendix B

Optimisation and Solving Algorithms

In implementing the multi-zone engine model (and submodels including the FGAM) in a computational code, several numerical methods were utilised. For each purpose, various algorithms were considered, varying in complexity, accuracy, stability and computational efficiency. These methods were drawn mostly from [71] and [77] and these two excellent resources should be consulted for further details of the methods described in this appendix. As this was to be a proof of concept model, the eventual methods selected were generally the simplest and most stable. However the model could be greatly improved by implementation of better algorithms and those that were considered are described below.

This is by no means meant to be an exhaustive review of available methods and it should be noted that new methods are constantly being developed. Libraries of these methods are also generally available for the main programming languages used by the scientific community such as `Armadillo` for C^{++} [78], `LAPACK` for `FORTRAN95` [79] and the built-in library in `MATLAB`® [80]. An understanding of these methods is however required before they can be implemented as the most efficient methods are designed for specific systems and need to be identified and applied as such.

B.1 Solution of Simultaneous Equations

B.1.1 General Non-linear Systems of Equations

A single equation of the form

$$y = f(x) \tag{B.1}$$

can be solved using Newton's method. This involves an iterative method by setting x_0 to some initial estimate and then obtaining progressively better solutions using the formula

$$x_{n+1} = x_n - \frac{f(x_n) - y}{f'(x)} \tag{B.2}$$

where $f'(x)$ is the derivative of $f(x)$. A general non-linear system of N equations in N unknowns is generally represented as

$$\begin{aligned} f_1(x_1, x_2, \cdots, x_N) &= 0 \\ f_2(x_1, x_2, \cdots, x_N) &= 0 \\ \vdots \qquad &= \vdots \\ f_N(x_1, x_2, \cdots, x_N) &= 0 \end{aligned} \tag{B.3}$$

In a similar fashion, this system can also be solved using an analogous multi-dimensional Newton's Method.

$$\mathbf{x}_{n+1} = \mathbf{x}_n + \mathbf{J}_n^{-1} \cdot (-\mathbf{f}_n) \tag{B.4}$$

where $\mathbf{x}$ is the vector of x variables
$\mathbf{f}$ is the vector of f functions to be set to 0
$\mathbf{J}$ is the Jacobian matrix of F

The Jacobian matrix ($\mathbf{J}$) is the matrix containing the partial derivatives of each of the functions (f) with respect to each of the variables (x) and is of the form

$$\mathbf{J} = \begin{pmatrix} \frac{\partial f_1}{\partial x_1} & \frac{\partial f_1}{\partial x_2} & \cdots & \frac{\partial f_1}{\partial x_N} \\ \frac{\partial f_2}{\partial x_1} & \frac{\partial f_2}{\partial x_2} & \cdots & \frac{\partial f_2}{\partial x_N} \\ \vdots & \vdots & \ddots & \vdots \\ \frac{\partial f_N}{\partial x_1} & \frac{\partial f_N}{\partial x_2} & \cdots & \frac{\partial f_N}{\partial x_N} \end{pmatrix} \tag{B.5}$$

The values of the partial derivatives can either be calculated explicitly, if the algebraic form of the functions are known and easily differentiable, or approximated through numerical differentiation.

To obtain each iterative solution, the matrix operation in Equation B.4 may appear fairly straightforward, however the matrix inversion operation involved in obtaining $\mathbf{J}^{-1}$ is extremely computationally expensive, involving calculations of the order N^3, where N is the number of equations to be solved [71]. Given that the values of the variables change at each iteration, the corresponding entries in the Jacobian also change, requiring a re-evaluation of the inverse at each iteration and further computational expense.

At this point several strategies can be adopted. An approximation of $\mathbf{J}^{-1}$ can be made, possibly increasing the total number of iterations required to obtain an acceptable solution but reducing the computational expense of each iteration. In selected cases, the entries

in $\mathbf{J}^{-1}$ can be updated without performing the full inversion operation. An alternative approach is to consider the fact that evaluating

$$\Delta\mathbf{x} = \mathbf{J}^{-1} \cdot (-\mathbf{f}) \tag{B.6}$$

is equivalent to solving for $\Delta\mathbf{x}$ in the system

$$\mathbf{J} \cdot (\Delta\mathbf{x}) = -\mathbf{f} \tag{B.7}$$

This is now a problem in the domain of numerical linear algebra in which there are a variety of methods available.

B.1.2 Linear Algebraic Equations

A system of M linear algebraic equations in N unknown variables has the following form

$$\begin{aligned} a_{11}x_1 + a_{12}x_2 + \cdots + a_{1N}x_N &= b_1 \\ a_{21}x_1 + a_{22}x_2 + \cdots + a_{2N}x_N &= b_2 \\ \vdots \qquad\qquad\qquad\qquad\quad &= \vdots \\ a_{M1}x_1 + a_{M2}x_2 + \cdots + a_{MN}x_N &= b_M \end{aligned} \tag{B.8}$$

or in matrix form

$$\mathbf{A} \cdot \mathbf{x} = \mathbf{b} \tag{B.9}$$

where $\mathbf{A}$ is the matrix containing the a coefficients
$\mathbf{x}$ is the vector of the x variables
$\mathbf{b}$ is the right hand side vector of b values

This system can be uniquely solved for the vector $\mathbf{x}$ if $M = N$. If $M < N$ (ie. more variables than equations) then the system is said to be *underconstrained*. If $M > N$ (ie. more equations than variables) the system is *overconstrained*. In each case there can either be no solutions to the system or an infinite number of solutions. If any of the equations is a linear combination of the others, then the system is said to be *degenerate* and once again can result in no or infinite solutions. In order to find a unique solution then, the system must consist of N linearly independent equations in N unknown variables.

Two additional problems may occur in attempting to solve such a system. Even though all equations may be linearly independent, some combinations may be close to linearly dependent. This may result in the numerical operations failing (eg. dividing by the difference between two numbers that are very close in magnitude may be numerically equivalent to dividing by zero). Additionally, scaling issues between the different equations (eg. the addition of a very big number to a very small number being approximately equal

to the original very big number) may results in roundoff errors that give incorrect solutions, even if the operations succeed. Good modelling practice would advise ensuring that the system is set up to avoid these problems, and the use of good methods that detect and compensate for these issues. It should be cautioned against using the latter as a substitute for the former, as even the best methods can break down when incorrectly applied.

Once again a distinction is made between *direct* methods that attempt to calculate the exact solution in a fixed number of steps, and *iterative* methods that converge upon a solution in multiple steps to within a desired error bound. Direct methods are generally very efficient at solving small, well-behaved systems. For larger, less well constrained systems, direct methods can result in large roundoff errors and therefore incorrect solutions. Iterative methods generally require an initial estimate at the solution which is incrementally improved. If this initial estimate is quite close to the actual solution then the system can converge quite quickly. Each iteration generally requires fewer operations than the execution of a direct method so it is the total number of iterations required that determines whether an iterative or direct method will obtain a solution quicker. Iterative schemes are generally better at avoiding the roundoff errors described above, though this is not always necessarily true. Both direct and iterative approaches can be configured to take advantage of *sparse* matrices, where there are few non-zero entries in the matrix compared to the total and these non-zero entries form a recognisable pattern.

Sparse Matrices

Most systems of equations encountered in the implementation of the Multi-zone model can be represented by sparse matrices, consisting of very few non-zero elements compared to the total matrix size. In addition, these matrices can be constructed so as to form a pattern such as those shown in Figure B.1.

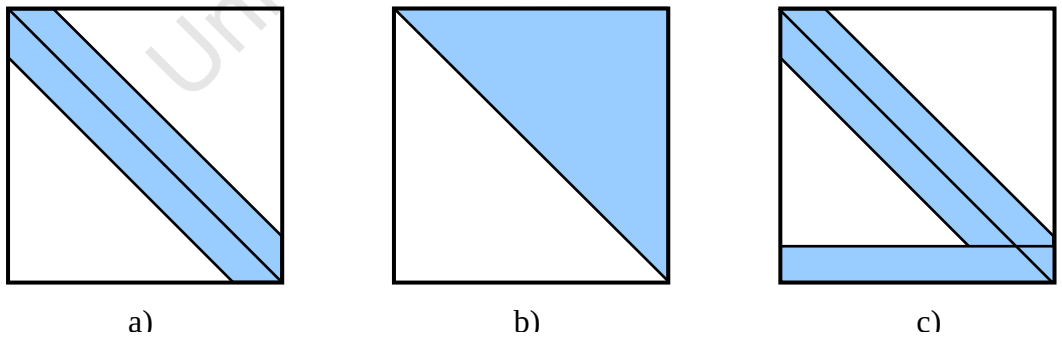

Figure B.1: *Examples of sparse matrix configurations: a) band diagonal; b) triangular; c) singly bordered band diagonal*

The advantage of such sparse matrices is three-fold:

1. If only the non-zero elements are stored, then the memory requirements to store the matrix can be significantly reduced.

2. It may not be necessary to loop through the zero-valued elements when performing matrix operations, which saves computation time.

3. Specific methods may be available that efficiently solve the particular form of sparse matrix.

In order to take advantage of these benefits, the first requirement is an indexing system that enables storage of only the essential elements of the matrix, while retaining sufficient information to enable the reconstruction of the original matrix. For example, a band diagonal matrix, consisting of the centre diagonal and the two adjacent diagonals, can easily be stored in a 3-column matrix, each containing one of the diagonals. Other schemes, such as the *row-indexed sparse storage mode* described in [71] may be more suitable for the particular form of sparse matrix encountered. A key advantage of such an indexing scheme is the reduced computational effort required for matrix multiplication.

A solution scheme that takes advantage of these "cheap" matrix multiplications, is the *biconjugate gradient method*. In the special case where $\mathbf{A}$ is symmetric and positive definite, this method is equivalent to minimising the function

$$f(x) = \frac{1}{2}\mathbf{x} \cdot \mathbf{A} \cdot \mathbf{x} - \mathbf{b} \cdot \mathbf{x} \tag{B.10}$$

which occurs when

$$\nabla f = \mathbf{A} \cdot \mathbf{x} - \mathbf{b} \tag{B.11}$$

is equal to 0. The minimisation is accomplished by traversing successive orthogonal directions until the minimum value of B.10 in that direction is found. After N iterations, the minimum over the entire vector space will have been found and this correspond to a solution to B.9.

As a final note, if the original non-linear system of equations to be solved for, can in fact be linearised, then the linear algebra methods described above can be directly applied to solve for the variables of interest. This approach should be adopted whenever possible, so long as it does not result in loss of acceptable accuracy.

B.2 Optimisation Methods

Optimisation methods are used for minimising (or maximising) functions of one or more variables. In this study, the calibration coefficients of the FGAM had to optimised to best fit the autoignition profiles generated by the Detailed Kinetic Mechanism of [24]. This involved minimisation of the function describing the error in fit. It is important to note

that although a function will generally have a single *global* minimum (the lowest possible value over the domain considered), it may also possess several *local* minima (where a differential change in any of the variables will result in an increase in the function, but not necessarily the absolute minimum value of the function). This difference is shown for the 1-dimensional case is Figure B.2.

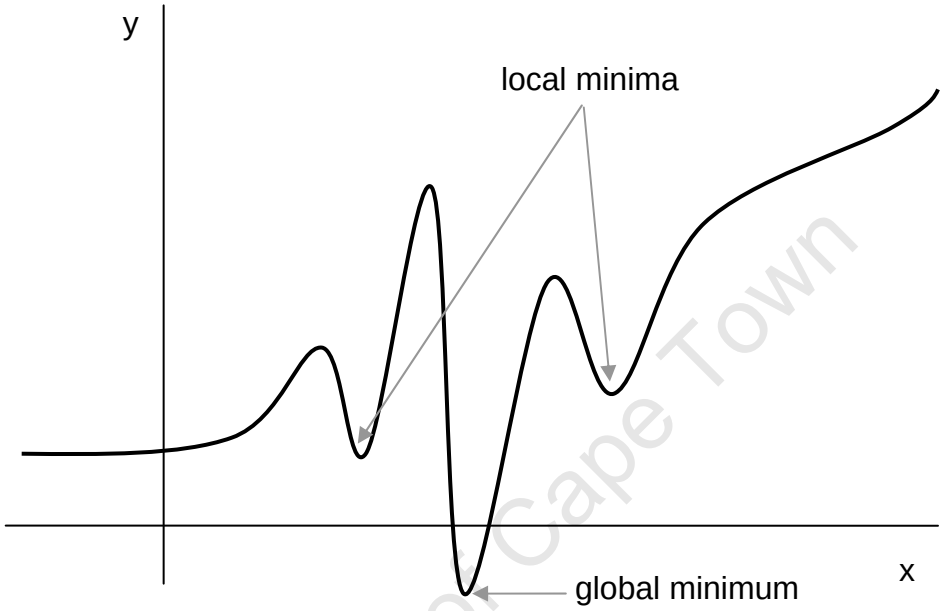

Figure B.2: *Local and global minima in a function of one variable*

Optimisation methods can also be used to solve systems of simultaneous equations. If all the terms of the equations are moved to the left hand side and expressed as functions, minimising the sum of the squares of these functions to zero will result in the solution of the equation system. However the minimisation function may settle on a non-zero local minimum which does not correspond to a solution, thus a simultaneous equation solver such as those described in B.1 should be used whenever possible.

In the categorisation of optimisation methods, a distinction is made between gradient based solvers and stochastic methods. Gradient based methods generally start at an initial guess and proceed incrementally in a direction that decreases the value of the function to be minimised. The major differences between methods therefore lie in the way this direction is chosen at each step and deciding how large a step to actually take along that direction. Because of the gradient based approach however, these methods are especially vulnerable to getting stuck in local minima.

Stochastic methods, by contrast, randomly populate the solution space with multiple possible solution points. Then through a combination of the best available current solutions

and some additional random components, new possible solutions are derived. This process is repeated, exploring the solution space, until an acceptable solution is found. Examples of such methods include Genetic Algorithms (GAs) and Particle Swarm Optimisation (PSO) and these are discussed below.

As a rule of thumb, gradient based methods perform better for smooth, well behaved functions, where a good initial guess for the location of the global minimum can made and speed of convergence is important. Stochastic methods are better for exploring a solution space in which multiple local minima exist, so as to find the overall global minimum. A combination of these methods may be useful, finding the general neighbourhood of the global minimum with a stochastic method, then using a gradient based method to "polish" the solution.

B.2.1 Gradient Based Methods

Most gradient based methods begin with the 2nd order Taylor approximation of the function $f(\mathbf{x})$ around a point $(\mathbf{x}_i)$, such that

$$f(\mathbf{x}) \approx f(\mathbf{x}_i) - \mathbf{b} \cdot (\mathbf{x} - \mathbf{x}_i) + \frac{1}{2}(\mathbf{x} - \mathbf{x}_i) \cdot \mathbf{A} \cdot (\mathbf{x} - \mathbf{x}_i) \tag{B.12}$$

where $-\mathbf{b}$ is the gradient vector (∇f) evaluated at $\mathbf{x}_i$

$$\nabla f = \begin{pmatrix} \dfrac{\partial f}{\partial x_1} \\ \dfrac{\partial f}{\partial x_2} \\ \vdots \\ \dfrac{\partial f}{\partial x_N} \end{pmatrix} \tag{B.13}$$

and $(\mathbf{A})$ is the Hessian Matrix evaluated at $\mathbf{x}_i$

$$\mathbf{A} = \begin{pmatrix} \dfrac{\partial^2 f}{\partial x_1^2} & \dfrac{\partial^2 f}{\partial x_1 \partial x_2} & \cdots & \dfrac{\partial^2 f}{\partial x_1 \partial x_N} \\ \dfrac{\partial^2 f}{\partial x_2 x_1} & \dfrac{\partial^2 f}{\partial x_2^2} & \cdots & \dfrac{\partial^2 f}{\partial x_2 \partial x_N} \\ \vdots & \vdots & \ddots & \vdots \\ \dfrac{\partial^2 f}{\partial x_N x_1} & \dfrac{\partial^2 f}{\partial x_N \partial x_2} & \cdots & \dfrac{\partial^2 f}{\partial x_N^2} \end{pmatrix} \tag{B.14}$$

when $\mathbf{x}_0$ coincides with the origin of the co-ordinate system $(\mathbf{p})$, Equation B.12 reduces to

$$f(\mathbf{x}) \approx f(\mathbf{p}) - \mathbf{b} \cdot \mathbf{x} + \frac{1}{2}\mathbf{x} \cdot \mathbf{A} \cdot \mathbf{x} \tag{B.15}$$

In *quasi-Newton methods*, the form given in B.12 is used to approximate ∇f for the function. At the minimum value of f, the gradient will be equal to $\mathbf{0}$ and this is found in a similar fashion to Newton's method in one dimension. In *line search methods*, the form given in B.15 is used to infer a sequence of directions in which to perform one-dimensional line minimisations.

Quasi-Newton Methods

The derivative of f in equation B.12 is given by

$$\nabla f(\mathbf{x}) = \nabla f(\mathbf{x}_i) + \mathbf{A} \cdot (\mathbf{x} - \mathbf{x}_i) \tag{B.16}$$

Setting $\nabla f(x) = 0$ multiplying through by the inverse of $\mathbf{A}$ gives

$$\mathbf{x} - \mathbf{x}_i = \mathbf{A}^{-1} \cdot \nabla f(\mathbf{x}_i) \tag{B.17}$$

Subtracting the expression in Equation B.17 evaluated at $i = j$ from the same expression evaluated at $i = j + 1$, yields the archetypal equation for the iterations required in the quasi-Newton methods:

$$\mathbf{x}_{j+1} = \mathbf{x}_j + \mathbf{A}^{-1} \cdot (\nabla f_{j+1} - \nabla f_j) \tag{B.18}$$

using the notation $\nabla f_i \equiv \nabla f(\mathbf{x}_i)$ for convenience. In practice, the actual Hessian matrix is not used but rather a sequence of matrices that converge on the inverse of A such that

$$\lim_{j \to \infty} \mathbf{H} = \mathbf{A}^{-1} \tag{B.19}$$

$$\mathbf{x}_{j+1} = \mathbf{x}_j + \mathbf{H}_{j+1} \cdot (\nabla f_{j+1} - \nabla f_j) \tag{B.20}$$

This quasi-Newton method is fairly straightforward to implement as an algorithm, however it does require the calculation of both partial derivatives with respect of each of the variables in $\mathbf{x}$. Where these cannot by determined analytically, they can be numerically approximated. This will however require several evaluations of the function f, which may not be efficient.

Line Search Methods

Possibly the most intuitive method of multi-variable minimisation would be to keep all variables constant except one and search for the value of this variable that results in the minimum function value. Then pick a different variable and repeat. This method will in most cases converge on a minimum but for functions in which the interaction between variables is quite complex, this convergence may be very slow, requiring several changes in direction in each of the variables. This may be analogous to descending a mountain, where

the direction of quickest descent is obvious, but optimising variables individually results in taking a safer path with multiple switchbacks, always heading generally downwards but covering more overall distance with a slower rate of descent.

This problem can be reduced with the use of *conjugate directions*. The underlying idea is that after minimising along a particular direction $\mathbf{u}$, it is possible to choose a new direction $\mathbf{u}$ that does not "interfere" with the existing minimisation.

Returning to the 2nd order Taylor approximation in Equation B.15, the gradient is given by

$$\nabla f = \mathbf{A} \cdot \mathbf{x} - \mathbf{b} \tag{B.21}$$

and further more, for a differential change in direction $\delta\mathbf{x}$

$$\delta\left(\nabla f\right) = \mathbf{A} \cdot \left(\delta\mathbf{x}\right) \tag{B.22}$$

At the point where the function has been minimised along $\mathbf{u}$, the gradient of the function must be perpendicular to $\mathbf{u}$ as in

$$\mathbf{u} \cdot \nabla f = 0 \tag{B.23}$$

In order for the new direction $\mathbf{v}$ not to interfere with the optimisation along $\mathbf{u}$, the gradient must remain perpendicular to $\mathbf{u}$ so

$$\mathbf{u} \cdot \delta\left(\nabla f\right) = 0 \tag{B.24}$$

It then follows that

$$\mathbf{u} \cdot \mathbf{A} \cdot \mathbf{v} \tag{B.25}$$

Vectors for which the relationship in B.25 hold are called *conjugate* and it is generally possible to construct a set of conjugate directions that span the solution space. For an N dimensional case, N lines minimisations along N conjugate directions will result in an exact minimisations for quadratic functions that can be exactly represented by the form in B.15. General functions to be minimised will of course not be exactly quadratic, however the strategy of minimising along conjugate directions will converge on a minimum quadratically.

If the gradient of the function can be easily computed, the orthogonal conjugate directions can be found more directly using the so called *conjugate gradient methods* (similar in origin but different in application to the method described in Section B.1.2). This requires fewer iterations than finding the conjugate directions without knowledge of derivatives, however once again calculation of these derivatives may themselves be computationally expensive.

B.2.2 Particle Swarm Optimisation

The Particle Swarm Optimisation (PSO) algorithm, as with many modern computational techniques, takes its inspiration from systems in the natural world. It was originally created by Eberhart and Kennedy in 1995 to simulate the behaviour of a flock of flying birds. It is perhaps most easily explained though by comparing it to a swarm of insects looking for food.

Each insect can wander the meadow looking for the best feeding spot. In addition each insect knows its own previous best spot and can communicate with its neighbourhood of insect to find the swarm best spot. Each individual insect will fly around, drawn to its personal best and the swarm's best, with some additional random behaviour. Exploring the meadow in this way, the swarm will eventually converge on the best possible feeding spot.

In a computational implementation of the PSO to solve a multi-variable optimisation problem of N variables, the solution space is randomly populated with multiple *particles*. This number need not be as large as N. Each particle has a *position* vector ($\mathbf{x}$) corresponding to a possible solution (the values of each of the N variables). In addition, each particle has a *velocity* vector ($\mathbf{v}$) and a vector describing its personal best position (**pbest**). The global best position is also stored as a vector (**gbest**) and is accessible to all the particles.

In order to obtain the personal and global bests of the particles and swarm, a *fitness function* is evaluated. This fitness function is generally the function to be optimised. If the function evaluation at the current position of a particle is better (either higher or lower value depending on how the function is configured) than at its current personal best then **pbest** is changed to its current $\mathbf{x}$. If, in addition, the function evaluation is better the the global best, then **gbest** is changed to the current $\mathbf{x}$.

The system is initialised by randomly generating positions for each of the particles. Initial velocities are set to $\mathbf{0}$. All **pbest** vectors are set to the initial particle positions. The fitness function is evaluated at each of the positions and the **gbest** is selected. The algorithm then proceeds as follows.

The velocity for each particle is updated by

$$\mathbf{v}_{t+1} = \omega \mathbf{v}_t + \rho_1 c_1 (\mathbf{pbest} - \mathbf{x}_t) + \rho_2 c_2 (\mathbf{gbest} - \mathbf{x}_t) \tag{B.26}$$

The position for each particle is then updated by

$$\mathbf{x}_{t+1} = \mathbf{x}_t + \mathbf{v}_t \tag{B.27}$$

The fitness function is re-evaluated at each of the new positions and the **pbest** and **gbest** vectors updated if necessary. This procedure is repeated until an acceptable solution is

found or the system converges.

In Equation B.26 c_1 and c_2 are weighting coefficients determining how strongly the particle is drawn to either its personal best or the global best respectively. Typical values used are $c_1 = 2$, $c_2 = 2$. In order to add some random behaviour to the system, these weighting coefficients are modified by random numbers, ρ_1 and ρ_2 with values between 0 and 1. These random values are generated for each particle at each solution step.

The ω coefficient is used to impose an inertia on the system so that that particle maintains a component of motion in the direction it was initially moving. A high ω value will result in greater exploration of the solution space, whereas a lower ω values tend to focus search on the local region. Typical values are around $\omega = 0.8$. A common strategy is to begin the optimisation with a high ω value and then reduce it over time. In order to ensure convergence however, either a maximum value should be set for the velocity or the following relation must hold.

$$\omega > \frac{1}{2}(c_1 + c_2) - 1 \tag{B.28}$$

with $\omega \leq 1$.

In general the PSO algorithm is very good at exploring the solution space and eventually finding a global minimum, without being trapped in local minima, because of the approach of using multiple particles to converge from different directions. This is especially useful for functions with seemingly erratic behaviour such as the optimisation of the FGAM calibration coefficients. The many evaluations of the fitness function for each particle at each iteration can however be extremely time consuming. This time requirement can be further increased by the fact that the random particle wandering, which enables it to explore so well, can also result in evaluation of the fitness function at possible solutions that are very far away from the optimum. Evaluation of the fitness function at these "bad" points can often take much longer than evaluation at good points.

There are several variations on the PSO method that may be employed. Communication may be limited so that particles can only exchange best positions with their neighbouring particles. The swarm may be broken up into subswarms, each with fitness functions targeting components of the final solution. The best positions of each of the subswarms is then shared with the total swarm. Aspects of genetic algorithms can also be including in the PSO, using techniques such as selection and breeding to increase the impact of the top performing members of the swarm. Each of these modifications is particularly suited to a specific applications and can perform poorly in others so it is important to evaluate their implementation in the context of the system the PSO is to be applied to.

B.2.3 Genetic Algorithms

Genetic Algorithms (GAs) form part of a larger subset of computational methods known as Evolutionary Computing. They are based on the theory of evolution. Members of a population have a set of characteristics that are somehow measured to see how "fit" they are to survive. The "weak" members are removed from the population. The most fit members of the population survive and produce offspring. The offspring possess characteristics that are a combination of the characteristics of the previous generation. Some of these offspring should then be even more fit then the generation before. Mutations are also allowed to occur to introduce some random variability so that other characteristic possibilities are explored and the population does not simply converge to a non-optimum state.

In the computational implementation, like in the PSO algorithm, the solution space is randomly populated by *individuals*, whose characteristics correspond to possible values of the variables in the system. A *fitness function* is employed to evaluate the survival strength of the individuals. This fitness function is usually the function to be optimised. A *selection* operator is used to select a portion of the population that will survive to the next *generation*. A *reproduction* operator is used create new individuals using the characteristics of the surviving individuals. A *mutation* operator is used to introduce random changes to selected individuals in the population. A *driver* routine is used to iteratively perform the operations of evaluation, selection, reproduction and mutation until an acceptably optimised individual is found.

The following algorithm for implementation of a general genetic algorithm is taken from [77]

1. Let $g = 0$ be the generation counter
2. Initialise a population C_g of N individuals.
3. While no convergence
   (a) Evaluate the fitness of each individual in population C_g
   (b) Perform Cross-over
      i. Select two individuals $C_{g,n1}$ and $C_{g,n2}$
      ii. Produce offspring for $C_{g,n1}$ and $C_{g,n2}$
   (c) Perform Mutation
      i. Select one individual $C_{g,n}$
      ii. Mutate $C_{g,n}$
   (d) Select the new generation
   (e) Evolve the next generation: let $g = g + 1$

Convergence is reached when, for example,

- the maximum number of generations is exceeded
- an acceptable best fit individual has evolved
- the average and/or maximum fitness value do not change significantly over the past g generations

This is the basic algorithm for genetic algorithms. Choices in the selection, reproduction and mutation operators as well the actual fitness function used, can greatly change the speed, stability and ability of the algorithm to explore the solution space. The possible operators that can be applied are thus a topic of continual research. Genetic algorithms have found application in a variety of fields such as planning, control systems, regression and reduction of chemical kinetic mechanisms.

Below are listed some thoughts and questions as to how a genetic algorithm should be implemented for a particular application.

Initial Population

The size of the population to be used is an important decision in terms of the speed and accuracy of the method. A large population will cover more of the solution space and so will likely converge on an optimal solution in fewer generations than a smaller population. However the computational time for each generation for larger population will be longer than for a smaller population. Additionally, if some insight into the problem is available, the initial positioning can be influenced to focus the search on an area of the solution space where the optimum is known to be found.

Selection Operators

There are multiple decisions that must be made by the selection. How many individual must be selected? Should the selection be random, composed of only the fittest individual or a combination? Should a few weaker individuals be purposefully selected to add variety to the gene pool? Do individuals have a limit to how many generations they can survive for? These decisions may be constant throughout the computation, they may change via a predetermined schedule, or they may be adapted on the fly by considering aspects such as the overall fitness of the population and disparity between strong and weak members.

Reproduction Operators

Again there are several choices that can be made. How many offspring should be produced? Which *parents* should be combined to produce each *child*? How many *parents* should each child have? How will the characteristics of each of the parents be combined?

Mutation Operators

How often should mutations occur? How many individuals should undergo mutation? How should mutated individuals be selected? Should strong members be protected from mutation? Should all characteristics or some undergo mutation? How large a deviation is a mutation allowed to be?

B.3 Solution of Ordinary Differential Equations

A Differential Equation (DE) is an equation involving a function and its derivatives. If the function is dependent on multiple variables and and the equation is expressed using partial derivatives, this is known as a Partial Differential Equation (PDE). If the function is dependent on a single variable and the derivatives are all with respect to this variable then the equation is known as an Ordinary Differential Equation (ODE). This section will describe the solution of ODEs as these were the systems of equations encountered in implementation of the multi-zone model.

In modelling a system, the function argument is usually some sort of progress variable such as time. The ODE thus represents how the function changes with respect to this progress variable at each point. In an engine, for example, there will be various system properties such as temperature, pressure and species concentration that change in time. For N such properties, this can be represented by a system of equations having the general form

$$\frac{dx_i(t)}{dt} = f_i(t, x_1, x_2, \ldots, x_N), \qquad i = 1, \ldots, N \tag{B.29}$$

where each of the x_i are the properties that vary with time t.

In order to fix the solution of these equations, boundary conditions are required. Most commonly, the boundary conditions that are known are values of each of the functions at some initial point t_0. Such a situation is known as an initial value problem and solution of the system amounts to integration of the equations in B.29 to yield

$$x_i(t) = x_i(t_0) + \int_{t_0}^{t} f_i(t, x_1, x_2, \ldots, y_N)dt, \qquad i = 1, \ldots, N \tag{B.30}$$

Computational integration of the equations in B.30 usually involves breaking the interval of integration into smaller intervals or *timesteps*, over which the functions can be steadily advanced using the derivative information.

B.3.1 Integration Methods

For ease of explanation, integration of a single function will be described for each of the methods below. This can easily be extended to solution of a system of multiple equations by simply following the same procedure for each function at each timestep.

Euler Integration

The simplest method of performing such a numerical integration is to use the first order approximation

$$x_{n+1} = x_n + hf(t_n, x_n) \tag{B.31}$$

where n is the index referring to the current timestep
h is the size of the step taken given by $h = t_{n+1} - t_n$

This is known as Euler's Method. Because the method only uses the derivative information on one side of the integration interval at each step, the results may not be very accurate. This requires very small timesteps to be taken in order to obtain the same accuracy as other methods. The increased number of function evaluations required at each of the additional timesteps could potentially make Euler integration more computationally expensive than more complicated methods. Furthermore, in applications where the error accumulates with the number of timesteps, taking smaller timesteps may lead to less accurate solutions.

Euler integration is however relatively straightforward to implement. Additionally for the particular application required for this study, the integrating of reaction rates in a chemical kinetic mechanism (the FGAM), results in a particularly stiff set of ODEs. The concept of *stiff* systems is discussed in Section B.3.3 below but it suffices to say that appropriate treatment of such systems requires complicated *implicit* integration schemes that would have been challenging to integrate with the rest of the multi-zone model. Taking small enough Euler timesteps could ensure that the system could not jump into a region in which it was not defined and thus break down. The use of Euler integration in this implementation of the FGAM was a thus a conscious decision to sacrifice speed and possibly accuracy to ensure stability and integration.

Runge-Kutta Method

The Runge-Kutta Method is possibly the most widely used ODE integration method as it is a fairly simple algorithm that performs reasonably well with respect to speed and accuracy. The basic method involves taking several "trial" steps and using the derivative information at the end points of each of these trial to better approximate the gradient to be used for the actual step.

The formula for implementation of the popular fourth-order Runge-Kutta method (RK4) is given in B.32 below.

$$
\begin{aligned}
k_1 &= hf(t_n, x_n) \\
k_2 &= hf(t_n + \frac{h}{2}, x_n + \frac{k_1}{2}) \\
k_3 &= hf(t_n + \frac{h}{2}, x_n + \frac{k_2}{2}) \\
k_2 &= hf(t_n + h, x_n + k_3) \\
x_{n+1} &= x_n + \frac{k_1}{6} + \frac{k_2}{3} + \frac{k_3}{3} + \frac{k_4}{6}
\end{aligned} \tag{B.32}
$$

As implied by the name, the RK4 method is *fourth order accurate*. This means that it will solve exactly for a function that can be completely defined by a fourth order polynomial. This is in general better better than the first order accuracy of the Euler method, allowing much larger timesteps to be taken. However like the Euler method, the maximum stepsize is limited by the stiffness of the system set up by the FGAM. Thus, although use of RK4 would have resulted in slightly more accurate results, it would have been significantly slower due to the larger number of function evaluations required per step.

Implicit Methods

The two methods described above are called *explicit* as each of the steps can be performed sequentially, and although the derivative value at the next step may be approximated and used to improve the solution, the actual value is not required in the calculation.

Another class of methods, termed *implicit*, does include the derivative at the end point of each step in the calculation of that step. The simplest such example is the Backward Euler scheme. Here each step is given by the formula

$$x_{n+1} = x_n + hf(t_{n+1}, x_{n+1}) \tag{B.33}$$

Such a formulation is inherently stable (if not absolutely accurate) due to use of the "future" derivative to progress the function forward in time. Unfortunately, solution of the set of these equations for each time step requires that they all be solved simultaneously, unlike the explicit schemes in which they can be solved sequentially.

If the implicitly formulated ODE system is to be coupled with some other system that is explicitly formulated, then some mechanism must be introduced to enable their interaction. The explicit scheme cannot continue its sequential calculations without the information from the implicit scheme. Similarly the implicit scheme must possess the information from the explicit scheme at all timesteps before it can be solved. Thus an implicit ODE solver for the FGAM would be impractical to incorporate into the explicitly formulated multi-zone model.

B.3.2 Adaptive Time Stepping

The implementation of any ODE integration method can be significantly improved by use of an adaptive timestep method (in fact it is a requirement of some methods). In regions where the derivatives change significantly with changes in the progress variable, smaller timesteps should be in order to respond adequately to these changes. Likewise, in regions where the derivatives do not change much, larger timesteps may be taken, reaping large speed benefits.

The calculation of appropriate size timestep to be taken is usually accomplished by attempting a step, approximating the error in that step and then retaking an appropriately sized step to bring the approximate error in line with some predetermined allowance.

In the RK4 method, an approximation of the error can be made through *step doubling*. Here each step is taken twice: once as a full step and again as two half steps. Knowing that the method is fourth order accurate enables an approximation of the error to be made based on the difference between the results of the two stepping strategies.

If x_1 is the result of taking a single step and x_2 the result of taking two half steps, then the stepsize that will actually be taken h' can be rescaled from the original stepsize h by the formula

$$h' = h\left(\frac{|x_1 - x_2|}{\epsilon}\right)^{0.2} \tag{B.34}$$

where ϵ is the allowable error. The step doubling strategy of adaptive time stepping can be similarly utilised for other integration methods if their order of accuracy is also known.

For the Euler integration implementation of the FGAM in this study, the step size to be used at each timestep was determined to be the minimum of:

1. a predetermined default step size h_{def}
2. the maximum step size h that could be taken such that

$$-h\left(\frac{d[X_i]}{dt}\right) \leq [X_i] \tag{B.35}$$

for all species X_i to ensure that none of the species concentrations could become negative, causing the system to fail.

B.3.3 Stiff Systems of Equations

The term *stiff* is often used in general terms to describe differential equations that are "difficult" to solve numerically. More precise definitions are not easily formulated, as a

variety of aspects may contribute to the exhibited stiffness. Two such aspects leading to equation stiffness are especially relevant to reaction rate systems as encountered in the implementation of the FGAM.

The first aspect involves derivatives that are strongly dependent on the function value. Small errors in solution at a point, result in a slight error in calculation of the function at the current timestep. The derivative at this point thus also experiences an error in calculation, resulting in an even larger error in the function evaluation at the next timestep. The overall function thus constructed may deviate greatly from the actual function or experience large fluctuations in value.

In the simple reaction system

$$X_1 \rightarrow X_2 \tag{B.36}$$

the differential equation governing the concentration of X_1 is given by

$$\frac{d[X_1]}{dt} = -k[X_1] \tag{B.37}$$

for some reaction rate constant $k \geq 0$. This is a prime example of such a stiffness problem. Stability can be improved by the use of small timesteps but this results in a very long computation time.

The other stiffness cause which is much more difficult to cure involves the interaction of two timescales of very different magnitude. To illustrate this, consider the 2-reaction scheme

$$X_1 \rightarrow X_2 \rightarrow X_3 \tag{B.38}$$

The governing set of differential equations is given by

$$\frac{d[X_1]}{dt} = -k_1[X_1] \tag{B.39}$$

$$\frac{d[X_2]}{dt} = k_1[X_1] - k_2[X_2] \tag{B.40}$$

$$\frac{d[X_3]}{dt} = k_2[X_2] \tag{B.41}$$

Such a system is usually solved analytically through a steady state approximation. Assuming the concentration of X_2 is nominally constant and so $\frac{d[X_2]}{dt} = 0$. Then from B.40

$$[X_2] = \frac{k_1}{k_2}[X_1] \tag{B.42}$$

This can be substituted into Equation B.41 to obtain

$$\frac{d[X_3]}{dt} = \frac{k_1}{k_2}[X_1] = k_1[X_1] \tag{B.43}$$

and the concentration of X_2 can be explicitly calculated from B.42.

For the initial conditions

$$\begin{aligned}[X_1] &= 10 \\ [X_2] &= 0 \\ [X_3] &= 0\end{aligned} \tag{B.44}$$

and reaction rates given by

$$\begin{aligned}k_1 &= 1 \\ k_2 &= 10000\end{aligned} \tag{B.45}$$

this yields the analytical solution

$$\begin{aligned}[X_1] &= 10e^{-t} \\ [X_2] &= 0.001e^{-t} \\ [X_3] &= 10(1 - e^{-t})\end{aligned} \tag{B.46}$$

with concentrations progressing in time as per Figure B.3

However, if the system had to be numerically integrated using Euler integration for example, difficulties would be encountered. Suppose for example an initial step of size 0.001 was taken. Then the concentrations after 1 timestep would be $[X_1] = 9.99, [X_2] = 0.01, [X_3] = 0$. With these values, the rate of change of X_2 is now equal to 90.1, so the maximum step size that can be taken without the concentration of $[X_2]$ becoming negative is 0.0001. Choosing a smaller step size would also not help, as the next step size requirement would simply be even smaller.

Further such steps, switching between large and small, can be taken and the overall behaviour of X_1 and X_3 should be similar to that seen in Figure B.3, however the concentration of X_2 would oscillate violently. If X_2 is involved in any other reactions, the system may become completely unstable.

The appropriate course of action for dealing with stiff systems such as this is to use an *implicit* integration method. By solving for all of the timesteps simultaneously, the overall behaviour of the system is targeted and the local misbehaviour of the individual timesteps

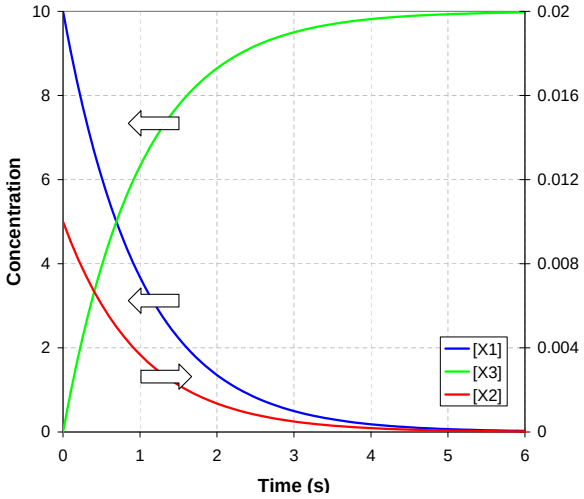

Figure B.3: *Behaviour of reaction system given in B.38. Concentrations of X_1 and X_3 shown on left axis. Concentration of X_2 shown on right axis.*

can be avoided. As described previously though, incorporating an implicitly formulation submodel into a larger model that is explicitly formulated is not a trivial exercise.

One option would be to formulate the entire multi-zone model using an implicit scheme as well. This is possibly an approach that should be adopted if the the model is to be repurposed from an investigative model to a predictive model, where accuracy is more important than simulation time. For this investigative study though, explicit schemes were used throughout.

Appendix C

Class Descriptions for Engine Model

C.1 Structure of the Multi-zone Model

The multi-zone model was implemented in VBA for Excel using a modular object oriented approach. A key objective in this implementation was to allow ease of incorporation of new and better methods and submodels into the larger multi-zone model. Different object classes were thus created to represent the different engine components and submodels that were required. Figure C.1 shows how the different object classes all fit together.

Each of these object classes consisted of several *members*, being either *variables*, *properties* or *methods*. A variable contains either a scalar value or another object. A property is a function that accepts input parameters and outputs either a scalar value or another object. A method is a subroutine that performs some action. Methods can also return values and objects.

In addition each member can be either *public* or *private*. Public members are accessible by the user and other objects. Private members can only be accessed by the object itself. The inputs and outputs of the public members thus form the *interface* through which objects can be pieced together and manipulated.

In this Appendix, the interface consisting of the public members of each of the classes used are presented using the syntax of VBA. What actually happens within these functions, as well as in the private functions, may change as a result of the particular methods and submodels used. However as long as the interface is maintained the same, the multi-zone model will continue to function. The interface can thus be seen as the master plan for implementing the multi-zone model.

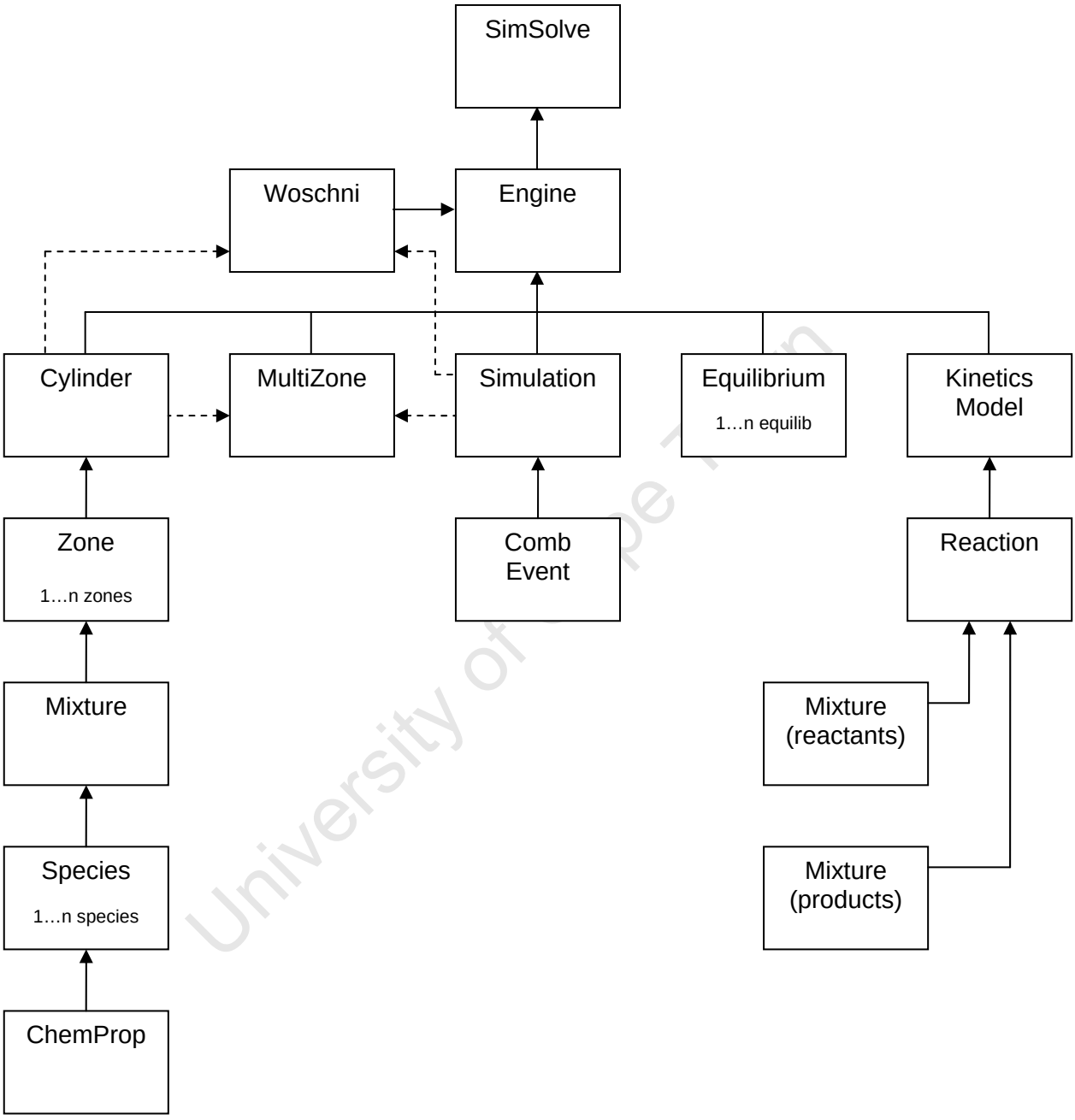

Figure C.1: *Object interactions in the multi-zone model. Solid lines indicate that the* from *object is* ***contained in*** *the* to *object. Dashed lines indicate that the* from *object is* ***referenced by*** *the* to *object.*

C.2 ChemProp Class

Description

Class containing the chemical properties for a specific chemical species

Constructor

```
Private Sub Class_Initialize(pname As String, pformula As String,
  pMM As Double, pdensity As Double, patoms() As Double, pCpTabL() As Double,
  pCpTabH() As Double, phf0L As Double, phf0H As Double, phrefL As Double,
  phrefH As Double, psrefL As Double, psrefH As Double, pTcross As Double)
'
' where  pname  is the name of the chemical property set
'        pformula  is the chemical formula
'        pMM  is the molecular mass
'        pdensity  is the density
'        patoms  contains the number of atoms of C, H, O and N
'        pCpTabL  contains the array of Cp coefficients for the lower
'                    temperature range
'        pCpTabH  contains the array of Cp coefficients for the higher
'                    temperature range
'        phf0L  is the hf0 value for the lower temperature range
'        phf0H  is the hf0 value for the higher temperature range
'        phrefL  is the href value for the lower temperature range
'        phrefH  is the href value for the higher temperature range
'        psrefL  is the sref value for the lower temperature range
'        psrefH  is the sref value for the higher temperature range
'        pTcross  is the crossover temperature between high and low ranges
```

Public Properties

```
Public Property Get atoms(index As Variant) As Double
'  returns the number of atoms of index: 1 = C, 2 = H, 3 = O, 4 = N

Public Property Get h(T As Double, Optional unit As String = "kJ/kmol")
  As Double
' returns total enthalpy h at temperature T in unit
' unit can be "kJ/kmol" or "kJ/kg"

Public Property Get s(T As Double, Optional unit As String = "kJ/kmol")
  As Double
' returns total entropy s at temperature T in unit
' unit can be "kJ/kmol" or "kJ/kg"
```

```
Public Property Get u(T As Double, Optional unit As String = "kJ/kmol")
  As Double
' returns total internal energy u at temperature T in unit
' unit can be "kJ/kmol" or "kJ/kg"

Public Property Get g(T As Double, Optional unit As String = "kJ/kmol")
  As Double
' returns total gibbs function g at temperature T in unit
' unit can be "kJ/kmol" or "kJ/kg"

Public Property Get cp(T As Double, Optional unit As String = "kJ/kmol")
  As Double
' returns specific heat Cp at temperature T in unit
' unit can be "kJ/kmol" or "kJ/kg"

Public Property Get cv(T As Double, Optional unit As String = "kJ/kmol")
  As Double
' returns specific heat Cv at temperature T in unit
' unit can be "kJ/kmol" or "kJ/kg"
```

C.3 CombEvent Class

Description

Class to describe of normal combustion through flame propagation

Constructor

```
Private Sub Class_Initialize(pthetaspark As Double, pdthetaburn As Double,
  pWiebeA As Double, pWiebeB As Double)
'
' where  pthetaspark  is the spark timing
'        pdthetaburn  is the burn duration
'        pWiebeA  is the Wiebe A coefficient
'        pWiebeM  is the Wiebe M coefficient
```

Public Properties

```
Public Property Get burnfrac(theta As Double) As Double
' returns the mass fraction burned at crank angle theta
```

C.4 Cylinder Class

Description

Class describing the piston motion in the engine cylinder

Constructor

```
Private Sub Class_Initialize(pBore As Double, pStroke As Double,
  pConCrankRatio As Double, pCompRatio As Double, pnuz As Integer)
'
' where  pBore  is the cylinder bore
'        pStroke  is the cylinder stroke
'        pConCrankRation  is the conrod to crank ratio
'        pCompRatio  is the cylinder compression ratio
'        pnuz  is the number of zones in the cylinder
```

Public Variables

```
Public zones As Collection
' A collection of each of the Zone objects in the cylinder
```

Public Properties

```
Public Property Get v(ByVal theta As Double) As Double
' returns cylinder volume at crank angle theta

Public Property Get volbal() As Double
' returns the residual of a cylinder volume balance of all zones
```

C.5 Engine Class

Description

Class to represent the engine, containing all other engine component and simulation objects.

Constructor

```
Private Sub Class_Initialize()
'
' As Engine is the overall container class it is convenient to simply create
'   the object first and then assign member objects and variables later
```

Public Variables

```
Public cyl As Cylinder
' The engine Cylinder object

Public sim As Simulation
' The Simulation object controlling simulation parameters

Public mzone As MultiZone
' The MultiZone object controlling interaction between zones

Public kinmodel As KineticsModel
' The kinetics model used to model autoignition in the unburned zones

Public disseqs As Collection
' A collection of Equilibrium objects describing dissociation reactions

Public wosch As Woschni
' The Woschni heat transfer model

Public atm As zone
' A Zone object simulating ambient conditions
```

Public Methods

```
Public Sub masstrans(fromZone As Zone, toZone As Zone, dm As Double,
  Optional mix As Boolean = False)
' transfers a mass of dm from fromZone to toZone including energy transfer
' if mix is False then the species are converted into the contents of the
'   toZone
' if mix is True then the species are not converted and transferred as is
```

C.6 Equilibrium Class

Description

Class to handle dissociation equilibrium reactions

Constructor

```
Private Sub Class_Initialize(preactants As Mixture, pproducts As mixture)
'
' where  preactants  is a mixture representing the LHS of the equilibrium
'        pproducts  is a mixture representing the RHS of the equilibrium
```

Public Properties

```
Public Property Get Gstar(pzone As Zone) As Double
' returns the G* value for the Zone pzone wrt the current equilibrium

Public Property Get kp(pzone As Zone) As Double
' returns the Kp vale of the Zone pzone wrt the current equilibrium

Public Property Get dissbal(pzone As Zone) As Double
' returns the residual of a dissociation Kp balance wrt the current
' equilibrium
```

C.7 KineticsModel Class

Description

Class to perform chemical kinetics calculations for autoignition modelling

Constructor

```
Private Sub Class_Initialize()
'
' reactions are added to the kinetics model after the object is created
```

Public Variables

```
Public reactions As Collection
' a collection of Reaction objects making up the chemical kinetics mechanism
```

Public Methods

```
Public Function takeRxnStep(pzone As zone, dt As Double) As Double
' attempts to take a chemical reaction timestep of lenght dt in Zone pzone
' the actual timestep taken may be greater or less than dt due to adaptive
'   timesteping
' the actual timestep taken is returned
```

C.8 Matrix Class

Description

Class for handling matrix objects and operations

Constructor

```
Private Sub Class_Initialize(prows As Integer, pcols As integer)
'
' initialises a matrix with prows rows and pcols columns
```

Public Properties

```
Public Property Get mat(ByVal i As Integer, ByVal j As Integer) As Double
' returns the entry in row i, column j

Public Property Let mat(ByVal i As Integer, ByVal j As Integer,
  value As Double)
' inserts value in row i, column j

Public Property Get rows() As Integer
' returns the number of rows in the matrix

Public Property Let rows(value As Integer)
' sets the number of rows in the matrix

Public Property Get cols() As Integer
' returns the number of columns in the matrix

Public Property Let cols(value As Integer)
' sets the number of columns in the matrix

Public Property Get inverse() As Matrix
' returns the inverse of the matrix

Public Property Get row(ByVal index As Integer) As Matrix
' return row number index of the matrix

Public Property Get col(ByVal index As Integer) As Matrix
' returns column number index of the matrix

Public Property Get L1norm() As Double
' returns the L1 norm of the matrix

Public Property Get L2norm() As Double
' returns the L2 norm of the matrix

Public Property Get Linfnorm() As Double
```

```
' returns the Linfinity norm of the matrix
```

Public Methods

```
Public Sub dimension(i As Integer, Optional j As Integer = 1)
' redimensions the matrix to have i rows and j columns

Public Function copy() As Matrix
' returns a new matrix object that is a copy of the matrix

Public Function ludcmp(ByRef index As Matrix, ByRef d As Double)
  As Matrix
' performs an LU decomposition of the matrix returning a matrix containing
'   both lower and upper triangular parts
' index returns a vector describing the row permutations resulting from
'   partial pivoting
' d returns +1 or -1 depending on whether the number of row interchanges was
'   even or odd respectively

Public Function lubksb(ByRef b As Matrix, ByRef index As Matrix) As Matrix
' performs backsubstitution to solve the system Ax = b
' index is the row permuation vector created by ludcmp

Public Function invmult(ByRef b As Matrix) As Matrix
' return the product of the inverse of the matrix and the vector b
```

C.9 Mixture Class

Description

Class to represent a mixture of different species

Constructor

```
Private Sub Class_Initialize(pname As String)
'
' where  pname  is the name of the mixture
' species are added to the mixture after creation of the object
```

Public Variables

```
Public specs As Collection
' a collection of the Species objects that make up the mixture
```

Public Properties

```
Public Property Get name() As String
' returns the name of the mixture

Public Property Get atoms(index As Variant) As Double
' returns the number of atoms of index in the mixture
' C = 1, H = 2, O = 3, N = 4

Public Property Get ns() As Integer
' returns the number of species in the mixture

Public Property Get dXdt(index As Variant) As Double
' returns the current rate of change of concentration of species index

Public Property Let dXdt(index As Variant, value As Double)
' sets the current rate of change of concentration of species index to
'   value

Public Property Get molfrac(index As Variant) As Double
' returns the mol fraction of species index in the mixture

Public Property Get ntot() As Double
' returns the total number of mols in the mixture

Public Property Get MM() As Double
' returns the molar mass of the mixture

Public Function h(T As Double, Optional unit As String = "kJ/kg") As Double
' returns the total enthalpy of the mixture at temperature T in unit
' unit can be "kJ/kg" or "kJ/kmol"

Public Function s(T As Double, Optional unit As String = "kJ/kg") As Double
' returns the total entropy of the mixture at temperature T in unit
' unit can be "kJ/kg" or "kJ/kmol"

Public Function u(T As Double, Optional unit As String = "kJ/kg") As Double
' returns the total internal energy of the mixture at temperature T in unit
' unit can be "kJ/kg" or "kJ/kmol"

Public Function cp(T As Double, Optional unit As String = "kJ/kgK") As Double
' returns the Cp value of the mixture at temperature T in unit
' unit can be "kJ/kgK" or "kJ/kmolK"
```

```
Public Function cv(T As Double, Optional unit As String = "kJ/kgK") As Double
' returns the Cv value of the mixture at temperature T in unit
' unit can be "kJ/kg" or "kJ/kmol"

Public Function r(Optional unit As String = "kJ/kgK") As Double
' returns the Gas Constant of the mixture in unit
' unit can be "kJ/kgK" or "kJ/kmolK"

Public Function gamma(T As Double) As Double
' returns the specific heat ratio of the mixture at temperature T

Public Function v(p As Double, m As Double, T As Double) As Double
' returns the volume of the mixture at pressure p, mass m and temperature T

Public Function p(v As Double, m As Double, T As Double) As Double
' returns the pressure of the mixture at volume v, mass m and temperature T

Public Function T(p As Double, v As Double, m As Double) As Double
' returns the temperature of the mixture at pressure p, volume v and mass m

Public Function m(p As Double, v As Double, T As Double) As Double
' returns the mass of the mixture at a pressure p, volume v and temperature T

Public Function rho(p As Double, T As Double) As Double
' returns the density of the mixture at a pressure p and temperature T

Public Function TfromU(useek As Double, Optional T0 As Double = 1000)
  As Double
' returns the temperature at an internal energy useek using an initial guess '   T0
```

Public Methods

```
Public Function copy() As Mixture
' returns a Mixture object that is an exact copy of the mixture
```

C.10 MultiZone Class

Description

Class to handle the interaction of the multiple zones.

Constructor

```
Private Sub Class_Initialize(ByRef pcyl As Cylinder, Byref psim
  As Simulation)
'
' creates references to the engine's Cylinder and Simulation objects
```

Public Properties

```
Public Property Get muzone(index As Integer) As Double
' returns the mass in unburned zone no. index after current burn step

Public Property Get massforbl(bl As Double) As Double
' returns the total mass consumed by the flame for a given burn length bl

Public Property Get blfrombm(bm As Double) As Double
'returns the burn length that would correspond to a total mass consumed bm
```

Public Methods

```
Public Sub setref()
' sets the initial volumes of each of the unburned zone according to the
'   the initial geometric zone configuration
```

C.11 `Reaction` Class

Description

Class to represent a single reaction in a chemical kinetics mechanism

Constructor

```
Private Sub Class_Initialize(pname As String, ByRef reactants As Mixture,
  ByRef products As Mixture, ByRef pA As Matrix, ByRef pB As Matrix,
  ByRef pPn As Matrix, ByRef prpowr As Matrix, ByRef prpowp As Matrix,
  pnk As Integer)
'
' where  pname  is the name of the reaction
'        preactants  is a mixture representing the LHS of the reaction
'        pproducts  is a mixture representing the RHS of the reaction
'        pA  is a vector containing reaction rate A coefficients
'        pB  is a vector containing reaction rate B coefficients
'        pPn  is a vector containing reaction rate np coefficients
'        prpowr  is a matrix containing reactant concentration powers
```

```
'        prpowp  is a matrix containing product concentration powers
'        pnk  is the number of Arrhenius forms that make up the reaction rate
'
' the initialisation has been set up using vectors and matrices to store the
'   reaction rate coefficients in order to cater for the 1st FGAM reaction
'   which uses a QSSA to derive a reaction rate composed of two Arrhenius
'   expressions
```

Public Properties

```
Public Property Get name() As String
' returns the name of the reaction

Public Property Get rate(pzone As zone) As Double
' returns the current reaction rate in the Zone pzone
```

C.12 SimSolver Class

Description

Primary Class containing the Engine object. Solves the system at each timestep by setting up the vector of balance functions F and the Jocobian J and iteratively solving $\mathbf{x}_{i+1} = \mathbf{x}_i + \mathbf{J} \cdot (-\mathbf{f})$.

Constructor

```
Private Sub Class_Initialize()
'
' engine object added after object creation
```

Public Variables

```
Public eng As Engine
' the main engine object containing all other component and simulation
'   objects
```

Public Methods

```
Public Sub solvestep()
' sets up the balance equations and solves at current timestep
```

C.13 `Simulation` Class

Description

Class containing all the simulation parameters and information

Constructor

```
Private Sub Class_Initialize()
'
' all variables are public so none need to be initialised on creation
' this class is used solely for data storage
```

Public Variables

```
Public thetaStart As Double
' crank angle at which to start simulation

Public thetaEnd As Double
' crank angle at which to end simulation

Public timesteps As Integer
' total number of timesteps to be used

Public speed As Double
' engine speed

Public p0 As Double
' initial pressure

Public T0 As Double
' initial temperature

Public stepnow As Integer
' current timestep

Public tnow As Double
' current time

Public thetanow As Double
' current crank angle

Public combustion As CombEvent
' CombEvent object to describe normal combustion through flame propagation
```

```
Public AIdetected As Boolean
' flag to indicate autoignition has occurred

Public combFlag As Boolean
' flag to switch normal combustion on and off

Public qFlag As Boolean
' flag to switch heat transfer on and off

Public dissflag As Boolean
' flag to switch dissociation on and off

Public AIflag As Boolean
' flag to switch autoignition modelling on and off
```

C.14 Species Class

Description

Class to represent individual chemical species

Constructor

```
Private Class_Initialize(pname As string, ByRef pchem As ChemProp)
'
' where  pname  is the name of the species
```

Public Variables

```
Public chem As ChemProp
' the chemical properties of the species

Public nmol As Double
' the total number of moles of the species

Public dXdt As Double
' the rate of change of concentration of the species
```

Public Properties

```
Public Property Get name() As String
' returns the name of the species
```

```
Public Property Get mass() As Double
' returns total mass of the species

Public Property Get h(T As Double, Optional unit As String = "kJ/kmol")
  As Double
' returns total enthalpy of the species at temperature T in unit

Public Property Get u(T As Double, Optional unit As String = "kJ/kmol")
  As Double
' returns total internal energy of the species at temperature T in unit

Public Property Get s(T As Double, Optional unit As String = "kJ/kmol")
  As Double
' returns total entropy of the species at temperature T in unit

Public Property Get g(T As Double, Optional unit As String = "kJ/kmol")
  As Double
' returns total gibbs function of the species at temperature T in unit

Public Property Get cp(T As Double, Optional unit As String = "kJ/kmolK")
  As Double
' returns Cp value of the species at temperature T in unit

Public Property Get cv(T As Double, Optional unit As String = "kJ/kmolK")
  As Double
' returns Cv value of the species at temperature T in unit

Public Property Get MM() As Double
' returns molar mass of the species
```


C.15 Woschni Class

Description

Class to handle heat transfer through Woschni correlation

Constructor

```
Private Sub Class Initialize(ByRef pcyl As Cylinder,
  ByRef psim As Simulation)
'
' creates references to the Cylinder and Simulation objects of the engine
```

```
' Woschni parameters are coded directly into the class
```

Public Properties

```
Public Property Get Qdot(pzone As zone) As Double
' returns the heat transfer rate of the Zone pzone
```

C.16 Zone Class

Description

Class to represent a single zone in the multi-zone model

Constructor

```
Private Sub Class_Initialize(pname As String, ByRef pmix As Mixture)
'
' where  pname  is the name of the zone
'        pmix  is the mixture contained in the zone
```

Public Variables

```
Public mix As Mixture
' the mixture contained in the zone

Public V1 As Double
' volume at the previous timestep

Public p1 As Double
' pressure at the previous timestep

Public T1 As Double
' temperature at the previous timestep

Public Q1 As Double
' heat transfer at the previous timestep

Public m1 As Double
' mass at the previous timestep

Public MM1 As Double
' molar mass at the previous timestep
```

```
Public h1 As Double
' enthalpy at the previous timestep

Public u1 As Double
' internal energy at the previous timestep

Public s1 As Double
' entropy at the previous timestep

Public nC1 As Double
' number of carbon atoms at the previous timestep

Public nH1 As Double
' number of hydrogen atoms at the previous timstep

Public nO1 As Double
' number of oxygen atoms at the previous timestep

Public nN1 As Double
' number of nitrogen atoms at the previous timestep

Public V2 As Double
' volume at the current timestep

Public p2 As Double
' pressure at the current timestep

Public T2 As Double
' temperature at the current timestep

Public Q2 As Double
' heat transer at the current timestep

Public m2 As Double
' mass at the current timestep

Public dmin As Double
' mass transfer into the zone

Public dmout As Double
' mass transfer out of the zone

Public dHin As Double
```

```
' enthalpy transfer into the zone

Public dHout As Double
' enthalpy tranfer out of the zone
```

Public Properties

```
Public Property Get ubal() As Double
' returns residual of energy balance

Public Property Get igbal() As Double
' returns residual of ideal gas law balance

Public Property Get massbal(atom As String) As Double
' returns residual of mass balance

Public Property Get ntot(Optional state As Integer = 2) As Double
' returns total number of moles in zone

Public Property Get u2() As Double
' returns current internal energy

Public Property Get h2() As Double
' returns current enthalpy

Public Property Get MM2() As Double
' returns current molar mass

Public Property Get s2() As Double
' returns current entropy

Public Property Get nC2() As Double
' returns current number of carbon atoms

Public Property Get nH2() As Double
' returns current number of hydrogen atoms

Public Property Get nO2() As Double
' returns current number of oxygen atoms

Public Property Get nN2() As Double
' returns current number of nitrogen atoms
```

```
Public Property Get nmol(index As Variant, Optional state As Integer = 2)
  As Double
' returns number of moles of species index
' state = 1 refers to previous timestep
' state = 2 refers to current timestep

Public Property Get atoms(index As Variant) As Double
' returns total number of atoms of index
' C = 1, H = 2, O = 3, N = 4

Public Property Get volcon(index As Variant) As Double
' returns volume concentration of species index
```

C.17 Other Modules

Apart from the classes described above, other modules containing global methods were also used and these are described below

Initialisation Module

```
Public Function newChemProp(chem As String) As ChemProp
' returns ChemProp object containing property set of chemical chem

Public Function newFuelChem(fuelMix As Mixture) As ChemProp
' returns ChemProp object containing property set of a fuel blend as per the
'   Mixture fuelMix

Public Function newAFMix(ByRef fuel As Species, phi As Double,
  Optional egr As Double = 0) As Mixture
' returns Mixture object containing an unburned Air-Fuel mixture with fuel,
'   equivalence ratio phi and residual exhaust gas egr

Public Function newCombustedMix(AFmix As Mixture) As Mixture
' returns Mixture object containing a mixture as per full combustion of AFmix
```

MatrixFuncs Module

```
Public Function add(mat1 As Matrix, mat2 As Matrix) As Matrix
' returns the sum mat1 + mat2

Public Function mult(mat1 As Matrix, mat2 As Matrix) As Matrix
' returns the matrix product mat1 x mat2
```

```
Public Function smult(mat1 As Matrix, scal As Double) As Matrix
' return the scalar matrix product scal x mat1
```

SimMod Module

```
Public Sub runSim()
' runs the simulation
' this is the primary routine run from the front end interface
' calls initialise, burn and writeline

Public Sub initialise(eng As Engine)
' sets up all initial parametes

Public Sub burn(eng As Engine, sol As SimSolver)
' steps through timesteps from simulation start to end

Public Sub writeline(eng As Engine)
' outputs to spreadsheet the current properties for each zone and other
'   simulation parameters for the current timestep
```

SAE International™

An Investigation of Cascading Autoignition and Octane Number using a Multi-zone Model of the CFR Engine

2011-01-0850
Published
04/12/2011

Marlan Perumal and Gareth Floweday
Sasol Advanced Fuels Laboratory

doi:10.4271/2011-01-0850

ABSTRACT

This paper describes a quasi-dimensional multi-zone model of the CFR engine. The engine cylinder was divided into multiple zones containing the unburned air-fuel mixture, which experienced different temperature-pressure histories during the compression stroke and flame propagation phases of the engine cycle. This allowed for the simulation of a temperature gradient within the cylinder, which is postulated to be the cause of the Cascading Autoignition characteristic of the CFR engine.

A Wiebe function description of the flame front propagation was used to describe the normal combustion process; mass and energy were transferred proportionally from the unburned zones to a single burned zone. A Functional Global Autoignition Model (FGAM) was used to describe the autoignition chemistry in each of the unburned zones and an equilibrium approach was used to determine the composition of the burned zone.

This multi-zone model successfully reproduced the non-instantaneous pressure rise seen in knocking CFR pressure traces. A parametric modelling study was then conducted to investigate the influence of inlet pressure, inlet temperature, residual exhaust gas fraction, burn duration, compression ratio and in-cylinder temperature distribution on the cascading autoignition.

Having been calibrated on knocking pressure traces of iso-Octane running under RON 100 test conditions, the model was applied on nine Primary Reference Fuels (PRFs) and a Toluene Standardization Fuel (TSF) under their respective Research Octane Number (RON) test conditions. For each of the fuels, the calibration constants of the FGAM were optimised to fit a comprehensive set of Constant Volume Autoignition simulations, generated by the CHEMKIN™ Chemical Kinetics Software, based on a well validated Detailed Kinetic Mechanism.

The combination of the computationally inexpensive FGAM that accurately reproduced cool flame heat release with a multi-zone engine model was shown to simulate the post-knock pressure development of a knocking pressure trace in the CFR engine, which the method of using a detailed kinetic model in a simple 2-zone engine model does not. An accurate description of this knock pressure development would enable a more representative simulation of knock intensity as measured in the Octane Rating tests.

INTRODUCTION

Octane rating is the measure of a fuel's resistance to knock in spark-ignition engines. Since knock is potentially very damaging to the engine, it is a key design constraint and operating parameter for engines on the one hand, and production specification for fuel refineries on the other. The ASTM specifications D2699 [1] and D2700 [2], for measuring Research Octane Number (RON) and Motor Octane Number (MON) respectively, make these measurements standard practice for typical gasolines and many gasoline components (the measurement of some alcohol components have proved problematic though [3]).

The operating conditions for the two Octane tests were initially fairly representative of the operating conditions likely to induce knock in early carburetted SI engines. With the advent of Port Fuel Injection, the real life operating conditions gravitated towards those of the RON test.

Kalghatgi [4] proposed an Octane Index measure (OI = RON − KS) where K is a constant typical of a given engine and operating condition and S is the sensitivity, (RON − MON). For $0 \leq K \leq 1$, this would result in a linear interpolation between RON and MON. Turbocharged and Direct Injection Spark Injection (DISI) engines (with higher operating pressures and lower temperatures) experience knock outside of the original RON/MON operating envelope [5]. Thus, as is more often the case, $K < 0$ for modern engines. This would require an extrapolation beyond the description space of RON and MON. In order to ensure that this extrapolation is indeed valid, it is extremely important to understand the underlying cause of fuel sensitivity. It was in search of this understanding that this study returned to the ON measuring process in order to understand what is actually being measured.

As a first step in this process, this work was concerned with replicating the unique pressure development seen in knocking CFR engine pressure traces, by using a multi-zone engine model that incorporated the recently developed Functional Global Autoignition Model (FGAM) [6]. This would allow for a better modelled description of Standard Knock Intensity (SKI), which is the metric used to assign Octane Number.

This paper begins with a description of the measurement of Octane number (ON) in the CFR engine and the unique way in which knock manifests under these conditions. The requirements of a model that would be able to describe this behaviour are then discussed with specific emphasis on the choice of the FGAM as the autoignition submodel. The implementation of the multi-zone model itself is then described with discussion of the various simplifications and assumptions made, as well as the calibration of the model to produce the desired pressure development behaviour. Then the results of a parametric study are presented, followed by the application of the model to simulate the RON test for various fuel blends. Finally the strengths and shortcomings of this modelling approach are discussed with a view to incorporating more accurate submodels and input parameters to produce a model capable of ON prediction.

MEASUREMENT OF OCTANE NUMBER

RON and MON both measure fuel knock resistance in the standard single cylinder, adjustable compression ratio, CFR engine under prescribed operating conditions. The CFR engine has a number of design features that make it slightly different to modern production engines. The first is a shrouded inlet valve. This shroud covers half the open valve area and directs flow away from the spark plug and around the cylinder, imparting a high degree of swirl on the in-cylinder flow [7]. The other noteworthy feature is a side-mounted sparkplug, which together with the slow engine speed and heated inlet, create conditions that are more likely to induce knock at lower compression ratios than standard production engines.

A series of papers by Swarts, Yates and co-workers [8, 9, 10, 11] explored the RON and MON tests in detail by analysing pressure traces of the CFR run under knocking and non-knocking test conditions. Two specific outcomes were important to take note of. The first was that knock manifests differently in the CFR than in standard production engines. In production engines, knock typically involves autoignition of about 5% of the endgas and this is followed by a near instantaneous pressure spike and pressure oscillations audible as the knock sound [13]. In the CFR engine, knock can involve between 30% and 70% of the endgas [9]. A distinct knock-point was observable as shown in Figure 1. This was the point at which the pressure rise rate increased significantly but not in the same instantaneous fashion as the shock wave caused by knock in conventional SI engines. This indicated an accelerated but still non-instantaneous heat release.

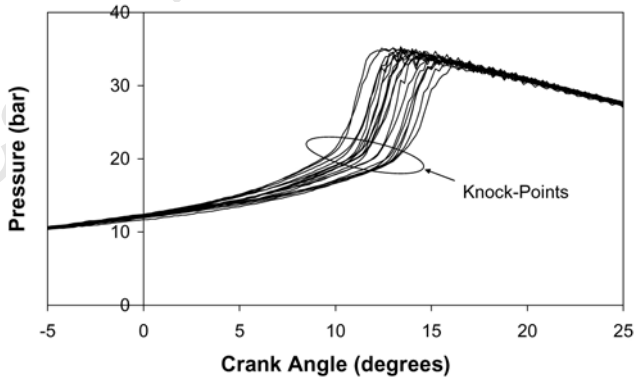

Figure 1. Several Pressure Traces showing the knock-points for PRF80 at SKI under RON conditions

The second important observation concerned the measurement of knock intensity by the knockmeter during Octane rating and specifically Standard Knock Intensity (SKI) [11]. The filtered rate of change of pressure signal is adjusted in magnitude and sensitivity by the METER and SPREAD dials on the knockmeter respectively, before being displayed as a knock intensity reading. This knockmeter reading was less affected by the high frequency pressure oscillations (as would be the case for knock sensors on modern engines [14]) but rather by the unique post knock-point pressure development. In order to model the MON and RON tests for the purpose of predicting octane number, this accelerated pressure development must also be simulated so that a better defined measure of actual SKI can be obtained.

Many current modelling approaches [15,16] used a detailed kinetic autoignition model in a single unburned zone to predict autoignition and then used a measure, such as 30% of unburned mass involved in autoignition, as a proxy for SKI.

Experimental work showed that mass fraction burned at the knock point varied significantly with ON. A graph of the mass fraction burned at knock-point for PRF blends under their respective RON test conditions is reproduced in Figure 2 [10]. It can be seen that as much as 70% of the unburned gas was involved in autoignition for a PRF40 at SKI. Thus using a fixed value of MFB as a proxy for SKI would not be sound assumption. Furthermore these single zone models produced a near-instantaneous pressure rise rate at the knock point [15], which is not consistent with actual knocking CFR pressure traces and so could not be used to simulate readings of knock intensity.

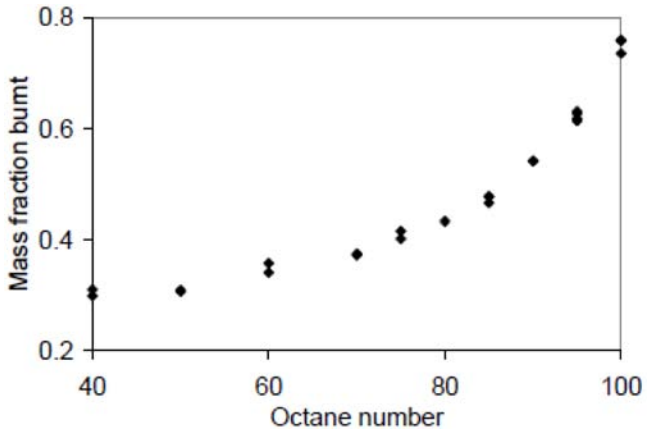

Figure 2. Mass Fraction Burned at Knock Point for PRF40 to PRF100 under RON test conditions [10]

CASCADING AUTOIGNITION

The unique pressure development in the knocking CFR engine had already been noted by Arrigoni et al. [17] in 1974 but surprisingly little work has been done since in attempting to model or explain it. Swarts et al. [18] proposed that it is due to a "cascading autoignition" similar to that seen in HCCI engines. This could be caused by a thermal gradient set up in the CFR engine by wall heating and in-cylinder fuel evaporation, and maintained by the slow engine speed and high swirl generated by the shrouded inlet valve.

A cascading autoignition event is defined as follows: A small portion of the endgas autoignites. The sudden increase in temperature and pressure compresses the adjacent end-gas, which was at a slightly lower temperature, and causes it to also autoignite. This in turn exerts a knock-on effect and autoignition cascades through the endgas faster than the propagating flame speed but still at subsonic velocities.

It is well acknowledged in the literature that knock in SI engines begins with the autoignition of kernels at thermal inhomogeneities [19,20]. However, due to the small mass fraction involved in the knock event and the smaller temperature gradient in the endgas, the pressure rise rate in a production engine due to knock is near instantaneous and does not show evidence of a cascading autoignition [21]. This partly explains why knock in standard production engines can be so damaging yet is tolerated as standard operating condition in the CFR engine.

In [18] a modelling approach was suggested using multiple unburned zones, each with a different severity of heat loss, to set up the required temperature gradient. It is also suggested that a cascading autoignition beginning near the walls and propagating towards the centre of the cylinder would produce the required pressure development. During the inlet process, the cylinder walls are hotter than the inlet gas and so heating of the gas near the walls could potentially set up such a gradient. It was the aim of the current work to use a similar modelling approach to reproduce the cascading autoignition phenomenon.

AUTOIGNITION MODELLING

The prediction of knock requires a model for the prediction of autoignition of the endgas. Detailed Chemical Kinetic Mechanisms (DKMs), involving thousands of reactions and species, are generally regarded as the most reliable and accurate autoignition models [22] and are commonly used in CFR engine models of the Octane tests such as [15,23]. They are however extremely computationally expensive, even when used in a single unburned zone. Considering the total number of simulations required for this study, the run time associated with such computational expense would not have been feasible.

Reduced or Lumped Mechanisms reduce the number of reactions and species in the system and can potentially provide a good fit of the overall ignition delay over a wide temperature and pressure domain [24]. Mechanisms reduced enough to be computationally efficient were however usually poor at predicting rates of heat release during autoignition, especially the cool flame heat release of "2-stage ignition" fuels [25].

Empirical models based on the Conservation of Autoignition Delay Integral are also currently used to predict autoignition. However even such models that took into account aspects such as cool flame timing and temperature rise [26] did not include predictions of heat release rates and so were unsuitable for the purpose of modelling the pressure rise rate of cascading autoignition

A reaction rate based Function Global Autoignition Model (FGAM) consisting of 9 reactions and 9 species has recently been developed with the specific aim of accurately capturing the heat release characteristics of a wide range of hydrocarbon fuels over varying operating conditions of temperature, pressure, air fuel ratios ($\phi <= 1$) and residual exhaust gas fraction. This model was able to achieve this by

allowing the coefficients that determine the reaction rates in the mechanism to be adjusted, for a given fuel, to match the autoignition characteristics of either detailed chemical kinetics simulations of that fuel or experimental data.

Since it has been proposed that the sensitivity of fuels can largely be attributed to the difference between single-stage and 2-stage autoignition behaviour [11,27], it was considered important to consider the heat release rates of these processes. The FGAM was used so that the complicated 2-stage autoignition heat release behaviour could be reproduced in a computationally efficient manner. The knock modelling study of [15] specifically did not consider the use of a multi-zone model to describe uneven temperature distribution because of the computational expense associated with their DKM. The use of the FGAM did allow for a multi-zone approach. Additionally the FGAM can potentially be fitted to real, full boiling range gasoline fuels, which is not yet possible with DKMs. The reaction mechanism of the FGAM is summarised in Appendix A and is more thoroughly described in [28].

The FGAM was fitted to the autoignition profile of a range of PRF Blends and a Toluene Standardization Fuel (TSF). These profiles were generated by the Lawrence Livermore National Laboratory (LLNL) developed detailed chemical kinetics autoignition mechanism described in [29], and run in CHEMKIN™ [18]. For each fuel, 100 constant volume simulations were performed at stoichiometric air-fuel ratio and 15% residual exhaust gas (REG) fraction, spanning initial pressures of 10 bar to 40 bar and initial temperatures of 600 K to 1200 K. The parameters of the FGAM were then optimized by a Particle Swarm Optimisation Method [30] to best match the temperature-time traces of the corresponding CHEMKIN runs.

An example of the overall autoignition delay fit for a PRF80 blend is shown in Figure 3. The average error in the overall ignition delay for this fit was 9%. The fitness function to be minimised for optimisation was the area between the temperature-time curves of the DKM and FGAM simulations, as per Eqn 1.

$$err = \frac{\int_{t=0}^{ID} \left| T_{DKM} - T_{FGAM} \right| dt}{T_{AI} \times ID} \qquad (1)$$

Where *err* is the error in fit, *t* is time, *ID* is overall ignition delay, T_{DKM} is the temperature predicted by the DKM, T_{FGAM} is the temperature predicted by the FGAM and T_{AI} is the temperature above which autoignition was assumed to be complete. T_{AI} was set to 1500K to provide balance between fitting overall ignition delay and cool flame behaviour.

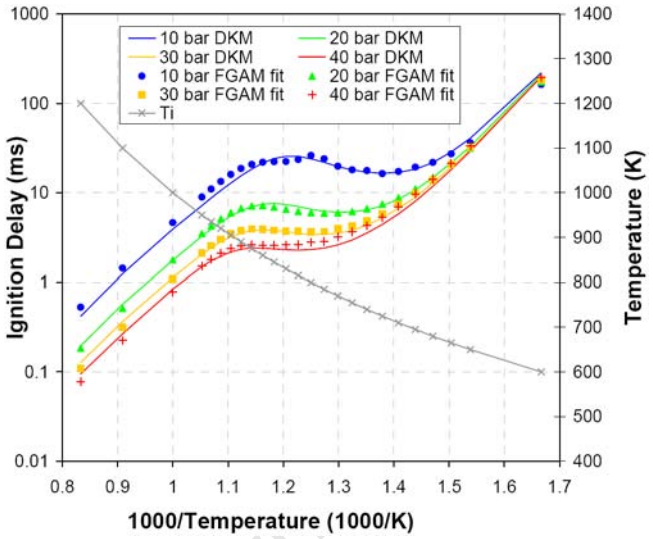

Figure 3. Overall Ignition Delay Fit of the FGAM to DKM simulations for PRF80 blend at ϕ = 1 and REG = 15%

In this way the overall ignition delay as well as the cool flame heat release could be targeted. Figure 4 shows examples of these temperature-time traces. This fit of the FGAM showed a slight under-prediction of the cool flame ignition delay and ceiling temperature and a slight over-prediction in post-cool flame ignition delay. However the overall trends for these parameters were directionally consistent. Floweday [25] notes that the differences between Detailed Kinetic Models can be as much as 38% in overall ignition delay so an overall fit of less than 10% may be regarded as quite acceptable.

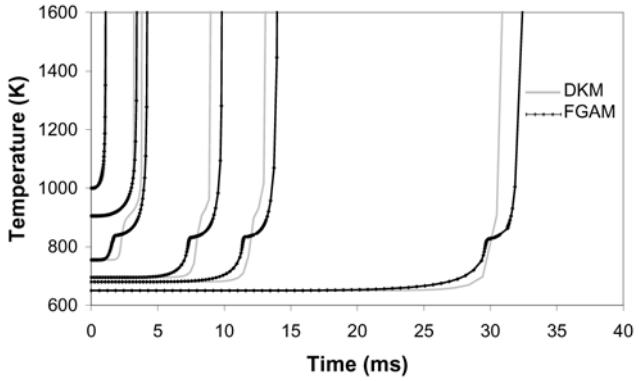

Figure 4. Examples of Temperature vs Time traces for PRF80 at 30bar and various initial temperatures showing FGAM fit to DKM simulations of overall ignition delay and cool flame behaviour

The FGAM calibration coefficients obtained in this study are provided in Appendix B. The average error in fit was between 6% and 12% for PRF blends and 15% for the TSF blend.

MULTI-ZONE ENGINE MODEL

The engine model used in this investigation was a multi-zone quasi-dimensional model that incorporated some of the traits of traditional 2- and 3-zone SI models [16] and thermally stratified multi-zone models used in the study of HCCI engines [31]. The multi-zone model was set up on a simple modular basis with various initial assumptions to show proof of concept in its implementation. The intention of this was to emulate the cascading autoignition seen in the CFR engine through the modelling of a temperature gradient within the engine cylinder.

The unburned gas in the cylinder was divided into multiple zones by volume. The division was done so as to nominally represent an annular distribution of zones within the cylinder (as shown schematically in Figure 5) but the zones themselves were zero-dimensional. The outer most zone represented a thermal boundary layer for purposes of heat transfer to the cylinder walls. The other zones were modelled as adiabatic, with no mass transfer between the unburned zones. These zones could then each be assigned unique initial temperatures to represent an initial thermal gradient at Inlet Valve Closure (IVC). It is proposed that such a thermally stratified annular distribution may be set up by the high degree of swirl in the CFR due to the shrouded inlet valve.

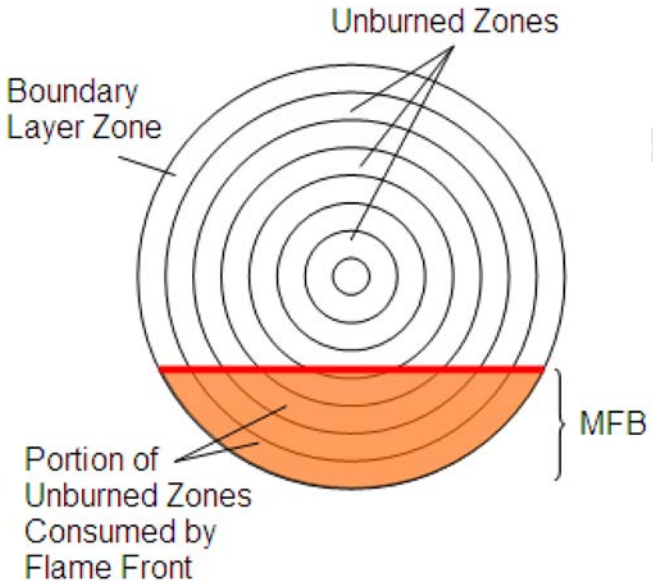

Figure 5. Schematic of concentric Unburned Zone reference layout showing linear consumption by the advancing flame front

The adiabatic zone assumption was adopted to simplify the simulation of the autoignition chemical reactions. Modelling any actual heat transfer that would occur in the turbulent cylinder environment would be extremely challenging in a quasi-dimensional model such as this. It is proposed instead that an adiabatic initial distribution can be found that results in the same temperature gradient at the point of knock, which would achieve the required result.

IMPLEMENTATION

The engine model was implemented as shown in the flowchart in Figure 6.

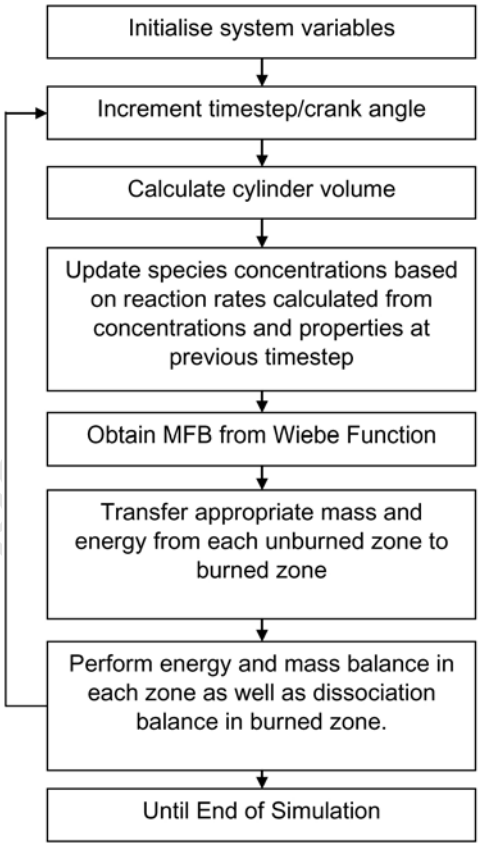

Figure 6. Simulation Algorithm of the Multi-zone CFR engine model

At each timestep the total volume of the cylinder was calculated from the formula [13]

$$\frac{V}{V_c} = 1 + \frac{1}{2}(r_c - 1)\left[R + 1 - \cos\theta - \sqrt{R^2 - \sin^2\theta}\right] \quad (2)$$

(where V is the instant cylinder volume, V_c is the clearance volume, r_c is the compression ratio, R is the conrod-crank ratio and θ is the current crank angle). For each zone i, an energy balance

$$Q - \left(\frac{p_{i,t} + p_{i,t-1}}{2}\right)\left(V_{i,t} - V_{i,t-1}\right) - \left(m_{i,t}u_{i,t} - m_{i,t-1}u_{i,t-1} + \delta m_{in}u_{in} - \delta m_{out}u_{i,t}\right) = 0 \quad (3)$$

(where Q is the heat transfer into the zone, p is the pressure, m is the mass, u is the internal energy, and δm is the mass transferred. The subscript i represents the property of that zone, t the current timestep, *in* transfer into the zone and *out* transfer out of the zone) and the ideal gas law equation:

$$p_{i,t}V_{i,t} - m_{i,t}R_{i,t}T_{i,t} = 0 \quad (4)$$

(where R is the mixture gas constant) were set up at each timestep t.

The zones were linked by setting the pressure of each zone to be equal to the total cylinder pressure and by the volume balance,

$$V_{cyl} - \sum_{i=1}^{n\,zones} V_i = 0 \quad (5)$$

For n zones then there would be n temperatures, n volumes and the overall cylinder pressure values to solve at each timestep (a total of $2n + 1$ variables). A total of n energy balances, n ideal gas law balances and 1 volume balance also gave $2n + 1$ equations to solve. Such a system of k equations in k unkowns could be solved by a multi-variable Newton's Method [32] by iteratively setting

$$\mathbf{x}_{n+1} = \mathbf{x}_n - \mathbf{J}_n^{-1}\mathbf{f}_n \quad (6)$$

Until **x** converged, where **x** is the vector of variables, **f** is the vector of functions to be set to 0 (ie. the balance equations) and **J** is the Jacobian matrix of **f**.

Flame Propagation Modelling

The flame propagation of normal combustion was modeled by means of a Wiebe function representing the mass fraction burned (MFB), where the values of a, m, θ_{ign} and $\Delta\theta$ burn in Eqn. (5) were tuned to match experimental data.

$$\chi = 1 - e^{-a\left(\frac{\theta-\theta_{ign}}{\Delta\theta_{burn}}\right)^{m+1}} \quad (7)$$

The flame front was regarded as being infinitely thin and consumed mass in the unburned zones in a linear fashion as shown in Figure 5. Note that this does not necessarily mean that the flame itself proceeded linearly. As the flame front expands, it compresses the unburned gas ahead of it. This together with the swirl generated by the shrouded inlet valve would distort any original geometric distribution of the unburned zones. The zone consumption profile of the reference configuration would therefore not be the same as the geometric flame development profile. With the side mounted spark plug of the CFR, a simple linear consumption profile was used as the best first approximation.

For each MFB value, the segment corresponding to the MFB of the total cylinder volume was calculated and overlaid on the reference zone distribution profile. The appropriate incremental mass and enthalpy from each of the unburned zones lying within the burned segment was then transferred to the burned zone. An enthalpy balance involving the change of species from reactants to products accounted for the heat of combustion.

In the burned zone, the Water-Gas Shift and CO_2 dissociation equilibrium reactions were used to determine the final burned temperature by minimizing Gibbs Free Energy and balancing C, H and O atoms. This added 5 additional equations and 5 concentration variables of CO_2, CO, O_2, H_2O and H_2, to the system to be solved in Eqn. (6).

Heat Transfer

Heat Transfer was assumed to occur from the burned zone and the designated boundary layer unburned zone only. A Woschni correlation [13] was used to calculate the convective heat transfer coefficients. The proportional cylinder wall area was apportioned between the burned and unburned zones on a cylinder volume fraction basis. Although the coolant temperature for both RON and MON tests are specified at 100°C, a wall temperature of 150°C was used for these simulations, based on experimental measurements using surface thermocouples in the CFR [33]. Some variation in the Woschni coefficients was experimented with but, since these did not have a significantly large effect on the model results, it was decided to use the original textbook values for this initial study.

Autoignition Chemistry

In each unburned zone the chemical reactions specified by the FGAM were allowed to proceed with reaction rates calculated from the instantaneous temperature, pressure and species concentrations. For a given reaction

$$a_1X_1 + a_2X_2 \rightarrow a_3X_3 + a_4X_4 \quad (8)$$

The reaction rate (RR) was calculated by

$$RR = [X_1]^{n1}[X_2]^{n2}p^{np}Ae^{-B/T} \quad (9)$$

(where n_1, n_2, np, A and B are reaction rate coefficients) For each species X then, its rate of change of concentration with time was calculated by

$$\frac{d[X]}{dt} = \sum_{i=1}^{n\,reactions} b_i RR_i \qquad (10)$$

Where the b_i are the number of moles of X in the reaction equation of reaction i (the corresponding a value in Eqn (8)). Note that if X is a reaction product, $b_i > 0$; if X is a reactant, $b_i < 0$ and if X is not involved in the reaction then $b_i = 0$.

In each zone, a system of ordinary differential equations of species concentration with respect to time was thus defined. The differential equations were then solved within each chemical timestep before the physical balances, described in the sections above, were used to solve for the pressures, volumes etc in the next physical timestep. An energy balance was performed in each unburned zone at the end of each chemical timestep to realize any heat release from the intermediate reactions. To increase the resolution of the chemical timescale, multiple chemical timesteps were taken within each physical timestep based on an adaptive timestep method. Once an unburned zone had reached a critical temperature (in this case set to 1500 K) it was regarded as having autoignited and its contents were set to the same fractions as the burned zone to ensure the correct final equilibrium temperature.

MODEL CALIBRATION

Each engine model simulation was run from Inlet Valve Closure (IVC) to Exhaust Valve Opening (EVO). Determination of IVC cylinder temperature distribution and residual exhaust gas is extremely challenging to determine experimentally [34]. For this preliminary investigation, initial conditions were selected to best match experimental pressure traces and were checked against a basic engine breathing model and values from literature [35] to ensure these conditions were within reason.

A large collection of knocking and non-knocking CFR pressure traces from previous studies [8, 9, 10, 11] was used to calibrate the model and validate its results. These experiments were performed in a CFR engine fitted with a water-cooled piezo-electric pressure transducer with various PRF and TSF fuels under standard RON test conditions. The raw pressure trace and filtered rate of pressure change data was kindly supplied by the authors. The results of these experiments are presented alongside the model results where appropriate and referenced as [12]. Where average values from a series of engine cycles are used, error bars represent 1 standard deviation in distribution of the data.

The model parameters were adjusted to match the experimental runs of PRF100 knocking at SKI under RON100 conditions, and at RON80 test conditions to compare non-knocking traces. Features of the pressure traces to be matched were: pressure development during compression, pressure development during normal combustion, peak pressure and location of the knock point. A comparison of the non-knocking and knocking RON pressure traces are given in Figures 7 and 8 and a list of the operating parameters used is given in Table 1.

Table 1. Simulation Parameters used in the Multi-zone Model to fit experimental pressure traces

IVC	-146	CAD
EVO	140	CAD
Engine Speed	600	rpm
Bulk Temperature at IVC	400	K
Temperature Gradient at IVC	20	K
Pressure at IVC	0.97	bar
Residual Exhaust Gas Fraction at IVC	20%	
θ_{ign}	-18	CAD
$\Delta\theta_{burn}$	48	CAD
Wiebe a	9	
Wiebe m	5	
Number of Unburned Zones	20	
Number of Timesteps	600	

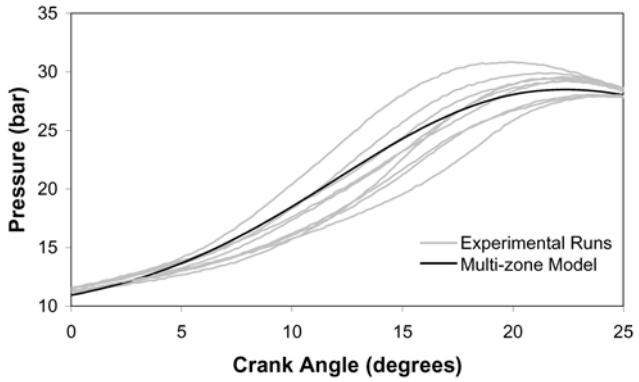

Figure 7. Comparison of the non-knocking pressure trace generated by the Multi-zone CFR Model with PRF100 at RON80 conditions with experimental pressure traces from [12] (burn duration 52 CAD)

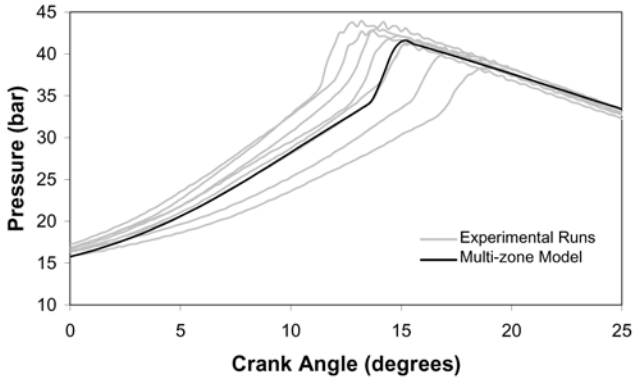

Figure 8. Comparison of the knocking pressure trace generated by the Multi-zone CFR Model with PRF100 at RON100 conditions with experimental pressure traces from [12] (burn duration 40 CAD)

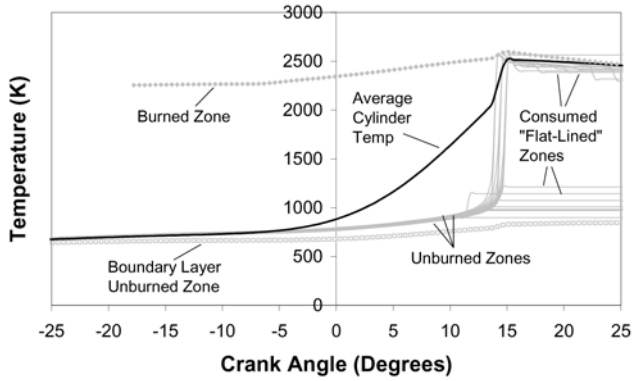

Figure 9. Temperature Development in each of the zones of the Multi-zone Model. Zones that "flat-line" have been completely consumed by the flame front

It may be noticed that the value used for θ_{ign} was not the actual spark advance value specified in the RON tests. This was because the values of *a* and *m* chosen resulted in a Wiebe function that showed negligible response in the first few CAD. It was found that with these coefficients, specifying a value of θ_{ign} of 5 CAD before actual spark timing produced a Wiebe function that closely approximated the MFB profile of experimental runs.

The Residual Exhaust Gas (REG) fraction of 20% may seem high and it is in fact higher than that predicted by the basic engine breathing model of 11%. This value was adjusted to reduce the pressure rise due to combustion in order to bring the model predictions in line with the experimental pressure traces. Adjustment to the REG value was more effective in this regard than adjustments to other values. It is notable in the appendix of Taylor [35] that describes the calculation of residual exhaust gas fraction, that the margin of error in this calculation at low engine speeds in the CFR can be very large with the maximum being just under 20%. It was decided therefore to use this REG value for this initial study.

Figure 8 shows that the knock pressure development produced by the model was very similar to that seen in the experimental CFR pressure traces. The different pressure traces show the cycle-to-cycle variation typical of SI engines. The knock-point was clearly visible at 14 CAD for the modeled trace and the mass fraction burned at this point was 70%, which was the same as that calculated from the experimental pressure trace using the Rassweiler and Withrow method described in [11].

An analysis of the temperature traces in each of the zones (Figure 9) clearly showed multiple autoignition events in succession after the knock point, simulating a cascading autoignition. Simulations run with smaller timesteps proved that it was not simply the timestep spacing that dictated the timing of the separate autoignition events. By looking at the average cylinder temperature it is apparent how this phenomenon results in the same pressure development as the knocking CFR engine.

A set of simulations were performed to identify the minimum number of zones required in the multi-zone model. Using too many zones is obviously computationally expensive. Simulations with 1 unburned zone produced the same type of results as in [15] with a near instantaneous pressure rise as the entire unburned endgas at the knock point autoignited. Simulations with 2, 5 and 10 zones produced distinct autoignition events but this resulted in a non-smooth pressure development. Simulations with 20 unburned zones produced a smooth cascading autoignition pressure development and so this was the number of zones used in the rest of the study.

RESULTS

PARAMETRIC STUDY

A parametric study was conducted in order to investigate how the model would react to a change in initial conditions and simulation parameters. A baseline run was performed with parameters for PRF100 fuel running at SKI under RON 100 conditions with other conditions as given in Table 1. In each set of simulations, all parameters were kept at the same baseline value except for one which was varied within a range. The independent influence of each of the model parameters could thus be assessed.

Some of the results of this study provided possible explanation for the effect of the operating parameters on the cascading autoignition phenomenon. Other results, which

may appear obvious, still had value in that they validated that the model responded to changes in the input parameters in the appropriate manner. The results of this study are described below with graphs of the pressure trace and time resolved rate of change of pressure. In each of the figures, the dark line represents the baseline case and the other results are represented by the lighter lines. The direction of change in the variable of interest is indicated by an arrow.

Compression Ratio

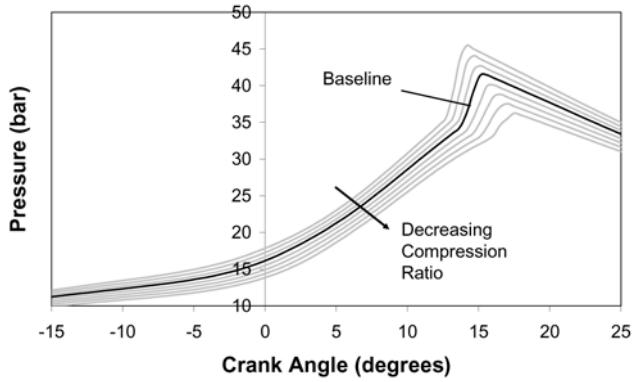

Figure 10. Parametric Study - Effect of Compression Ratio on Pressure Trace. CR = 7.0 to 8.4 in increments of 0.2

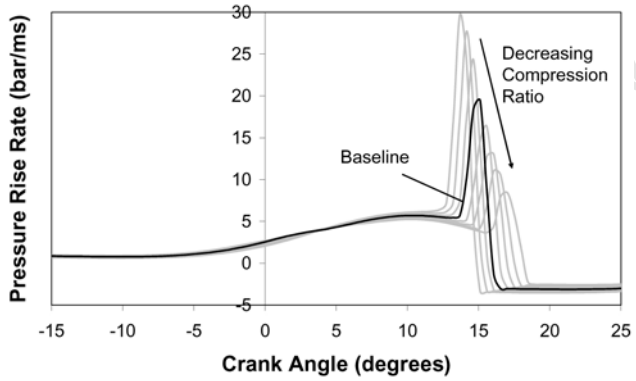

Figure 11. Parametric Study - Effect of Compression Ratio on Rate of Change of Pressure. CR = 7.0 to 8.4 in increments of 0.2

Figure 11 shows how the maximum pressure rise rate due to knock reduced rapidly with decreasing compression ratio in a fairly linear manner. The decrease from a compression ratio of 7.8 to 7.0 (or equivalent RON from 100 to 94) resulted in a decrease in this maximum from 19.5 bar/ms to 8.5 bar/ms. It is important to note that fuels generally still exhibit knock in the CFR engine at compression ratios corresponding to several Octane numbers lower than rated. However the knock intensity recorded would be reduced, due to the lower knock pressure rise rate seen here.

The comparison in Figure 12 with experimental runs of PRF100 running at increased compression ratios revealed a similar trend. At compression ratios below 7, the peak pressure rise rate remained relatively flat around 5 bar/ms, associated with normal combustion through flame propagation. Above this point, knock begins to occur and the peak pressure rise rate increases rapidly until SKI at the critical compression ratio (CCR) of 7.82. The response of the model to change in compression ratio was thus seen to be very similar to that of experiments.

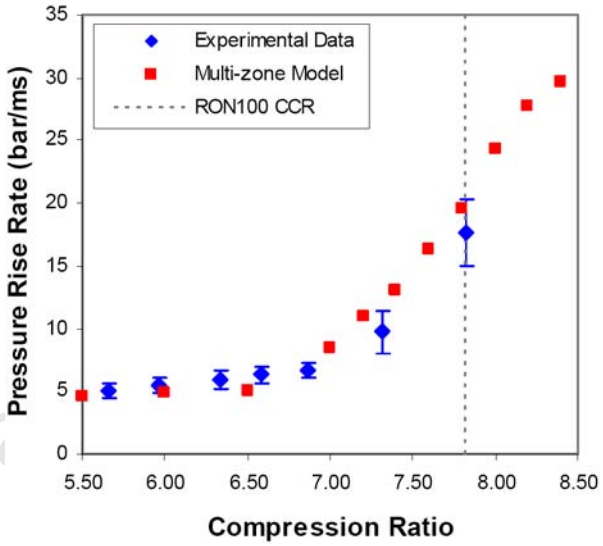

Figure 12. Peak Pressure Rise Rate for PRF100 running under various compression ratios compared with experimental data from [12]

Burn Duration

The Burn Duration was varied between 45 CAD and 54 CAD in increments of 1 CAD, with the results shown in Figures 13 and 14. As expected, the pressure traces were identical until the start of combustion at which point normal combustion proceeded either faster or slower depending on the burn duration. The knock point in the modeled traces moved incrementally later with longer burn duration, though the intensity of knock appeared consistent.

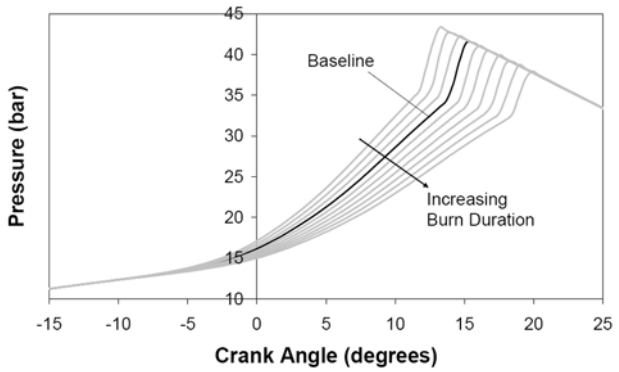

Figure 13. Parametric Study - Effect of Burn Duration on Pressure Trace. $\Delta\theta_{burn}$ = 45CAD to 54CAD in increments of 1CAD

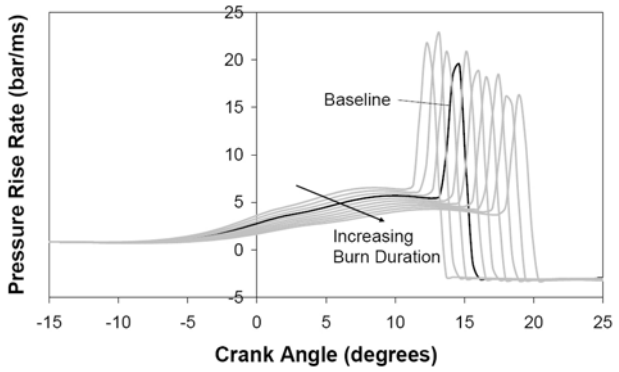

Figure 14. Parametric Study - Effect of Burn Duration on Rate of Change of Pressure. $\Delta\theta_{burn}$ = 45CAD to 54CAD in increments of 1CAD

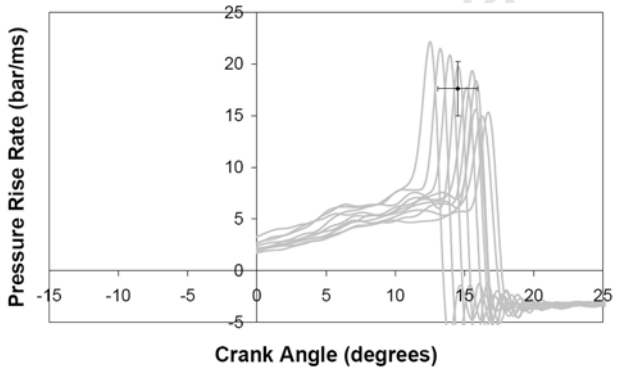

Figure 15. Selected filtered rate of change of pressure traces for PRF100 under RON100 conditions from [12]. Error bars represent 1 standard deviation in position and magnitude of peak pressure rise rate for cycle-to-cycle variation.

The differences in pressure developments in Figure 13 were very similar to the cycle-to-cycle variation seen in Figures 1 and 8. Furthermore comparison of pressure rise rates from the model in Figure 14 and actual experimental cycles in Figure 15 confirms this similarity. This suggests that cycle-to-cycle variation can be accounted for in the model by changes in burn duration.

This was an important result in this study as it reduced the need to accurately predict the burn duration for the different fuels and test conditions that were subsequently run. This further negated the need to deal with complex turbulent effects in the modeling of cycle-to-cycle variation.

Residual Exhaust Gas

Residual Exhaust Gas (REG) Fraction was varied between 5% and 35% in increments of 5%. The effect of REG fraction was much greater than initially anticipated. In reality, the dilution of unburned inlet charge with exhaust gas has the dual effect of reducing the amount of fuel which can combust to release heat and increasing the overall cylinder temperature at IVC. The results in Figures 16 and 17 show only the dilution effect with the inlet temperature held the same for each of the runs.

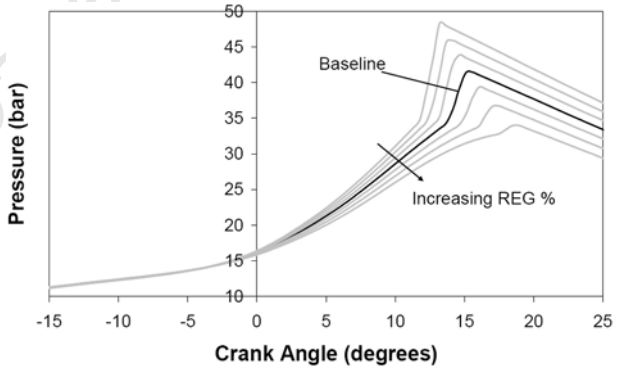

Figure 16. Parametric Study - Effect of Residual Exhaust Gas Fraction on Pressure Trace. REG = 5% to 35% in increments of 5%

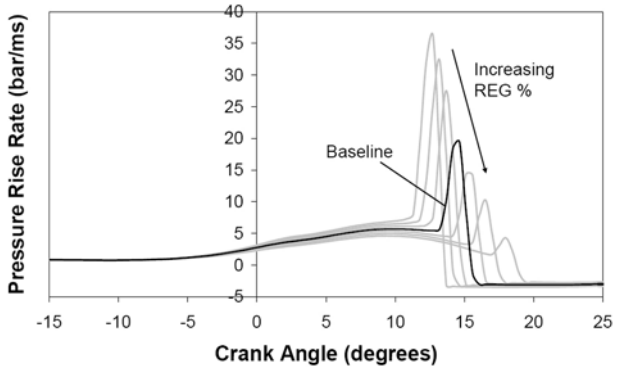

Figure 17. Parametric Study - Effect of Residual Exhaust Gas Fraction on Rate of Change of Pressure. REG = 5% to 35% in increments of 5%

With the reduced heat release from an increase in REG, the pressure traces showed a later onset of knock and of lower intensity. The high sensitivity of pressure rise rate to REG % highlights the importance of correctly modelling the inlet conditions. This also agreed with the logic of using a comparison to PRFs as the metric of knock resistance, rather than simply the compression ratio, as the reference fuels would be subject to the same REG effects as the test fuel, thus improving the reproducibility of test results.

A similar logic was applied in this study to justify the use of the seemingly large REG fraction of 20%, to bring the peak pressures predicted by the model in line with experimental results. As all fuels run would be subject to these same conditions, it is the comparison of their responses which is of interest.

Inlet Pressure

Inlet Pressure was varied between 0.95 bar and 1.0 bar in increments of 0.01 bar. The model response to changes in inlet pressure was the least sensitive of all the variables tested. Figure 18 shows that the different pressure traces generated were barely discernable and the pressure rise rates in Figure 19 were likewise of very similar magnitude. This implies that the Octane test results are not influenced too greatly by small variations in the inlet pressure, which may be caused by differences in ambient conditions or modifications of the intake system. This makes sense since autoignition delay is only weakly dependent on pressure compared to temperature.

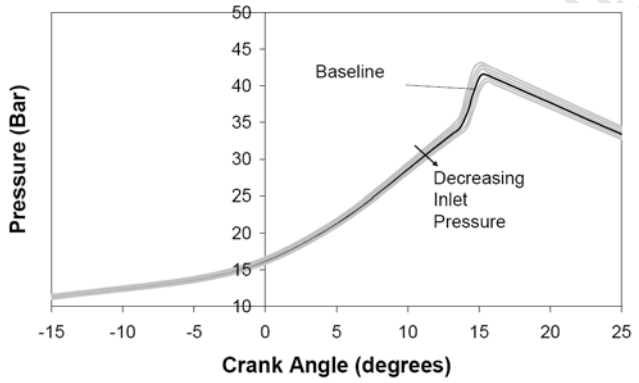

Figure 18. Parametric Study - Effect of Inlet Pressure on Pressure Trace. P_{IVC} = 0.95 bar to 1.0 bar in increments of 0.01 bar

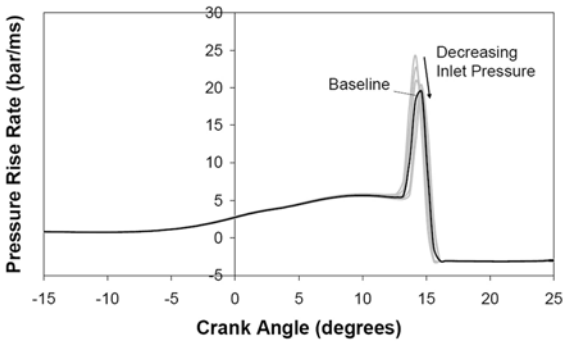

Figure 19. Parametric Study - Effect of Inlet Pressure on Rate of Change of Pressure. P_{IVC} = 0.95 bar to 1.0 bar in increments of 0.01 bar

Larger variations in atmospheric pressure such as that caused by change in altitude would have had a more appreciable effect, which is why slightly different test conditions are stipulated for larger differences in atmospheric pressure. However this would be more to bring the knockmeter readings in line with the expected values and should not influence the relative performance of different fuels greatly.

Inlet Bulk Temperature

The inlet bulk temperature at IVC was varied between 370 K and 450 K in increments of 10 K with the results shown in Figures 20 and 21 using 20 K increments for clarity. Given the uncertainty in measurement of the in-cylinder temperature, a broad range was investigated. The resultant pressure traces reached approximately the same peak pressure of 40 bar. Simulations with increased inlet temperature produced slightly lower pressures during normal combustion. This can be attributed to the fact that all simulations reached approximately the same peak temperature due to dissociation equilibrium reactions. Simulations with higher initial temperatures therefore experienced a lower total temperature rise due to combustion, resulting in a lower pressure at the same crank angle.

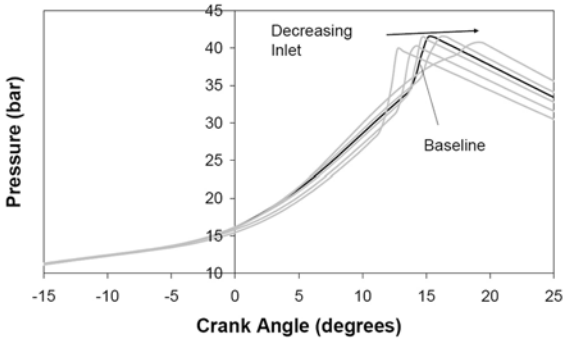

Figure 20. Parametric Study - Effect of Bulk Inlet Temperature on Pressure Trace. T_{IVC} = 370 K to 450 K in increments of 20 K

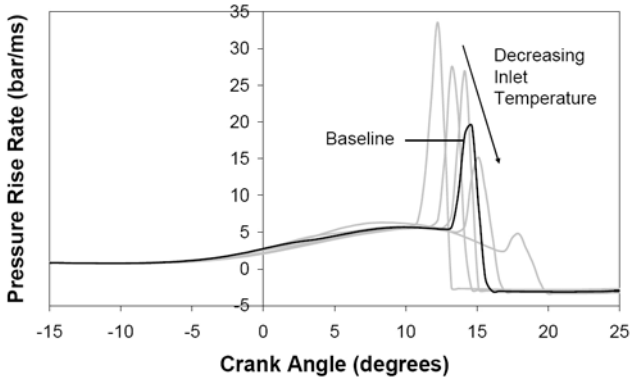

Figure 21. Parametric Study - Effect of Bulk Inlet Temperature on Rate of Change of Pressure. T_{IVC} = 370 K to 450 K in increments of 20 K

The onset of knock was predictably earlier for simulations with higher initial temperature, and therefore involved a larger fraction of the unburned gas. The pressure rise rate due to knock increased by between 5 and 10 bar/ms for an increase of 20 K in the initial temperature.

In-cylinder Temperature Gradient

The in-cylinder temperature gradient was varied between 0 K and 40 K in increments of 10 K. In order to achieve this, the bulk temperature was kept constant and the minimum and maximum temperatures adjusted, applying the same temperature profile, so that the difference between T_{max} and T_{min} in the unburned zones at IVC would be the temperature gradient required. The results of these simulations are shown in Figures 22 and 23.

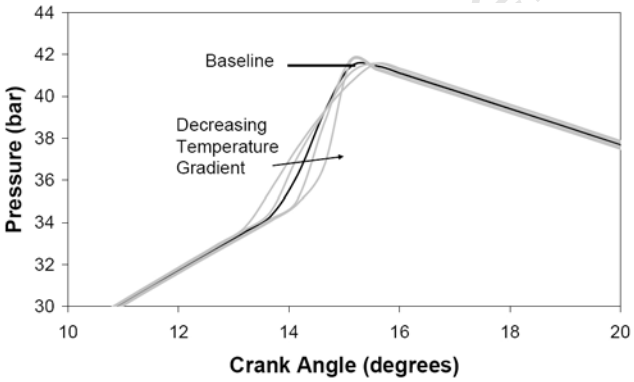

Figure 22. Parametric Study - Effect of In-cylinder Temperature Gradient on Pressure Trace. ΔT_{IVC} = 0 K to 40 K in increments of 10 K

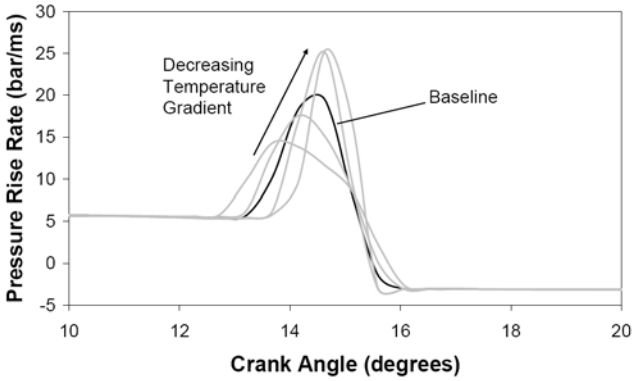

Figure 23. Parametric Study - Effect of In-cylinder Temperature Gradient on Rate of Change of Pressure. ΔT_{IVC} = 0 K to 40 K in increments of 10 K

Decreasing the temperature gradient had the effect of delaying the knock point (since the zone with the highest initial temperature would have autoignited first and would have started off at a lower initial temperature than other simulations). The other expected result is that the slope of the pressure trace after the knock point steepened with decreased temperature gradient, since zones at closer initial temperatures would autoignite in quicker succession. For an initial temperature gradient of 20 K, it is interesting to note that at TDC, the difference between maximum gas temperature and minimum temperature in the unburned zones was 30 K and at 5 CAD before knock-point it was 40 K. The temperature gradient resulting in cascading autoignition can therefore be much greater than at initial conditions.

Temperature Gradient Profile

Assuming an in-cylinder temperature gradient does exist, it is uncertain what the shape of the temperature profile would be. Several options of axisymmetric profiles were considered, as shown in the bottom right hand corner of Figure 24. Profiles **a**, **b** and **c** assumed a higher initial temperature at the walls, reducing inwards in either a convex, linear or concave profile. Profiles **d**, **e** and **f** assumed a higher temperature at the centre, reducing towards the walls.

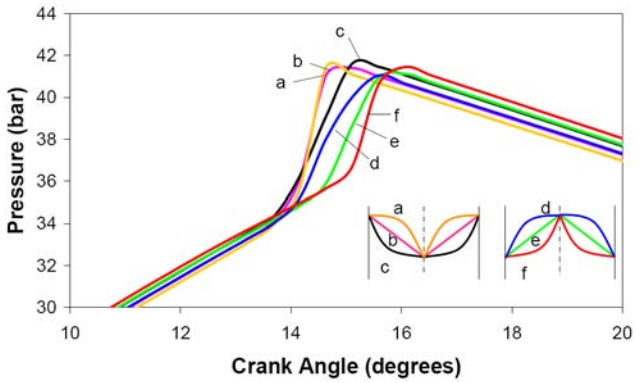

Figure 24. Parametric Study - Effect of Temperature Gradient Profile on Pressure Trace. Temperature profiles are as shown in the diagrams in the bottom right of the figure

The shapes of each of the pressure developments after the knock point were all slightly different. However Figure 25 shows that the peak pressure rise rate was approximately the same for all the profiles except **a** and **b**. This may be explained by the fact that the annular initial distribution of the zones meant that the outer most zones inherently contained more mass than the zones near the center. Profiles **a** and **b** therefore contained more mass at higher temperature, which would have resulted in a higher rate of pressure rise when they autoignited. The knock point of profiles **e** and **f** were delayed slightly because the hottest zones that would have autoignited first were completely consumed by the flame front before the knock point.

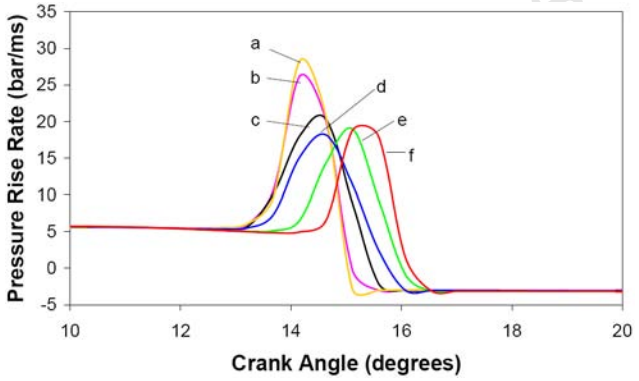

Figure 25. Parametric Study - Effect of Temperature Gradient Profile of Rate of Change of Pressure

Profile **c** was used for the rest of this study as it best matched the experimental pressure traces and this was consistent with the findings of [7]. However more detailed CFD modelling of the CFR in-cylinder flow and fuel evaporation would be required to verify this, as the very similar pressure traces of the different profiles may have produce quite different results when filtered to produce the knockmeter reading.

OCTANE PREDICTION FOR PRF AND TSF BLENDS

The FGAM was calibrated for PRF blends between PRF40 and PRF100 and the coefficients obtained are provided in Appendix A. The ASTM standards [1,2] list the compression ratios corresponding to SKI for the PRF blends and these are resultantly the critical compression ratios for their respective Octane Numbers. A Toluene Standardization Fuel designated TSF892 comprising 70% Toluene and 30% n-heptane was also fitted with the FGAM. This TSF has a RON of 89.2 and MON of 78.2. The fitted blends were then run in the multi-zone model under RON test conditions at their critical compression ratios. Simulation parameters were as per Table 1. Note that the burn duration remained the same for all simulations.

RON Simulations

The pressure traces generated from the PRF blends running under their critical compression ratios for RON are shown in Figure 26. Note that the model had been calibrated on the PRF 100 blend only and so the RON test simulations for other fuels were therefore purely predictive. These results showed good agreement with the experimental data of PRF blends run under these conditions [12]. The results for TSF892 simulated under RON90 conditions are also displayed. This showed a knock response similar to the PRF90 though slightly lower.

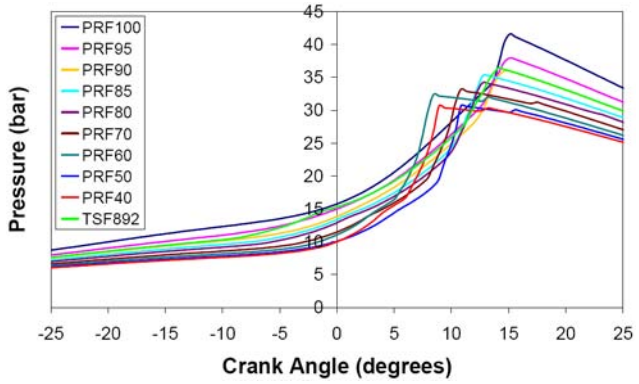

Figure 26. Pressure traces of PRF blends and TSF892 running at their respective RON test conditions

The mass fraction burned at knock point for the multi-zone model simulations were very consistent with the experimental results of the RON tests for PRF blends as seen in Figure 27. Generally a decrease in ON from RON100 resulted in a lower MFB at the knock point, and resultantly a higher mass fraction involved in the knock event. The increase in MFB for the RON50 test and subsequent decrease for RON40 was unexpected but confirmed by the experimental results. It is unclear why this deviation from the trend exists but it had been previously noted in [18]. The MFB for the TSF892

simulation is also shown. Although this value was lower than for the equivalent PRF, the difference was within the spread of the cycle-to-cycle variation of the experimental data. Swarts [36] has however noted, in comparisons between PRFs and TSFs, that the MFB at knock point need not necessarily be the same for different fuels with the same RON.

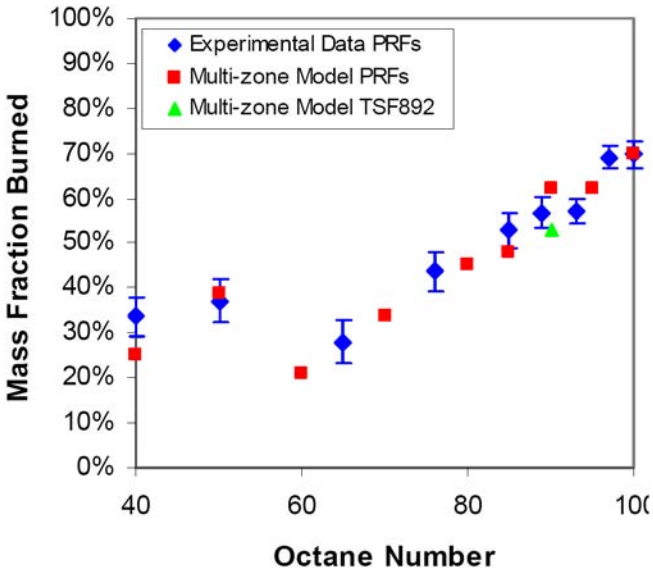

Figure 27. Mass Fraction Burned at Knock Point for RON Simulations compared with experimental results from [12]

The peak pressure rise rates for model simulations are shown in Figure 28. As with the experimental results, a decrease in Octane number resulted in an increase in peak pressure rise rate up till about RON60. The deviation to slightly reduced pressure rise rates for RON40 and RON50 were also simulated. Although the magnitudes of the pressure rise rates appear to agree quite well with experiment, too much should not be read into this as the experimental traces were first smoothed before analysis and this had the effect of reducing derivative values from the original noisy signal. The *trends* observed in change of peak pressure rise rate with Octane Number were consistent though. The pressure rise rate for TSF892 was however lower than for PRF90.

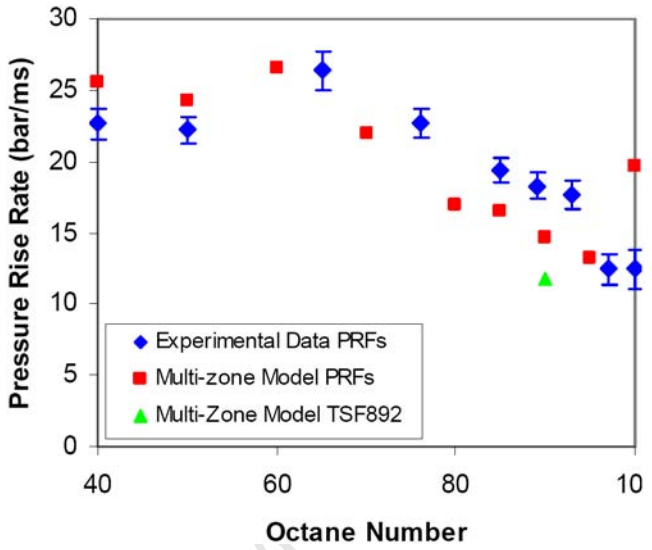

Figure 28. Peak Pressure Rise Rates for RON Simulations compared with experimental results from [12]

The one anomalous simulation point was ironically for the calibration point of RON100. It is uncertain why the peak pressure rise rate at this point was significantly higher than expected from the trend of the previous points. However two observations are worth mentioning. Firstly the experimental results show the RON100 peak pressure rise rate did not decrease from that of RON97, as would be expected from the trend, so at least some deviation should be expected from the simulation. Additionally the autoignition response of pure iso-octane is significantly different from that of blends with even small amounts of n-heptane. In Floweday's original calibration of the FGAM [28], it was noted that as good a fit for n-heptane was not obtainable for iso-octane. It is therefore possible that the autoignition heat release rate predicted by the FGAM for PRF100 was too high, resulting in an over-prediction of the knock pressure rise rate.

The PRF blends between RON80 and RON 100 were then run at compression ratios corresponding to 5 ON above and below their own. A comparison of the results is given in Figure 29. The pressure rise rates associated with the standard knock intensity were quite distinct from the higher and lower compression ratios run. The model could therefore differentiate between the RON of PRF blends above 80 within 5 ON.

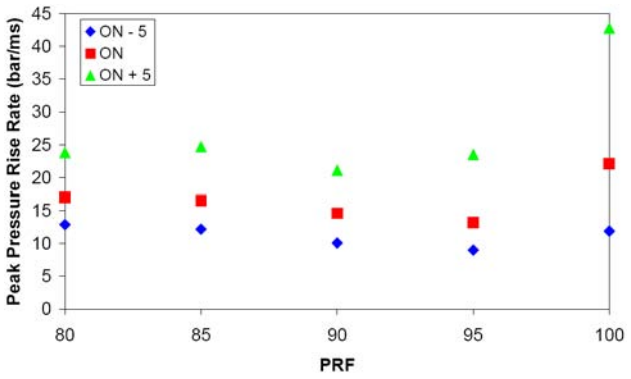

Figure 29. Peak Pressure Rise Rates for PRFs running at Critical Compression Ratio and at 5ON above and below

Simulations were also run of the PRF and TSF fuels under MON conditions. However these simulations did not yield as satisfactory results as the RON simulations. This may be due to the fact that the simulation parameters used were minor modifications of the RON parameters and a full investigation to fit the parameters to experimental data was not conducted, as had been done for RON. Such an investigation would be valuable as it would enable the multi-zone model to be applied to investigate the issue of octane sensitivity.

DISCUSSION

Mention has been made in this paper about filtering the pressure trace to emulate the operation of the knockmeter on the CFR engine. The effect of filtering is not only to eliminate high and/or low frequencies but also to make the peak value of the signal dependent on the development of the signal immediately prior to that point. Swarts et al [10] has already shown that simulation of the output of such a filtering system is possible on the actual pressure traces recorded in the engine. Applying such a filter to the results of the multi-zone model should also therefore be possible but would require simulations with a much higher timescale resolution (ie. smaller timesteps of approximately 0.02ms). In this way the results of the model could be directly interpreted in terms of Knock Intensity readings of the Octane Rating tests.

The use of the FGAM, instead of a detailed kinetic model, substantially reduced the computational time required by the Multi-zone model. A typical 20 zone Engine simulation required approximately 30 minutes on a standard desktop PC (Dual Core 2GHz Processor with 2GB of RAM). By contrast a *single, constant volume* Detailed Kinetic Simulation required between 30-60 minutes. Running multiple zones with a DKM in a changing temperature-pressure simulation would take a single run to the order of days. In order to fit the FGAM to a given fuel, generating the required DKM autoignition profile would take on average 2 days and optimising the reaction rate coefficients an additional 2 days. From thereon the FGAM could be used repeatedly with significantly lower computational effort. The calibrated FGAM would also not be limited to these simulations but could be further used for HCCI and other auto-ignition simulation applications by other researchers. The continuous improvement of computation technology will likely enable the use of DKMs in this multi-zone model in the near future. The FGAM does still have the advantage that its computational efficiency enables more simulations to be run in a given amount of time, which is of great importance in an investigative study such as this.

Although the FGAM was found to be able to fit the autoignition profiles of the PRF blends with good accuracy, some difficulty was encountered in fitting the ternary TSF blends of toluene, iso-octane and n-heptane, particularly with regards to the cool flame heat release rates. It has been documented that the autoignition behaviour of toluene/iso-octane blends is not fully understood, with some peculiarities in the blending behaviour [37]. This may explain why the FGAM, which was developed primarily with paraffin autoignition chemistry in mind, could not provide a good fit for the blend TSF998 (74% toluene, 10% iso-octane, 16% n-heptane). As a result only the blend of TSF892, which consists only of toluene and n-heptane, was included in this study. Based on the good results obtained in this implementation of the FGAM for the PRFs, it is proposed that further validation and investigation of this autoignition model be performed so that TSF and other blends can be more reliably modelled. In particular the FGAM needs to be validated for rich mixtures. Although all simulations in this study were performed under stoichiometric conditions, the Octane rating tests require that the air-fuel ratio be set to that producing maximum knock and for many fuels this would be just rich of stoichiometric [9].

This implementation of a multi-zone model showed proof of concept in its ability to emulate the pressure development in the CFR engine. Even with the acknowledged large simplifications and assumptions made, the results still showed very good agreement with experimental data. It may be possible to increase the accuracy of the model results by incorporating various other sub-models. A manifold and in-cylinder fuel evaporation study would provide a better set of initial conditions for both the temperature magnitude and in-cylinder distribution. A flame propagation model would remove the need for the empirically calibrated Wiebe description of flame propagation that was used. Veynante and Vervisch [38] provide a good description of available combustion models up till 2002 and new developments include the universal coherent flamelet model of Teraji et al [39] and a quasi-dimensional combustion model of Perini et al [40]. Additionally heat transfer effects both between zones and to the cylinder walls could be more accurately described. The combination of all these submodels including the FGAM

and pressure signal filter could take the form of a fully inclusive CFD model of the CFR engine.

CONCLUSIONS

• The characteristic knock pressure development in the CFR engine must be adequately modelled in order to determine standard knock intensity and thus classify the Octane rating of modelled fuels. Current modelling approaches which use detailed chemical kinetic models in a single unburned zone can accurately model the onset of autoignition, but are unable to reproduce the non-instantaneous pressure rise due to knock in the CFR.

• A multi-zone model incorporating the Functional Global Autoignition Model proposed in [28] and an initial temperature gradient within the cylinder is able to both predict the onset of autoignition and simulate a cascading autoignition. This results in the appropriate pressure development under knocking conditions in the CFR and strongly suggests that cascading autoignition is in fact the cause of this pressure development.

• The multi-zone model responds appropriately to changes in the operating parameters of inlet pressure, temperature and compression ratio.

• Variation of the burn duration was shown to emulate the effects of cycle-cycle variation both in the position of the knock point in varying cycles and with the uniformity of pressure rise rate in each cycle.

• Simulations of PRF blends running at the critical compression ratios for their respective RON ratings predicted results consistent with real engine experiments of these conditions with respect to knock peak pressure rise rate and mass fraction burned at knock point.

• Fitting the FGAM to a set of detailed chemical kinetic simulations allowed the use of a computationally efficient model to simulate autoignition in multiple zones subject to a changing pressure, temperature environment, whilst still accurately emulating cool flame timing and heat release dynamics. The natural extension of this is implementation in a CFD code with more accurate submodels.

REFERENCES

1. ASTM Standard D2699-09, “Standard Test Method for Research Octane Number of Spark-Ignition Engine Fuel”, ASTM International, West Conshohocken, PA, 2009.

2. ASTM Standard D2700-09, “Standard Test Method for Motor Octane Number of Spark-Ignition Engine Fuel”, ASTM International, West Conshohocken, PA, 2009.

3. Yates, A., Bell, A. and Swarts, A., “Insights relating to the autoignition characteristics of alcohol fuels”, *Fuel*, **89**:83-93, 2010.

4. Kalghatgi, G. T., “Fuel Anti-Knock Quality- Part II. Vehicle Studies - How Relevant is Motor Octane Number (MON) in Modern Engines?,” SAE Technical Paper 2001-01-3585, 2001, doi:10.4271/2001-01-3585.

5. Yates, A., Swarts, A. and Viljoen, C.L., “Correlating Auto-Ignition Delays And Knock-Limited Spark- Advance Data For Different Types Of Fuel,” SAE Technical Paper 2005-01-2083, 2005, doi:10.4271/2005-01-2083.

6. Floweday, G. “Two Contrasting Approaches to Auto-Ignition Modelling for HCCI engines”, PhD Thesis, Mechanical Engineering Department, University of Cape Town, 2010.

7. Hsiao, T.P., “Flame Propagation Model for the CFR Engine under Knocking and Non-Knocking Conditions”, Master's Thesis, Mechanical Engineering Department, University of Cape Town, 2006.

8. Yates, A., Swarts, B. and Viljoen, C.L., “An Investigation of Anomalies Identified within the ASTM Research and Motor Octane Scales,” SAE Technical Paper 2003-01-1772, 2003, doi:10.4271/2003-01-1772.

9. Swarts, A., Yates, A., Viljoen, C.L. and Coetzer, R., “Standard Knock Intensity Revisited: Atypical Burn Rate Characteristics identified in the CFR Octane Rating Engine,” SAE Technical Paper 2004-01-1850, 2004, doi: 10.4271/2004-01-1850.

10. Swarts, A., Yates, A., Viljoen, C.L. and Coetzer, R., “A Further Study of Inconsistencies between Autoignition and Knock Intensity in the CFR Octane Rating Engine,” SAE Technical Paper 2005-01-2081, 2005, doi: 10.4271/2005-01-2081.

11. Swarts, A. and Yates, A., “Insights into the Role of Autoignition during Octane Rating,” SAE Technical Paper 2007-01-0008, 2007, doi:10.4271/2007-01-0008.

12. Experimental Results from CFR engine study documented in [8-11] kindly supplied by the authors.

13. Heywood, J.B., “Internal Combustion Engine Fundamentals”, McGraw Hill, 1988.

14. Stone, R., “Introduction to Internal Combustion Engines”, Palgrave-Macmillan, 1999.

15. Mehl, M. Faravelli, T., Ranzi, E., Giavazzi, F., et al., “Kinetic Modeling Study of Octane Number and Sensitivity of Hydrocarbon Mixtures in CFR Engines,” SAE Technical Paper 2005-24-077, 2005, doi:10.4271/2005-24-077.

16. Hajireza, S., Mauss, F. and Sunden, B., “Two-Zone model of Gas Thermodynamic State in SI Engines with Relevance for Knock”, The Fourth International Symposium COMODIA 98, 1998.

17. Arrigoni, V., Cornetti, G., Spallanzani, G., Calvi, F., et al, “High Speed Knock in S.I. Engine,” SAE Technical Paper 741056, 1974, doi: 10.4271/741056.

18. Kee, R.J., et al., CHEMKIN Release 4.1, Reaction Design, San Diego, CA, 2006.

19. Konig, G. and Sheppard, C.G.W., "End-Gas Autoignition and Knock in a Spark Ignition Engine," SAE Technical Paper 902135, 1990, doi: 10.4271/902135.

20. Dent, J.C., Das, S. and Blundson, C.A., "Application of Computational Fluid Dynamics to the study of Conditions Relevant to Autoignition Damage in Engines," SAE Technical Paper 961963, 1996, doi: 10.4271/961963.

21. Brunt, M.F., Pond, C.R., and Biundo, J., "Gasoline Engine Knock Analysis using Cylinder Pressure Data," SAE Technical Paper 980896, 1998, doi: 10.4271/980896.

22. Mehl, M., et al., "Detailed Chemistry Promotes Understanding of Octane Numbers and Gasoline Sensitivity", *Energy and Fuels*, 20:2391-2398, 2006.

23. Curran, H.J. et al., "Autoignition Chemistry in a motored engine: An experimental and kinetic modeling study", presented at Western States section Meeting, Tempe, AZ (United States), 1996.

24. Griffiths, J.F., "Reduced Kinetic Models and their Application to Practical Combustion Systems", *Progress in Energy and Combustion Science*, **21**:25-107, 1995.

25. Floweday, G., "A New Functional Global Auto-ignition Model for Hydrocarbon Fuels - Part 1 of 2: An Investigation of Hydrocarbon Fuel Auto-ignition Behaviour and Existing Global Auto-ignition Models," *SAE Int. J. Fuels Lubr.* **3**(2): 710-724, 2010, doi:10.4271/2010-01-2161.

26. Yates, A. and Viljoen, C.L., "An Improved Empirical Model for Describing Auto-ignition," SAE Technical Paper 2008-01-1629, 2008, doi:10.4271/2008-01-1629.

27. Mittal, V., Heywood, J.B. and Green, W.H., "The Underlying Physics and Chemistry behind Fuel Sensitivity", *SAE Int. J. Fuels Lubr.* **3**(1):256-265, 2010, doi: 10.4271/2010-01-0617.

28. Floweday, G., "A New Functional Global Auto-ignition Model for Hydrocarbon Fuels - Part 2 of 2: Model Formulation, Development and Performance Assessment," *SAE Int. J. Fuels Lubr.* **3**(2):757-772, 2010, doi: 10.4271/2010-01-2169.

29. Mehl, M. et al "Detailed Kinetic Model of Gasoline Surrogate Mixtures", *Proceedings of the European Combustion Meeting 2009*, 2009.

30. Engelbrecht, A.P., "Computational Intelligence: An Introduction", John Wiley & Sons Ltd, ISBN 0-470-84870-7, 2002.

31. Mehl, M., Tardani, A., Faravelli, T., Ranzi, E., et al., "A Multizone Approach to the Detailed Kinetic Modeling of HCCI Combustion," SAE Technical Paper 2007-01-0086, 2007, doi:10.4271/2007-01-0086.

32. Press, W.H. et al., "Numerical Recipes in C: The Art of Scientific Computing", Cambridge University Press, 1992.

33. Marr, M.A. et al., "A Fast Response thermocouple for internal combustion engine surface temperature measurements", *Experimental Thermal and Fluid Science*, 34:183-189, 2010.

34. Swarts, A. and Yates, A., "In-Cylinder Fuel Evaporation and Heat Transfer Information Inferred from the Polytropic Character of the Compression Stroke in a Spark-Ignition Engine," SAE Technical Paper 2004-01-1856, 2004, doi: 10.4271/2004-01-1856.

35. Taylor, C.F., "The Internal Combustion Engine in Theory and Practice: Volume 1", 2nd Edition, MIT Press, Cambridge, Massachusetts, 1960.

36. Swarts, A., "Insights relating to octane rating and the underlying role of autoignition", PhD Thesis, Mechanical Engineering Department, University of Cape Town, 2006.

37. Vanhove, G., Petit, G., and Minetti, R., "Experimental study of the kinetic interactions in the low-temperature autoignition of hydrocarbon binary mixtures and a surrogate fuel", *Combustion and Flame*, **145**:521-532. 2006.

38. Veynante, D. and Vervisch, L., "Turbulent Combustion Modelling", *Progress in Energy and Combustion Science*, **28**:193-266, 2002.

39. Teraji, A., Tsuda, T., Noda, T., Kubo, M., et al., "Development of a Novel Flame Propagation Model (UCFM: Universal Coherent Flamelet Model) for SI Engines and Its Application to Knocking Prediction," SAE Technical Paper 2005-01-0199, 2005, doi:10.4271/2005-01-0199.

40. Perini, F., Paltinieri, F. and Mattarelli, E., "A quasi-dimensional combustion model for performance and emission of SI engines running on hydrogen-methane blends", *International Journal of Hydrogen Energy*, **35**:4687-4701, 2010

41. Mott, D.R., "New Quasi-Steady-State and Partial Equilibrium Methods for Integrating Chemically Reacting Systems", PhD Thesis, University of Michigan, 1999.

CONTACT INFORMATION

Marlan Perumal
Sasol Advanced Fuels Laboratory
Department of Mechanical Engineering
University of Cape Town
7708
Tel:+27 21 650 3242
marlan.perumal@sasol.com
www.safl.uct.ac.za

ACKNOWLEDGMENTS

This study was funded and supported by Sasol Technology Fuels Technology which is headed by Mr Paul Morgan. A vast database of experimental data was made available by Prof. Andy Yates and Dr Andre Swarts from their previous studies of the CFR engine.

ABBREVIATIONS

AI
Autoignition

ATC
After Top Dead Centre

BTC
Before Top Dead Centre

CAD
Crank Angle Degree

CCR
Critical Compression Ratio

CFD
Computational Fluid Dynamics

CFR
The standard engine used to measure Octane Number

DKM
Detailed Kinetic Mechanism

DISI
Direct Injection Spark Ignition

EVO
Exhaust Valve Open

FGAM
Functional Global Autoignition Model

HCCI
Homogenous Charge Compression Ignition

ID
Ignition Delay

IVC
Inlet Valve Closure

MON
Motor Octane Number

NTC
Negative Temperature Coefficient

ON
Octane Number

PRF
Primary Reference Fuel

RCM
Rapid Compression Machine

RON
Research Octane Number

SI
Spark Ignition

SKI
Standard Knock Intensity

TDC
Top Dead Centre

TSF
Toluene Standardization Fuel

APPENDIX A

REACTION MECHANISM SCHEMATIC OF THE FUNCTIONAL GLOBAL AUTOIGNITION MODEL (FGAM)

The Functional Global Autoignition Model makes use of the reaction scheme shown in Figure A1 with Reaction Rates as per Figures A2 and A3.

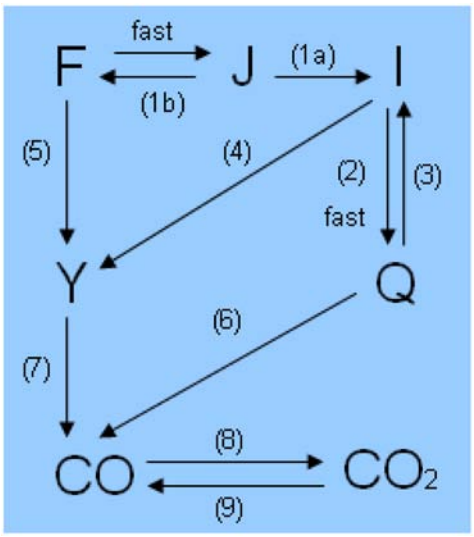

Figure A1. Reaction Mechanism for the FGAM [6]

$$RR_1 = 1/(1/K_{1a} + [F]^{a1}[O_2]^{b1} K_{1b})$$
$$RR_2 = [F]^{a2}[I]^{c2} K_2$$
$$RR_3 = [Q]^{d3} K_3$$
$$RR_4 = [I]^{c4} K_4$$
$$RR_5 = [F]^{a5}[O_2]^{b5} K_5$$
$$RR_6 = [Q]^{d6}[O_2]^{b6} K_6$$
$$RR_7 = [Y]^{e7}[O_2]^{b7} K_7$$
$$RR_8 = [\mathrm{CO}]^{f8}[O_2]^{b8} K_8$$
$$RR_9 = [\mathrm{CO_2}]^{g9} K_9$$

Figure A2. Reaction Rate Equations for the FGAM [6]

$$K_{1a} = A_{1a} e^{B_{1a}/T}$$
$$K_{1b} = A_{1b} P^{n1b} e^{B_{1b}/T}$$
$$K_2 = A_2 P^{n2} e^{B_2/T}$$
$$K_3 = A_3 e^{B_3/T}$$
$$K_4 = A_4 e^{B_4/T}$$
$$K_5 = A_5 P^{n5} e^{B_5/T}$$
$$K_6 = A_6 P^{n6} e^{B_6/T}$$
$$K_7 = A_7 P^{n7} e^{B_7/T}$$
$$K_8 = A_8 e^{B_8/T}$$
$$K_9 = A_9 e^{B_9/T}$$

Figure A3. Reaction Rate Constants for the FGAM Reaction Rates [6]

In the schematic, *F* represents the fuel. *J*, *I*, *Y* and *Q* are intermediate species with the same thermodynamic and chemical properties as *F*. Reactions 6 and 7 are the balanced reactions with Oxygen to form *CO* and H_2O. Reactions 8 and 9 represent the dissociation equilibrium $CO + 0.5O_2 \leftrightarrow CO_2$.

The system $F \leftrightarrow J \rightarrow I$ is treated with a Quasi Steady State Assumption (QSSA) [41] to reduce to the Reaction $F \rightarrow I$ with the Reaction Rate of the form given in *RR1*.

The *A*, *B*, *n* and concentration power coefficients are adjusted to fit the autoignition profiles generated by Detailed Chemical Kinetic Models. Further details are contained in [6].

APPENDIX B

FGAM CALIBRATION COEFFICIENTS FOR PRF BLENDS

	PRF100	PRF95	PRF90	PRF85	PRF80	PRF70	PRF60	PRF50	PRF40	TSF892
Average Error in Fit	11%	12%	9%	9%	10%	9%	10%	6%	11%	15%
% iso-octane	100	95	90	85	80	70	60	50	40	0
% n-heptane	0	5	10	15	20	30	40	50	60	30
% toluene	0	0	0	0	0	0	0	0	0	70
Coefficients										
ln(A1a)	26.671	25.755	25.807	25.335	25.208	25.240	25.707	25.834	25.706	26.906
B1a	-15254	-14490	-14346	-14133	-14043	-13889	-14311	-14393	-14278	-15124
a1	-0.137	-0.159	-0.146	-0.146	-0.145	-0.151	-0.151	-0.158	-0.152	-0.178

b1	0.712	0.770	0.770	0.853	0.810	0.931	0.731	0.724	0.747	0.702
ln(A1b)	20.244	20.057	20.546	19.950	20.298	19.881	19.611	19.126	19.821	22.202
n1b	-2.800	-2.748	-2.782	-2.723	-2.737	-2.716	-2.574	-2.622	-2.570	-2.934
B1b	-14493	-17243	-17579	-17894	-18165	-19041	-18223	-17808	-19317	-20500
a2	1.208	1.009	1.080	1.123	1.137	1.724	2.190	2.198	2.339	1.006
c2	0.596	0.633	0.627	0.608	0.613	0.617	0.645	0.693	0.640	0.670
ln(A2)	22.430	24.418	24.379	25.060	26.117	26.338	26.300	23.998	26.399	23.293
n2	-1.111	-1.149	-1.156	-1.147	-1.167	-1.391	-1.658	-1.658	-1.695	-1.515
B2	-7995	-8239	-8466	-8171	-8316	-9020	-7929	-8232	-7849	-7651
d3	2.810	2.859	2.842	2.925	2.841	2.827	2.633	2.383	2.877	2.255
ln(A3)	50.997	43.463	43.074	43.440	43.647	43.393	42.759	44.315	42.639	40.047
B3	-30694	-24088	-24404	-25540	-26177	-25412	-25626	-24671	-25093	-24641
c4	0.015	0.034	0.033	0.024	0.033	0.034	0.034	0.034	0.032	0.030
ln(A4)	36.791	47.840	46.972	46.095	46.662	46.080	45.221	42.387	44.341	46.797
B4	-23536	-33192	-33345	-30556	-30335	-30701	-28921	-31083	-29102	-33071
a5	0.987	0.634	0.891	0.894	0.920	0.940	0.933	0.751	0.941	0.909
b5	0.794	0.844	0.849	0.849	0.855	0.869	0.928	0.939	0.943	0.805
ln(A5)	21.235	21.462	21.457	21.468	21.461	20.749	19.137	19.302	19.360	22.084
n5	-0.556	-0.552	-0.503	-0.616	-0.570	-0.553	-0.545	-0.541	-0.540	-0.488
B5	-17263	-16390	-16583	-16688	-16863	-16641	-15773	-15764	-15787	-18129
d6	5.875	5.149	5.160	5.738	5.703	5.675	5.623	5.603	5.659	5.182
b6	0.149	0.151	0.152	0.149	0.154	0.157	0.159	0.163	0.160	0.169
ln(A6)	25.342	24.864	24.733	27.056	27.139	26.383	28.552	28.715	28.938	25.162
n6	-0.034	-0.037	-0.037	-0.030	-0.031	-0.031	-0.030	-0.032	-0.031	-0.036
B6	-15488	-15412	-15645	-16400	-15713	-15955	-16169	-16292	-15898	-16587
e7	2.578	0.704	0.701	1.739	2.016	1.686	1.674	1.693	1.735	0.731
b7	0.148	0.155	0.151	0.153	0.151	0.152	0.155	0.162	0.154	0.185
ln(A7)	13.161	11.872	11.792	11.992	12.032	12.575	13.152	13.253	13.221	11.509

n7	2.035	1.793	1.803	1.802	1.794	1.745	1.773	1.793	1.784	1.623
B7	-14863	-13384	-13175	-13505	-13494	-13489	-13565	-13728	-14148	-13149
f8	3.916	-0.102	-0.101	0.741	0.733	0.732	0.753	0.752	0.678	-0.118
b8	0.216	0.145	0.144	0.166	0.166	0.192	0.189	0.192	0.188	0.162
ln(A8)	23.022	16.168	16.390	16.483	16.528	19.597	23.610	24.553	23.573	17.397
B8	-1340	-15726	-15615	-14447	-14603	-13946	-13585	-12509	-13831	-14966
g9	0.903	1.085	1.034	1.329	1.016	1.011	0.942	0.912	0.885	0.873
ln(A9)	20.513	21.367	21.298	25.574	21.747	20.701	22.050	22.092	22.241	22.317
B9	-45761	-44349	-45557	-45079	-45817	-46819	-46704	-54226	-46704	-45525

The Engineering Meetings Board has approved this paper for publication. It has successfully completed SAE's peer review process under the supervision of the session organizer. This process requires a minimum of three (3) reviews by industry experts.

ISSN 0148-7191

SAE Customer Service:
Tel: 877-606-7323 (inside USA and Canada)
Tel: 724-776-4970 (outside USA)
Fax: 724-776-0790
Email: CustomerService@sae.org
SAE Web Address: http://www.sae.org
Printed in USA